

*Electric fields at biomimetic
interfaces –
Spectro-electrochemical studies on the
vibrational Stark effect of artificial
membranes*

vorgelegt von
M. Sc.
Jana Katharina Staffa
geb. in Wiesbaden

von der Fakultät II – Mathematik und Naturwissenschaften
der Technischen Universität Berlin
zur Erlangung des akademischen Grades
Doktor der Naturwissenschaften
- Dr. rer. Nat. -

Genehmigte Dissertation

Promotionsausschuss:

Vorsitzender: Prof. Dr. Martin Lerch
Gutachter: Prof. Dr. Peter Hildebrandt
Gutachter: Prof. Dr. Franz Bartl

Tag der wissenschaftlichen Aussprache: 19.02.2019

Berlin 2019

Abstract

Electric fields and electrostatic interactions can essentially influence biological processes. This is particularly true for membrane proteins since their activities may be controlled by changes of the transmembrane potential. To elucidate such processes requires appropriate biomimetic membranes, preferentially on electrodes to allow variations of the potential across a bilayer. Particular convenient model membranes are tethered bilayer lipid membranes (tBLM) on nanostructured Au electrodes, which were characterized with a combination of spectroscopy and electrochemistry. The Au film serves as IR signal amplifier and working electrode at the same time. Thereby, structural and functional characterizations of membrane-embedded proteins could be detected.

Quantification of electric fields within the artificial biomimetic membrane is experimentally extremely challenging but of high relevance understanding molecular processes at membranes. As a particularly promising experimental approach, the vibrational Stark effect (VSE) may be exploited. The VSE refers to the electric field dependent modulation of the frequency of a localised vibrational mode. Suitable Stark reporter groups for biological systems are the thiocyanate or cyanide group, which exhibit frequencies that can easily be distinguished from lipid and protein vibrations.

On the basis of electrochemical impedance spectroscopy (EIS) and surface-enhanced IR absorbance (SEIRA) spectroscopy the electrostatics of a frequently used simple membrane model, a self-assembled monolayer (SAM), on Au and Ag electrodes were analysed. Here we have investigated SAMs of 6-mercaptopohexanenitrile (C₅CN), 7-mercaptopheptanenitrile (C₆CN) and 4-mercaptopbenzonitrile (MBN). The potential-dependent changes of the VSE were determined on the basis of an electrostatic model to derive a relationship between the electrode potential and the electric field at the head groups of the SAMs. The analyses afforded electric field strengths in the order of 10⁸ V/m.

In this work, for the first time, Stark reporter groups were incorporated into the tBLM system on a nanostructured Au electrode. A thiocyanate labelled sterol derivate 7-beta-thiocyanocholest-5-en-3-betaylacetate (CLSCN) combined with phospholipids, 1-palmitoyl-2-oleoyl-sn-glycero-3-phosphocholine (POPC) and 1-palmitoyl-2-oleoyl-sn-glycero-phospho-(1'-rac-glycerol) (POPG), was used to characterise the electrostatics and local electric field inside the tBLM. To determine the relationship between the electrode potential and the transmembrane potential, i.e. the quantity controlling membrane processes, two Stark reporter groups were incorporated into the model membrane: the cyanide function of MBN as one fraction of the phase-separated SAM and the azide group introduced in the head group of a phospholipid (1,2-dipalmitoyl-sn-glycero-3-phosphoethanolamine-N-(6-azidohexanoyl) - PE-N₃). The combined spectroscopic and electro-chemical analysis provided insights into the electrostatics of the water reservoir between the SAM and the lipid bilayer. Upon adaptation of the electrostatic model to the tBLM system, an approximate relationship between the electrode potential and the transmembrane potential was obtained that provides a satisfactory description in the range of the effective potential of zero charge.

Altogether, the present work has demonstrated the great potential of EIS and SEIRA spectroscopy in combination with the vibrational Stark effect to study electrostatic interactions and quantify local electric fields within artificial membrane models.

Zusammenfassung

Elektrische Felder und elektrostatische Wechselwirkungen können verschiedene biologische Prozesse wesentlich beeinflussen. So kann durch Änderungen des Transmembranpotentials die Aktivität und Struktur von Membranproteinen gesteuert werden. Zur Untersuchung dieser Prozesse sind geeignete biomimetische Modellmembranen erforderlich, die zum Zweck der Potentialkontrolle auf Elektroden aufgebracht werden. Besonders geeignete Membranmodelle sind sog. „tethered bilayer lipid membranes“ (tBLM) auf nanostrukturierten Au-Elektroden, die elektrochemisch und spektroskopisch charakterisiert wurden. Dabei dient die Au-Unterlage zum einen als IR-Signalverstärker und zum anderen als Arbeitselektrode. Mit dieser Methode wurden strukturelle und funktionelle Charakterisierungen von Membranproteinen erhalten.

Die Quantifizierung elektrischer Felder oder elektrostatischer Wechselwirkungen innerhalb der künstlichen biomimetischen Membranen ist experimentell herausfordernd, aber von größter Bedeutung für das Verständnis molekularer Prozesse in Membranen. Der Schwingungs-Stark-Effekt (vibrational Stark-effect - VSE) ist dabei ein besonders vielversprechender experimenteller Ansatz, der die Modulation der Frequenz von Valenzschwingungen durch lokale elektrische Felder beschreibt. Geeignete Stark-Reportergruppen für biologische Systeme sind die Thiocyanat- oder Cyanidgruppe, deren Schwingungsfrequenzen sich leicht von Lipid- und Proteinschwingungen unterscheiden lassen.

Auf der Basis der elektrochemischen Impedanzspektroskopie (EIS) und oberflächenverstärkten IR Absorptionsspektroskopie (SEIRAS) wurden zunächst die elektrostatischen Eigenschaften der einfachsten Membranmodelle, d.h. selbstorganisierter Monolagen (SAM) auf nanostrukturierten Au- und Ag-Elektroden analysiert. Dazu wurden SAMs aus 6-Mercaptohexannitril (C₅CN), 7-Mercaptoheptannitril (C₆CN) und 4-Mercaptobenzonitril (MBN) untersucht. Die potentialabhängige Variation des VSE wurde auf der Grundlage eines elektrostatischen Modells beschrieben. Dabei wurden für SAM-beschichtete Elektroden lokale elektrische Felder im Kopfgruppenbereich des SAMs von 10⁸ V/m bestimmt.

In dieser Arbeit wurden zum ersten Mal Stark-Reportergruppen in das tBLM-System auf einer nanostrukturierten Au-Elektrode eingebaut. Dazu wurde ein Sterolderivat mit einer Thiocyanatgruppe (7-beta-Thiocyanocholest-5-en-3-betaylacetat - CLSCN) in Kombination mit Phospholipiden, 1-Palmitoyl-2-oleoyl-sn-glycero-3-phosphocholin (POPC) und 1-Palmitoyl-2-oleoyl-sn-glycero-phospho-(1'-rac-glycerol) (POPG) verwendet, um die Elektrostatik und das lokale elektrische Feld in der tBLM zu charakterisieren. Zur Bestimmung des Zusammenhangs zwischen Elektroden- und Transmembranpotential, d.h. der Größe, die Membranprozesse kontrolliert, wurden zwei VSE Reportergruppen in die Modellmembran eingebaut: die Cyanid-Funktion des MBN, das als eine Fraktion des Phasen-separierten SAMs diente, und die Azid-Funktion, die in die Kopfgruppe eines Phospholipids (1,2-Dipalmitoyl-sn-Glycero-3-Phosphoethanolamine-N-(6-Azidohexanoyl) - PE-N₃) inkorporiert wurde. Der kombinierte Einsatz der EIS und SEIRA Technik lieferte neue Einsichten in die elektrostatischen Eigenschaften des Wasserreservoirs zwischen SAM und Lipiddoppelschicht. Nach Anpassung des elektrostatischen Modells an die tBLM konnte eine Beziehung zwischen dem Elektroden- und Transmembranpotential entwickelt werden, das zufriedenstellende Ergebnisse im Bereich des effektiven Potentials der Nullladung lieferte.

Insgesamt demonstriert die vorliegende Arbeit das große Potenzial der EIS- und SEIRA-

Spektroskopie in Kombination mit dem Schwingungs-Stark-Effekts für die Quantifizierung elektrostatischer Wechselwirkungen und lokaler elektrische Felder in Membranmodellen.

Publications

Parts of this work are published in the following article:

Staffa J.K.; Lorenz L.; Stolarski M.; Murgida D.H.; Zebger I.; Utesch T.; Kozuch J.*; Hildebrandt P.* Determination of the Local Electric Field at Au/SAM Interfaces Using the Vibrational Stark Effect *J. Phys. Chem. C* **2017**, *121*, 40, 22274-22285.

Other Publications in peer-reviewed journals:

Forbrig, E.; Staffa, J.K.; Salewski, J.; Mroginski MA.; Hildebrandt P.*; Kozuch, J*. Monitoring the Orientational Changes of Alamethicin Incorporating into Bilayer Lipid Membranes. *Langmuir* **2018** *34* (6), 2373–2385

First author **corresponding author*

Oral presentations:

1. “*Electric Fields at biomimetic Interfaces*”, International Graduate Research Training Group 1524 (IRTG 1524) Concluding colloquium, December 13th - 15th, 2017, Potsdam (Germany).
2. “*Spectro-Electrochemical Determination of Electric Fields at biomimetic interfaces*”, International Graduate Research Training Group 1524 (IRTG 1524) Annual Meeting, October 6th - 8th, 2017, Raleigh, NC (USA).
3. “*Spectro-Electrochemical Determination of Electric Fields at Model Membrane Systems*”, 9th International Conference on Advanced Vibrational Spectroscopy (ICAVS9), June 11th - 16th, 2017, Victoria (Canada).
4. “*Spectro-Electrochemical Determination of Electric Fields at biomimetic interfaces*” International Graduate Research Training Group 1524 (IRTG 1524) Annual Meeting, October 7th - 10th, 2016, Neuruppin (Germany).
5. “*Spectroscopic studies on the vibrational Stark Effect of biomimetic interfaces*”, International Graduate Research Training Group 1524 (IRTG 1524) Winter Workshop, November 25th - 28th, 2015, Potsdam, (Germany).
6. “*Spectroscopic studies on the vibrational Stark Effect of biomimetic interfaces*”, International Graduate Research Training Group 1524 (IRTG 1524) Annual Meeting, October 7th - 10th, 2015, Wilmington/Wrightsville Beach, NC (USA).

Poster presentations:

1. International Graduate Research Training Group 1524 (IRTG 1524) Spring School, March 5th – 11th, 2017, Beverly, MA (USA).
2. International Graduate Research Training Group 1524 (IRTG 1524) Annual Meeting, October 7th - 10th, 2015, Wilmington/Wrightsville Beach, NC (USA).

Table of Contents

Abstract.....	III
Zusammenfassung.....	IV
Publications.....	VI
Table of Contents	VIII
Abbreviations.....	XI
Nomenclature.....	XIII
1. Introduction and Motivation	1
2. Theoretical Background	3
<i>1. Vibrational Spectroscopy</i>	<i>3</i>
1.1 Theory of Vibrational Spectroscopy	3
1.2 Infrared Spectroscopy	7
1.2.1 Fourier-transform Infrared (FTIR) Spectroscopy.....	8
1.2.2 Attenuated Total Reflection-IR (ATR-IR) Spectroscopy.....	10
1.2.3 Surface-enhanced Infrared Absorption (SEIRA) Spectroscopy.....	11
<i>2. Electrochemical Impedance Spectroscopy.....</i>	<i>13</i>
2.1 Theory of EIS	14
2.1.1 Equivalent Circuits	15
2.1.2 Graphical Data Representation ^{23,24}	16
2.1.3 Constant Phase Element	18
<i>3. Biomimetic Interfaces.....</i>	<i>18</i>
3.1 Self-assembled Monolayer - SAM	18
3.1.1 Structure of Self-assembled Monolayers	19
3.1.2 Biochemical and Biological Applications of Self-assembled Monolayers.....	21
3.2 Membrane Systems	21
3.2.1 Lipids – The Fundamental Building Block of a Biological Membrane	21
3.2.2 Phospholipids	22
3.2.3 Transmembrane Potential.....	23
3.2.4 Solid Supported Membranes	24
3.3 Electrostatics at the Electrode Interfaces	27
<i>4. Models to Quantify the Electric Field.....</i>	<i>32</i>
4.1 The Vibrational Stark-effect.....	33
4.2 The Onsager Model to Calculate Solvent Reaction Fields.....	36
<i>5. Theoretical Methods.....</i>	<i>38</i>
3. Material and Methods	39
<i>1. Chemicals and Biomolecules</i>	<i>39</i>
1.1 Synthesis of Di-alkyl-nitriles-disulphides	40

2. Instrumentation	42
2.1 IR Spectrometer.....	42
2.1.1 Cells for IR Measurements.....	42
2.2 Electrochemistry and EIS.....	43
3. Procedures	43
3.1 SEIRA Spectroscopy.....	43
3.1.1 Electroless Deposition.....	43
3.1.2 Electrochemically Cleaning	44
3.1.3 Vibrational Spectroscopy of the Biomimetic Interfaces	45
3.2 ATR-IR and BioATR-IR Spectroscopy	46
3.3 EIS	48
3.4 DFT	48
4. Results and Discussion.....	50
1. <i>Stark Reporter Groups</i>	50
1.1 Results of the Solvatochromic IR and DFT Experiments	50
1.2 Methods to Obtain the Stark Tuning Rate.....	51
1.3 Determination of the Stark Tuning Rates for -CN, -SCN and - N ₃	52
2. <i>Self-assembled Monolayers on Au and Ag Electrodes</i>	53
2.1 Alkyl Nitrile SAMs on Au Electrodes	54
2.2 Aromatic and Aliphatic SAMs on Ag Electrodes	57
2.3 Comparison of the SAM Structure on Au and Ag	58
2.4 The Effective Potential of Zero Charge for the Au and Ag Interfaces.....	59
2.5 The Stark Tuning Rate for Nitrile-terminated Thiols.....	61
2.6 Potential-dependence of SEIRA Intensities	61
2.7 Potential-dependence of the Stretching Frequencies.....	62
2.8 The Local Electric Field at the SAM Interface	63
2.9 Summary	64
3. <i>Labelled Bilayer Membrane with CLSCN</i>	65
3.1 Results of the IR Measurements.....	65
3.2 Shifts of the Thiocyanate Frequency in different IR Experiments.....	67
3.3 Potential-dependent Changes of the Thiocyanate Vibration	68
3.4 The Local Electric Field in the Bilayer of a tBLM	70
3.5 Summary	70
4. <i>Determination of the Transmembrane Potential</i>	71
4.1 Composition of the Mixed Monolayer WK3SH/MBN	71
4.2 IR and EIS Measurements of the Labelled tBLM System with MBN and PE-N ₃	72
4.3 Analysis of the Mixed SAM Formation.....	75
4.4 The Effective Potential of Zero Charge for the tBLM	76
4.5 The Potential-dependent Frequency and Intensity Changes of C≡N	76
4.6 The Potential-dependent Frequency and Intensity Changes of N ₃	78
4.7 Electrostatics at Different MBN Containing Biomimetic Interfaces	79
4.8 Summary	82
5. Conclusion and Outlook	83
6. Appendix	86

A 1 Analyses of the Nanostructured Ag-film.....	86
A 2 Solvatochromic ATR Measurement of ACN and H-bonding Effect of C4CN	88
A 3 Results of the MD Simulations of C5CN and C6CN	88
A 4 Self-assambled Monolayer Absorbed on the Nanostructured Ag-film	89
A 5 Further IR Spectra of the Labelled tBLM System with CLSCN.....	91
A 6 Potential-dependent EIS Spectra for Different Biomimetic Interfaces	92
A 7 IR Spectra of the tBLM System with MBN and PE-N ₃	93
A 8 Summary of all Electrostatics Data Obtained in this Work.....	95
A 9 Cartesian Coordinates of the DFT Calculations	97
7. References	120
8. Danksagung	128

Abbreviations

<i>6MH</i>	<i>6-Mercapto-1-hexanol</i>	<i>DMSO</i>	<i>dimethyl sulfoxide</i>
<i>AC</i>	<i>alternating current</i>	<i>EF</i>	<i>enhancement factor</i>
<i>ACN</i>	<i>acetonitrile</i>	<i>EIS</i>	<i>electrochemical impedance spectroscopy</i>
<i>AFM</i>	<i>atomic force microscopy</i>	<i>fBLM</i>	<i>floating bilayer lipid membranes</i>
<i>Ag</i>	<i>silver</i>	<i>FTIR</i>	<i>Fourier-transform infrared</i>
<i>Ar</i>	<i>argon</i>	<i>IHP</i>	<i>inner Helmholtz layer</i>
<i>ATR</i>	<i>attenuated total reflexion</i>	<i>IR</i>	<i>infrared</i>
<i>Au</i>	<i>gold</i>	<i>IRE</i>	<i>internal reflection element</i>
<i>B3LYP</i>	<i>Becke, three-parameter, Lee-Yang-Parr</i>	<i>IR-RAS</i>	<i>reflection-absorption infrared spectroscopy</i>
<i>C</i>	<i>carbon</i>	<i>LB</i>	<i>Langmuir-Blodgett</i>
<i>C5CN</i>	<i>6- mercaptohexanenitrile</i>	<i>LS</i>	<i>Langmuir-Schaefer</i>
<i>C6CN</i>	<i>7-mercaptopheptanenitrile</i>	<i>MBN</i>	<i>4-mercaptobenzonitrile</i>
<i>-CH₃</i>	<i>methyl group</i>	<i>-N₃</i>	<i>azide group</i>
<i>CHCN</i>	<i>cyclohexanecarbonitrile</i>	<i>NEXAFS</i>	<i>near-edge x-ray absorption fine structure</i>
<i>CLSCN</i>	<i>7-beta-thiocyanocholest-5-en-3-beta-yl acetate</i>	<i>-NH₂</i>	<i>amine group</i>
<i>CN</i>	<i>nitrile</i>	<i>OD</i>	<i>optical density</i>
<i>-CN</i>	<i>cyanide group</i>	<i>-OH</i>	<i>hydroxyl group</i>
<i>-CO</i>	<i>carbonyl group</i>	<i>OHP</i>	<i>outer Helmholtz layer</i>
<i>-COOH</i>	<i>carboxyl group</i>	<i>PE-N₃</i>	<i>1,2-dipalmitoyl-sn-glycero-3-phosphoethanolamine-N-(6-azidohexanoyl) (ammonium salt)</i>
<i>COOHC₅N₃</i>	<i>5-Azidopentanoic acid</i>	<i>PM-IRRAS</i>	<i>polarization modulation reflection-absorption infrared spectroscopy</i>
<i>CV</i>	<i>cyclic voltammetry</i>	<i>POPC</i>	<i>1-palmitoyl-2-oleoyl-glycero-3-phosphocholine</i>
<i>DFT</i>	<i>density functional theory</i>		

<i>POPG</i>	<i>1-palmitoyl-2-oleoyl-sn-glycero-3-phospho-(1'-rac-glycerol) (sodium salt)</i>	<i>SNR</i>	<i>signal-to-noise ratio</i>
<i>PVD</i>	<i>physical vapor deposition</i>	<i>SPR</i>	<i>surface plasmon resonance</i>
<i>SAM</i>	<i>self-assambled monolayer</i>	<i>STR</i>	<i>Stark tuning rate</i>
<i>sBLM</i>	<i>supported bilayer lipid membrane</i>	<i>sUV</i>	<i>small unilamellar vesicles</i>
<i>-SCN</i>	<i>thiocyanate group</i>	<i>tBLM</i>	<i>tethered bilayer lipid membranes</i>
<i>SE(R)RS</i>	<i>surface-enhanced (resonance) Raman spectroscopy</i>	<i>vac</i>	<i>vacuum</i>
<i>SEIRA</i>	<i>surface-enhanced infrared absorption</i>	<i>VdW</i>	<i>Van-der-Waals interactions</i>
<i>Si</i>	<i>silicon</i>	<i>VSE</i>	<i>vibrational Stark effect</i>
<i>sLM</i>	<i>supported lipid monolayers</i>	<i>VSS</i>	<i>vibrational Stark Spectroscopy</i>

Nomenclature

A	<i>amplitude, absorbance or area</i>	I	<i>intensity, current or ionic strength</i>
α	<i>tilt angle of SAM or polarizability</i>	k	<i>Boltzmann constant or</i>
β	<i>torsion angle</i>	κ	<i>Debye length</i>
c	<i>velocity of light or concentration</i>	I_i	<i>Cartesian displacement coordinates</i>
C	<i>capacitance</i>	l_c	<i>chain length</i>
d_{ik}	<i>transformation coefficient</i>	λ	<i>frequency or wavelength</i>
d	<i>optical path length, distance or distance to centre of gravity</i>	M	<i>molecular mass</i>
δ	<i>phase difference or phase angle</i>	m_i	<i>mass of i</i>
e	<i>elementary charge</i>	μ	<i>dipole moment</i>
E	<i>potential</i>	$\Delta\mu$	<i>difference dipole moment</i>
E_F	<i>electric field</i>	$ \Delta\mu $	<i>modulus of the difference dipole moment: Stark tuning rate</i>
E_{pzc}	<i>potential of zero charge</i>	μ	<i>reduced mass</i>
$E_{pzc,eff}$	<i>effective potential of zero charge</i>	μ_q	<i>electric dipole moment</i>
ϵ_0	<i>electrical permittivity constant in vacuo</i>	$[\mu_q]_{if}$	<i>transition dipole moment</i>
ϵ_i	<i>dielectric constant of i</i>	N	<i>number of atoms</i>
ϵ_s	<i>dielectric constant of the solution</i>	N_a	<i>Avogadro constant</i>
ϵ	<i>molar absorption coefficient</i>	N_T	<i>number of molecules per volume</i>
θ	<i>phase or tilt angle between the vectors of the difference dipole moment and the electric field</i>	n_i	<i>refractive index of i</i>
f	<i>force constant or local electric field factor</i>	P	<i>shape factor</i>
		φ	<i>tilt angle of head group</i>

$\Delta\phi$	<i>transmembrane potential</i>	V	<i>potential energy</i>
ϕ_s	<i>surface potential</i>	ρ	<i>density</i>
ϕ_d	<i>dipole potential</i>	σ	<i>charge density</i>
ϕ_i	<i>potential of layer i</i>	V_c	<i>volume of alkyl chains</i>
q_i	<i>mass-weighted Cartesian displacement coordinates</i>	$\tilde{\nu}$	<i>wavenumber</i>
Q_k	<i>normal coordinates</i>	ν_0	<i>wavenumber at the effective potential of zero charge</i>
R	<i>resistance</i>	Ψ_i, Ψ_f	<i>wave functions of the initial (i) and final (f) vibrational state</i>
$\vec{R}_{F,solv}$	<i>solvent reaction field</i>	Y	<i>admittance</i>
T	<i>kinetic energy or temperature</i>	ω	<i>circular frequency</i>
t	<i>time</i>	Z	<i>impedance</i>
U	<i>current</i>	z	<i>number of electrons</i>

1. Introduction and Motivation

Electric fields play an important role in a wide range of biological processes. Particularly strong electric fields arise at the interface and inside lipid membranes. They control the structure and activity of membrane bound proteins, e.g. by regulating potential-dependent ion channels. Therefore, it is of highest interest to quantify these electric fields and gain insight into their impact on mechanisms of biochemical reactions.

However, the in-situ quantification of electric fields for biological processes has been a longstanding challenge in biophysics. A promising approach is based on the vibrational Stark effect (VSE). Hereby the vibrational transition of a certain molecule is sensitive to changes of the local electric field. Hence, the local electric field can be determined by the vibrational frequency shift of a so-called Stark reporter group. A suitable reporter group for studying biological systems is the nitrile group because it gives rise to a band in a relatively transparent region in the infrared spectrum. However, the nitrile frequency is also strongly influenced by hydrogen bonds and interactions with halogens. Thus, incorporation of these reporter groups in biological systems for determining local electric fields requires sorting out the contribution of hydrogen or halogen bonding.

The potential curve across a bilayer lipid membrane is defined by three potentials: (1) the surface potential (ϕ_S) at the lipid/solution interface, (2) the dipole potential (ϕ_D) inside the lipid head group region and (3) the transmembrane potential ($\Delta\phi$) between the two bulk phases separated by the membrane. (**Figure 1 A**) Especially in the boundaries between the hydrophobic core, the polar or charged head groups, and the solution phase high electric fields about 10^8 - 10^9 V/m occur.

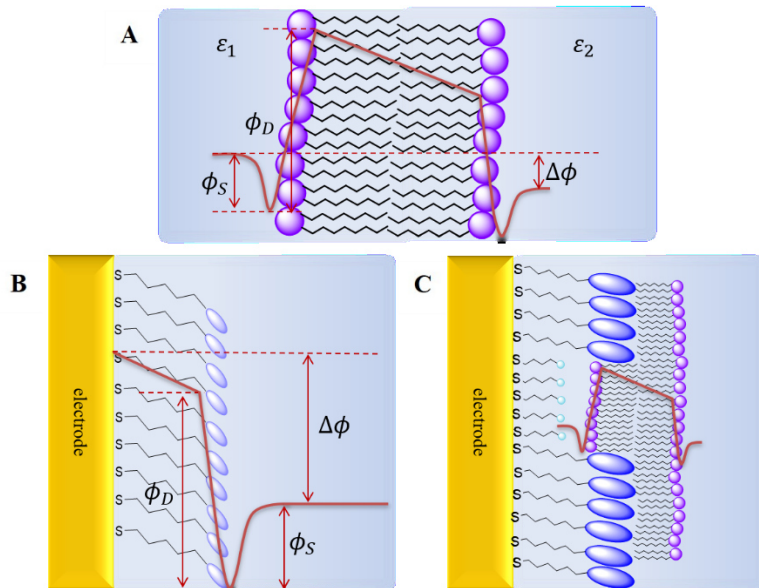


Figure 1: Two bulk phases (ϵ_1 , ϵ_2) separated by a bilayer lipid membrane is shown. The potential curve across the membrane (red line) is defined by the surface potential (ϕ_S), dipole potential (ϕ_D) and transmembrane potential ($\Delta\phi$). **(A)** Two biomimetic membranes, assembled on an electrode with their corresponding potential curve (red lined), is schematically presented **(B), (C)**.

These local electric fields are much higher than the global electric field calculated for a membrane with a transmembrane potential of 0.1 V and a 4 nm thickness of a lipid bilayer leading to 2.5×10^7 V/m. The latter value just represents a formal quantity which refers to a distance that is much larger than the dimension of a reactive site in a large molecule. It is thus not this global electric field that has an impact on biological processes but the local electric field at the reactive site.

To quantify local electric fields in and at the lipid membrane, Stark reporter groups can be incorporated into the system. This requires the use of model membranes that mimic natural biological membranes, at least as the electrostatic properties are concerned. The simplest model membrane is a self-assembled monolayer (SAM) deposited on a metal electrode, mimicking one half of a lipid bilayer. Using such a device, external potentials can be applied at the electrode and the frequency shift of the Stark reporter group can be analysed. The potential distribution over a SAM-coated electrode is governed by similar parameters (surface and dipole potentials as well as the electrode potential as the analogue for the transmembrane potential) as in the case of the bilayer lipid membrane (**Figure 1 B**). In the first part of this work aliphatic and aromatic nitrile terminated SAMs were assembled on gold and silver electrodes to analyse the interfacial electric field.

Solid-supported membranes form a more complex biomimetic interface. In this project a bilayer lipid membrane was mimicked using a tethered bilayer lipid membrane (tBLM) on Au as depicted in **Figure 1 C**. The tBLM system consists of a short and a long SAM with a polar and lipid head group, respectively. By spreading vesicles on the mixed SAM, a bilayer lipid membrane is formed. At the short SAM regions, the lipid bilayer is separated from the SAM by an aqueous phase because between the hydrophilic head groups and the lipid head groups a water reservoir is formed. Incorporating Stark reporter groups in lipids and the SAM, the local electric fields at the label position in the model membrane can be determined. This data may then allow deriving a relationship between the electrode potential and the transmembrane potential. Such a relationship is of utmost importance since it represents a link between molecular studies on model membranes and electrophysiological investigations at intact cells.

In this work, various components of the tBLM were labelled with different Stark reporter groups to map the electric field distribution across the model membrane. This approach represents the first attempt to correlate the electrode potential with the transmembrane potential of a model membrane.

2. Theoretical Background

1. Vibrational Spectroscopy

Vibrational spectroscopy has been developed throughout the last 200 years. In 1800, infrared (IR) radiation was discovered within the spectrum of light from the sun by Sir W. Herschel; this discovery established the foundation of vibrational spectroscopy.¹ Shortly afterwards, Albert A. Michelson invented the interferometer and received the Nobel Prize in 1907.² Leading scientists such as M. Plank and A. Einstein contributed to developments within vibrational spectroscopy with the black body radiation problem and the theory of the photoelectric effect by studying the interactions of light with matter, respectively.³ In 1928 Chandrasekhara. V. Raman reported the Raman effect and lay the foundation for a second vibrational spectroscopy, Raman spectroscopy.¹ In the late 1940s, the disperse IR spectrometer was made commercially available; this was followed approximately 20 years later by the Fourier-transform infrared (FTIR) spectrometer. Initially, only inorganic molecules were studied due to a lack of resolution but with time much more advanced spectrometers were developed, which allowed the study of more complex samples.⁴

Nowadays vibrational spectroscopy is one of the most powerful analytical techniques with which to study structure-functional relationships of biomolecules.^{1,5–7} With the development of resonance Raman spectroscopy and IR difference spectroscopy, it is feasible to probe structural properties and even single bonds in macromolecules with a high resolution. It is actually possible to study dynamic processes with time-resolved measurements, which can be resolved down to periods of femtoseconds or to study the kinetics of reactions.^{8,9} Vibrational spectra of molecules can be obtained for samples that are crystallized, solubilized or immobilized. The immobilization of molecules on metal surfaces forms the basis of surface-enhanced spectro-electrochemical measurements, like potential dependent SE(R)RS (surface-enhanced (resonance) Raman spectroscopy) or SEIRA (surface-enhanced IR absorbance) spectroscopy^{10,11}. The metal surface also functions as a working electrode in electrochemical measurements. This duality allows both spectroscopic and electrochemical measurements to be performed simultaneously, as it was the case in this work. This provides a more detailed insight into the role of electric fields in the biological processes that occur in and across membranes.

1.1 Theory of Vibrational Spectroscopy

Vibrational spectroscopy is based on electromagnetic radiation causing a transition between vibrational states when it interacts with matter.¹² IR and Raman spectroscopy are two complementary methods associated with different underlying physical processes. For IR, a resonant absorption occurs whereas for Raman inelastic scattering is responsible for the vibrational state transition.¹ Thus, IR spectroscopy is based on a one-photon process, while during the inelastic scattering two photons are involved. Both processes can also be related to rotational transitions, which appear as the fine structure of vibrational transitions. However, this fine structure can only be resolved in the gas phase, so it has no relevance for vibrational

spectroscopic studies of biological molecules. Molecule vibrations can be considered IR-active if a change of the dipole moment occurs as a result of the electromagnetic radiation interacting with the molecules, and Raman-active if a change of the polarizability occurs.

Molecular vibrations Molecular vibrations can be described by the harmonic oscillator model, which makes the assumptions that two point masses (m_A, m_B) are connected by a mass-less spring; the spring performs a vibration with the vibrational frequency along the x-axis; and their displacement along the axis from the equilibrium position (R_0) to position (R) is equal to Δx . The potential energy (V) and kinetic energy (T) of the vibrational movement can be expressed in the following two equations, respectively:

$$V = \frac{1}{2}f(R - R_0)^2 = \frac{1}{2}f\Delta x^2 \quad (2.1)$$

and

$$T = \frac{1}{2}\mu\left(\frac{d\Delta x}{dt}\right)^2 \quad (2.2)$$

where f describes the force constant due to the restoring force $F = -f\Delta x$ (Hooke's law) of the spring and μ is the reduced mass of the two point masses m_A and m_B according to:

$$\mu = \frac{m_A * m_B}{m_A + m_B} \quad (2.3)$$

As the vibration is undamped the energy conservation demands that the sum of the derivatives of potential and kinetic energy equals zero

$$0 = dVdt + dTdt \quad (2.4)$$

resulting in the Newton equation of motion

$$0 = \frac{f}{\mu}\Delta x + \frac{d^2\Delta x}{dt^2} \quad (2.5)$$

which can be solved by the cosine function

$$\Delta x = A \cos(\omega t + \theta). \quad (2.6)$$

Here A and θ describe the vibrations amplitude and phase, respectively. The circular frequency ω depends on the quotient of the force constant and the reduced mass:

2. Theoretical Background

$$\omega = \sqrt{\frac{f}{\mu}} \quad (2.7)$$

commonly it is expressed in wavenumbers $\tilde{\nu}$ (cm^{-1}), which is achieved by a division of the circular frequency by $2\pi c$

$$\tilde{\nu} = \frac{1}{2\pi c} \sqrt{\frac{f}{\mu}} \quad (2.8)$$

where c is the velocity of light. This equation confirms the positive correlation between the vibrational frequency and the bond strength and conversely the negative correlation with mass.

Normal modes A system with more than two atoms requires a more complex approach. Molecule vibrations are defined in terms of the so-called normal modes. A normal mode describes the vibration of all atoms in a molecule with the same frequency, but with different amplitudes. For a molecule with N atoms, there are $3N - 6$ normal modes. This number is based on the total number of degrees of freedom of $3N$, which is then reduced by 3 translational and 3 rotational degrees of freedom. In the case of a linear molecule, this number changes to $3N - 5$, since only 2 rotational degrees of the molecule exist. The displacement of the Cartesian coordinates of all atoms of the molecule must be considered determining the frequencies of the normal modes. The kinetic energy is:

$$T = \frac{1}{2} \sum_{\alpha=1}^N m_{\alpha} \left[\left(\frac{d\Delta x_{\alpha}}{dt} \right)^2 + \left(\frac{d\Delta y_{\alpha}}{dt} \right)^2 + \left(\frac{d\Delta z_{\alpha}}{dt} \right)^2 \right]. \quad (2.9)$$

Introducing mass-weighted Cartesian displacement coordinates q_i with $l_i = \Delta x_i, \Delta y_i, \Delta z_i$ defined as

$$q_i = \sqrt{m_i} l_i, \quad (2.10)$$

the kinetic energy can be simplified to

$$T = \frac{1}{2} \sum_{i=1}^{3N} \left(\frac{dq_i}{dt} \right)^2. \quad (2.11)$$

The potential energy represents a more complex term, all possible interactions between all atoms (covalent and electrostatic) are considered in the expression as a Taylor series

$$V = V_0 + \sum_{i=0}^{3N} \left(\frac{\partial V}{\partial q_i} \right)_0 q_i + \frac{1}{2} \sum_{i,j=1}^{3N} \left(\frac{\partial^2 V}{\partial q_i \partial q_j} \right)_0 q_i q_j. \quad (2.12)$$

For the interpretation of the vibrational potential energy, only changes of V based on the displacement of the individual atoms are of interest. Therefore, the first term, which describes the potential energy at the equilibrium, and the second term, as infinitesimal changes of q_i at the equilibrium do not influence the potential energy, are equal to zero. Within the harmonic approximation, higher order terms do not essentially affect the potential energy and can be neglected. Following the potential energy can be simplified to:

$$V \approx \frac{1}{2} \sum_{i,j=1}^{3N} \left(\frac{\partial^2 V}{\partial q_i \partial q_j} \right)_0 q_i q_j = \frac{1}{2} \sum_{i,j=1}^{3N} f_{ij} q_i q_j. \quad (2.13)$$

In analogy to **equation (2.5)** the newton equation, in dependence of the kinetic and potential energy, can be expressed as

$$0 = \frac{d^2 q_j}{dt^2} + \sum_{i=1}^{3N} f_{ij} q_i \quad (2.14)$$

with the general solution of $3N$ linear second order differential equations of

$$q_i = A_i \cos(\sqrt{\lambda} t + \theta). \quad (2.15)$$

Here λ is the frequency and θ the phase of the vibration. The system of differential equations can be solved with $3N$ solutions for λ representing $3N$ frequencies $\lambda^{\frac{1}{2}}$. There are $3N - 6(5)$ non-zero solutions; these indicate the 3 (2 in the case of a linear molecule) rotational and 3 translational degrees of freedom and therefore yielding the frequencies of the $3N - 6(5)$ normal modes. Consequently, knowing all frequencies the amplitude A_i can be calculated. The disadvantage treating normal modes in the Cartesian coordinate system is the distribution of all information for a normal mode in $3N$ equations. Therefore, for a more compact presentation the mass-weighted Cartesian displacement coordinates are converted into normal coordinates (Q_k) via an orthogonal transformation. As an approximation, these normal coordinates are reduced to the segment of the molecule with the most pronounced motion, due to the substantial difference between the amplitudes.

$$Q_k = \sum_{i=1}^{3N} d_{ik} q_i. \quad (2.16)$$

The transformation coefficient d_{ik} has been chosen in such a way that, in terms of the new coordinates, the kinetic and potential energies takes the same form according to **equation (2.11)** and **(2.13)** and that potential energy does not depend on the cross products of Q_k . The

2. Theoretical Background

kinetic energy retains its original form, which leads to the following solution of the Newton equation¹:

$$Q_k = K_k \cos(\sqrt{\lambda_k} t + \theta). \quad (2.17)$$

1.2 Infrared Spectroscopy

Infrared Absorption The IR radiation within the electromagnetic spectrum is located in the region from 10 to 12500 cm⁻¹.¹ The absorbance A (in OD = optical density) of a sample is given by the fundamental Bouguer-Lambert-Beer-Law:¹³⁻¹⁵

$$A = -\lg \left(I/I_0 \right) = \varepsilon * c * d. \quad (2.18)$$

Here, I and I_0 are the intensities of the parallel IR radiation after traversing through a sample with or without the analyte, respectively. Consequently, the absorbance of any component is proportional to its concentration c and the optical path length d . The molar absorption coefficient ε includes the transition probability between the initial and final vibrational state. It is derived quantum mechanically and expressed by the wave functions of the initial (Ψ_i) and final (Ψ_f) vibrational state and the electrical dipole moment operator $\hat{\mu}_q$:

$$[\mu_q]_{if} = \langle \Psi_f^* | \hat{\mu}_q | \Psi_i \rangle. \quad (2.19)$$

The electric dipole moment is given by the charge e of each atom and its distance d to the centre of gravity

$$\hat{\mu}_q = \sum_{\alpha} e_{\alpha} * d_{\alpha}. \quad (2.20)$$

A vibrational mode is IR-active if the correlated transition dipole moment is non-zero. This can be shown when expanding the operator of the electric dipole moment in a Taylor series, with respect to the normal coordinates Q_k , within the harmonic approximation

$$\hat{\mu}_q = \mu_q^0 + \sum_{k=1}^{3N-6} \hat{\mu}_q^k * Q_k \quad (2.21)$$

with

$$\hat{\mu}_q^k = \left(\frac{\partial \mu_q}{\partial Q_k} \right)_0. \quad (2.22)$$

Therefore, the transition probability can be expressed as:

$$[\mu_q]_{if} = \langle \Psi_f^* | \hat{\mu}_q | \Psi_i \rangle = \mu_q^0 \langle \Psi_f^* | \Psi_i \rangle + \sum_{k=1}^{3N-6} \hat{\mu}_q^k \langle \Psi_f^* | Q_k | \Psi_i \rangle. \quad (2.23)$$

The first term is equal to zero due to the orthogonality of the wavefunctions Ψ_i and Ψ_f . The second term is only non-zero when the following conditions are satisfied: the electric dipole moment changes with the normal coordinate during a vibration, and the quantum numbers of the wave functions differs by one from each other. An IR-active transition takes place when these conditions are fulfilled. In general, the absorbance of unpolarized light by randomly oriented molecules is given by the sum of the transition probabilities along all three Cartesian coordinates

$$A \propto \left([\mu_x]_{if}^2 + [\mu_y]_{if}^2 + [\mu_z]_{if}^2 \right). \quad (2.24)$$

Detailed information of a system can be achieved by using linearly polarized light with oriented molecules, since individual components of the transition dipole moment can be analysed.

1.2.1 Fourier-transform Infrared (FTIR) Spectroscopy

The two-beam interferometer designed by A.A. Michelson in 1891 is the basis for interferometers used for IR spectroscopy today.³ It is based on a Fourier-transform (FT) principle and allows for improvement of the signal-to-noise ratio (SNR) and reduction of the measuring time in comparison to the dispersive technique used previously.

Michelson Interferometer The Michelson Interferometer depicted in **Figure 2** builds an essential part in FTIR spectrometers. It divides the incoming radiation beam into two portions which are then later recombined with a phase difference between them. The difference in phase results in constructive or destructive interference of the beams. The interferometer operates in the following way: the beam splitter partially reflects and partially transmits radiation onto two plane mirrors, one fixed and one moveable. The mirrors are located perpendicular to each other. When the distance between the beam splitter and the two mirrors is identical, a phase difference of $\delta = 0$ occurs and the outgoing radiation is equal to the incoming one. When the mirror is displaced from this position, the recombined beams at the beam splitter interfere either constructively ($\delta = 2n * \frac{1}{2}\lambda$) or destructively ($\delta = (2n + 1) * \frac{1}{2}\lambda$).

Therefore a δ -dependent sinusoidal modulation of the respective wavelength λ occurs. The resulting interferogram **Figure 2 A** contains the superposition of the cosine function of all frequencies of the polychromatic IR radiation. Finally, to transform the path length dependent interferogram (time domain) into an IR spectrum **Figure 2 B** (frequency domain), a Fourier

2. Theoretical Background

transformation is used. The spectrum displays the attenuation of the IR radiation, with a dependence on the wavenumber:

$$I(\tilde{\nu}) = \int_{-\infty}^{+\infty} I(\delta) \cos(2\pi\tilde{\nu}) d\delta. \quad (2.25)$$

The moveable mirror can be moved at a constant velocity (continuous-scan interferometer), as was the case in this work. Theoretically, it is possible to measure the complete spectrum from 0 to $+\infty$ with an infinitely high resolution. However, this would require the moving mirror to be shifted from $\delta = 0$ to $+\infty$. Hence, measuring a spectrum over a limited distance a finite resolution requires that the edges of the interferogram are brought smoothly to zero. This is achieved by the multiplication of the interferogram with an apodization function, like a triangular function. Although artefacts can be suppressed, but this procedure affects the natural shape of the spectral bands.

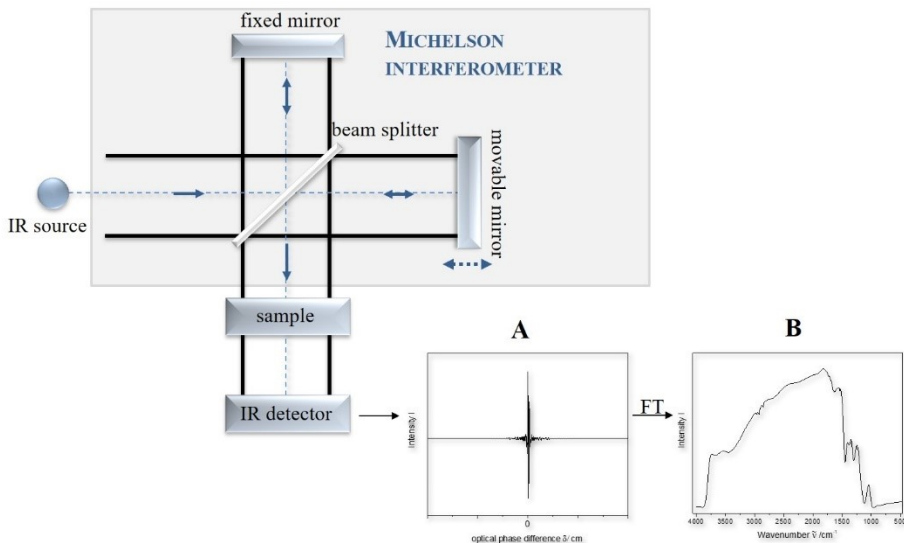


Figure 2: Schematic representation of a FTIR spectrometer with a beam splitter in the centre, a fixed mirror and a movable mirror. The recombined beams were diverted to the sample and afterwards to the detector. The interferogram (**A**) is Fourier transformed and the IR spectrum (**B**) is generated.

Advantages of the FTIR Spectrometer The FTIR spectrometer has multiple advantages compared with a dispersive spectrometer. The multiplex (Felgett) advantage is that it is possible to measure spectral information from all wavelengths simultaneously. Thus, the SNR ratio is improved by \sqrt{N} for a spectrum composed of N elements because the total noise is distributed over the entire spectral range. The throughput (Jacquinot) advantage describes the use of large apertures for FTIR spectrometers and consequently a greatly increased amount of IR radiation reaches the detector. The complete intensity of the IR radiation is detected. Another advantage is the internal calibration that provides a high wavenumber precision, also called the Connes advantage. It is provided by simultaneously measuring the interferogram of a HeNe laser.

1.2.2 Attenuated Total Reflection-IR (ATR-IR) Spectroscopy

ATR-IR spectroscopy is widely used and forms the basis of SEIRA spectroscopy, both of which were used in this work. In the ATR technique, the sample is in contact with a sensing element and the radiation is reflected from the surface. Consequently, the sample must not be thin or diluted. This allows even powders or solid materials to be measured, so long as the sample is in contact with the sensing element. Reflection of radiation occurs at an optical interface when it passes from one transparent medium to another with an abrupt change in the refractive index (n) of the media.

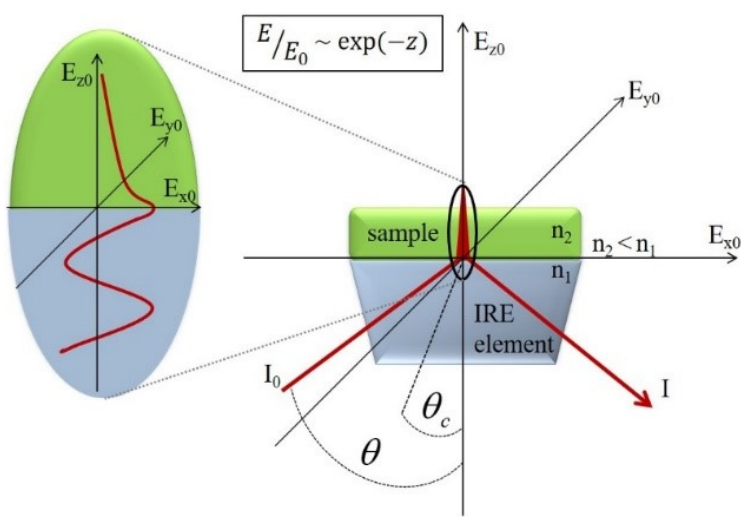


Figure 3: Attenuated total reflection at an IRE element with a propagation of an evanescent wave through the interface is shown. Achieving total reflection to an optical less dense medium ($n_2 < n_1$) the angle of incidence (θ) must be higher than the critical angle (θ_c). E describes the energy of the evanescent wave and E_{i0} ($i = x, y, z$) the energy of the evanescent wave at the interface and z the distance normal to the optical interface.

In the case of the ATR technique, total reflection needs to be achieved, which can only occur at the interface to a less optically dense medium ($n_2 < n_1$) when the angle of incidence (θ) is larger than the critical angle (θ_c)

$$\theta_c = \sin^{-1} \frac{n_2}{n_1}. \quad (2.26)$$

Therefore, the foundation of this technique relies on the use of an internal reflection element (IRE) or ATR prism; a schematic representation of the ATR-IR element is presented in **Figure 3**. Most organic compounds have a refractive index of $n_1 \sim 1.5$.³ Typical elements used as an IRE are silicon ($n_{\text{Si}} = 3.41$), germanium ($n_{\text{Ge}} = 4.00$) or zinc selenide ($n_{\text{ZnSe}} = 2.4$).³ A consequence of the internal reflection is the propagation of an evanescent wave through the interface caused by the electromagnetic field E of the radiation (perpendicular to the direction of the wave propagation) at the interface to the less dense media. The field strength of this wave decays exponentially in the direction normal to the optical interface (z) according to:

2. Theoretical Background

$$E = E_0 \exp\left(-\frac{z}{d_p}\right) \quad (2.27)$$

Here E_0 describes the field strength at the surface and d_p the depth of penetration at which the amplitude decays to $1/e$ (ca. 37%) of its intensity at the surface. This value is wavelength (λ) dependent and influenced by the ratio of the refractive indices of the IRE and the optically less dense media:

$$d_p = -\frac{\lambda}{2\pi\sqrt{\sin^2\theta - \left(\frac{n_2}{n_1}\right)^2}}. \quad (2.28)$$

As a rule of thumb the penetration depth lies in the range of the wavelength of the incident radiation. For instance, using an incident angle of 60° for a silicon prism, as was used in this work, and a spectral region of 1000 to 4000 cm^{-1} , a penetration depth of the evanescent wave between $2.6\text{ }\mu\text{m}$ and $0.7\text{ }\mu\text{m}$ is achieved. When adsorbing a molecule on the IRE it can couple with the electric field of the evanescent wave and absorb energy of the beam and consequently attenuate the totally reflected beam.

ATR is a technique that requires little sample preparation. As long as a sufficient contact area between the sample and the IRE is provided, spectra can be detected. The samples can also be measured in different surroundings allowing for an easily exchange of the buffer which in terms permits studies that are not possible in transmission experiments. Examples are pH-and ionic strength-dependent measurements, binding of substrates, cofactors or ligands; even reactions can be detected *in situ*. Since ATR is a surface-confined technique, surface-selection rules (see chapter 1.2.3 Surface-enhanced Infrared Absorption (SEIRA) Spectroscopy) can be applied and molecules or aggregates, like proteins or membranes, which exhibit preferential orientation on the IRE can be analysed with respect to their orientation.

1.2.3 Surface-enhanced Infrared Absorption (SEIRA) Spectroscopy

Using the ATR mode with an ATR-IR element which is coated by a metal island film, that can be treated as nanoparticles, the IR signal can be further enhanced up to a factor of 10^3 . This technique is called surface-enhanced infrared absorption spectroscopy, SEIRAS.¹⁶ The underlying effect was discovered by Harstein, Kirtley and Tsang in 1980 upon the study of aromatic carboxylic acids adsorbed on Ag and Au films.¹⁷ Among others, Osawa et al. carried out fundamental work to understand this effect.^{16,18} These authors discovered that at least two different mechanisms, electromagnetic and chemical, are responsible for the enhancement, but the electromagnetic mechanism is the dominant one.¹⁶ Both mechanisms consist of two components. The electromagnetic mechanism is based on plasmon resonance and the perturbation of the optical properties. The chemical mechanism can be attributed to donor-acceptor interactions and charge-transfer effects. SEIRA is strongly dependent on the angle of incidence and the polarization of the IR radiation.¹⁰ P-polarized light and large angles of incidence lead to a strongly enhanced IR signals, whereas for interactions with s-polarized light no enhancement occurs.

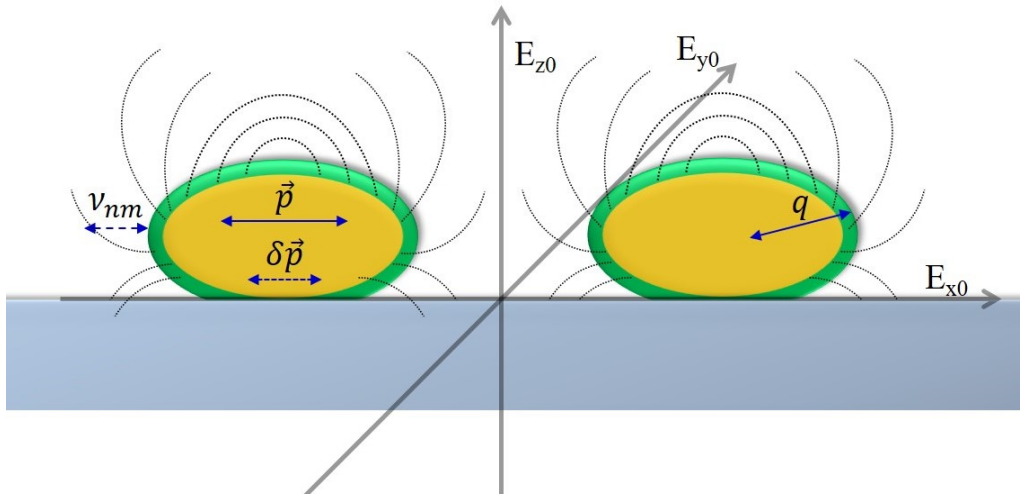


Figure 4: Mechanism of surface-enhanced IR spectroscopy based on a nanostructured Au film on an IRE element. Left, the vibrations of the adsorbed molecules (v_{nm}) lead to an oscillating dipole and induce a dipole in the metal particles ($\delta\vec{p}$) resulting in a change of the dielectric function. In addition, due to the polarization of the metal particles, an induced electric field around the particles is generated. On the right, the chemical enhancement based on donor-acceptor interactions or charge-transfer effects between the molecules and the metals is represented.

Electromagnetic Mechanism Initially, an induced electromagnetic field ($\overrightarrow{E_{ind}}(v_0)$) is generated, caused by the incident radiation and leads to an *excitation of collective electron resonance (local plasmon modes)*. Thus, a polarization leads to an induced dipole moment ($\vec{\mu}_{ind}$) in the metal particles. Consequently, the local electric field ($\overrightarrow{E_{loc}}(v_0)$) at the metal islands consists of an additional induced electric field and the incident electric field $\overrightarrow{E_0}(v_0)$

$$\overrightarrow{E_{loc}}(v_0) = \overrightarrow{E_0}(v_0) + \overrightarrow{E_{ind}}(v_0). \quad (2.29)$$

Therefore, the frequency of the incident light plays an important role. It must match to the frequencies of the plasmons to generate a large, short-range enhanced local electric field that then excites the molecular vibrations. The enhanced electric field is polarized along the surface normal and decays very sharply with the distance (d) from the surface

$$|\overrightarrow{E_{ind}}(v_0)|^2 = \frac{4\vec{\mu}_{ind}}{d^6}. \quad (2.30)$$

The enhancement factor (EF) at the distance d to the surface of a nanoparticle with the radius a_0 can be described as:

2. Theoretical Background

$$EF = EF(0) * \left(\frac{a_0}{a_0 + d}\right)^6. \quad (2.31)$$

Thus, all vibrations, whose transition dipole moment is aligned perpendicularly to the surface, parallel with the electric field, are the most enhanced. With the use of this *surface selection-rule* the alignment of the molecules on the surface can be studied.^{19–21}

This effect of the excitation of collective electron resonance or local plasmon modes only accounts for an enhancement of 10-fold or less. Therefore, a further electromagnetic mechanism must be involved in this process to account for the observed enhancement factor. If molecules are adsorbed on the metal islands their oscillating dipole, due to the molecular vibration, can induce dipoles ($\delta\vec{p}$) in the metal particles and *perturb the optical properties* of the metal island films such that the dielectric function is changed. (**Figure 4**) The perturbation leads to a change of the transmittance and reflectance of the film at the frequencies of the vibrations. The metal islands film function as an amplifier of the IR absorption.

Chemical Mechanism The chemical enhancement is based on *donor-acceptor interactions* between the chemisorbed molecules and the metal. Chemisorption changes the polarizability of the molecules; therefore, the enhancement for chemisorbed molecules are larger than for physisorbed ones. In addition, the chemical enhancement is generated by a *charge-transfer effect*. Charge oscillates between the molecular orbitals of the adsorbate and the metal might increase the absorption coefficient.

2. Electrochemical Impedance Spectroscopy

In 1880 electrochemical impedance spectroscopy (EIS) was first introduced by Oliver Heaviside. It is a valuable analytical tool in material research.²² The application of EIS extends in many different areas like studies of corrosion, electronic and conducting polymers, colloids, coatings, energy storage, batteries, fuel cells-related systems, biomedical sensors, semiconductors or electrochemical kinetics. Likewise, the adsorption, charge and mass transport of molecules can be analysed. It is a non-invasive technique. The disadvantage of EIS is the complex data interpretation. It involves the sophisticatedly correlation between the values obtained from EIS measurements with practical physical, chemical, electrical or mechanical parameters. There are many ways to present the EIS data. For the analysis electric circuit models are used. It is not trivial to choose the right model for each experimental case. In this work, EIS was applied to study the electronic properties of the interfaces explained in chapter 3.3.

2.1 Theory of EIS

According to Ohm's Law an ideal resistor follows the relation:

$$R = \frac{U}{I} \quad (2.32)$$

with the voltage U and the current I .²² The resistance R is independent of an AC frequency that causes the sinusoidal functions of the voltage and the current are in phase for an ideal resistor. In contrast, an ideal capacitor repels any flow of current, thereby the AC current and voltage signals are out of phase with each other. In a plate capacitor the relation of the capacitance (C) with the area (A) and distance (d) of the electrodes is given by.

$$C = \varepsilon_0 \varepsilon_r \frac{A}{d}, \quad (2.33)$$

where ε_0 is the electrical permittivity constant in vacuo ($8.85 \times 10^{-14} \frac{F}{cm}$) and ε_r the relative permittivity of the material (it reflects the ability to store electrical energy). In EIS experiments an alternate voltage ($U(t)$) is applied to the interface and the responding current ($I(t)$) is detected

$$U(t) = U_0 * \sin(\omega t) \quad (2.34)$$

$$I(t) = I_0 * \sin(\omega t + \delta). \quad (2.35)$$

Here δ describes the phase angle of the current in comparison to the voltage. Analogous to Ohm's Law (equation (2.32)) the complex impedance ($Z^*(t, \omega)$) can be described as the ratio of the input voltage ($U(t, \omega)$) and the output current ($I(t, \omega)$)

$$\begin{aligned} Z^*(t, \omega) &= \frac{U(t, \omega)}{I(t, \omega)} = \frac{U_0 * \sin(\omega t)}{I_0 * \sin(\omega t + \delta)} = \frac{U_0}{I_0} * \frac{\sin(\omega t)}{\sin(\omega t + \delta)} \\ &= Z(\omega) * \frac{\sin(\omega t)}{\sin(\omega t + \delta)}. \end{aligned} \quad (2.36)$$

During an experiment the magnitude of the impedance ($|Z|$) the phase angle and the circular frequency (ω) is detected. With the complex representation ($\exp(j\delta) = \cos(\delta) + j\sin(\delta)$) the impedance can be expressed as:

$$Z^*(t, \omega) = Z(\omega) * e^{j\delta} = Z(\omega) \cos(\delta) + i Z(\omega) \sin(\delta) = Z_{Re} + i Z_{Im}. \quad (2.37)$$

The complex impedance ($Z^*(t, \omega)$) can be divided into a real (Z_{Re}) and an imaginary (Z_{Im}) part. The ratio of these parts is used calculating the phase angle

2. Theoretical Background

$$\delta = \arctan\left(\frac{Z_{Im}}{Z_{Re}}\right). \quad (2.38)$$

The impedance indicates the frequency-dependent resistance. Whereas, the frequency-dependent conductance can be described with the admittance (Y) and is expressed as the inverse impedance

$$Y = \frac{1}{Z} = \frac{1}{Z_{Re} + jZ_{Im}} * \frac{Z_{Re} - iZ_{Im}}{Z_{Re} - iZ_{Im}} = \\ \frac{Z_{Re}}{Z_{Re}^2 + Z_{Im}^2} + i \frac{-Z_{Im}}{Z_{Re}^2 + Z_{Im}^2} = Y_{Re} + iY_{Im}. \quad (2.39)$$

Analogous to the complex impedance, the admittance can be divided up into a real (Y_{Re}) and an imaginary (Y_{Im}) part.

2.1.1 Equivalent Circuits

Applying a sinusoidal voltage to a pure resistor R the complex impedance $Z^*(t, \omega)$ is resistive and its magnitude $|Z|$ corresponds to the value R at all circuit frequencies (and is therefore frequency-independent)

$$Z^*(t, \omega) = R, \quad |Z| = R. \quad (2.40)$$

Taking account of a pure capacitor the complex impedance and the magnitude of the complex impedance is frequency-dependent

$$Z^*(t, \omega) = (i\omega C)^{-1}, \quad |Z| = (\omega C)^{-1}. \quad (2.41)$$

In this case the detected impedance is capacitive. For the analysis of EIS data in real systems no ideal resistor or capacitor can be assumed. Thus, a combination of resistive (R) and capacitive (C) elements in an equivalent circuit are applied. In the simplest case of a parallel R/C circuit (Figure 5) the potentials across both circuit elements are equal but the total current can be calculated from the sum of the currents flowing through the electrical elements (Kirchhoff's law).

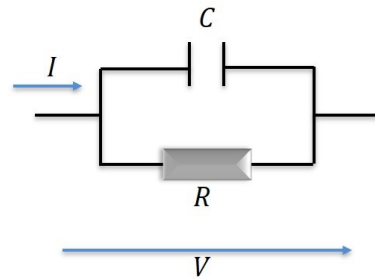


Figure 5: Simplest case of a parallel R/C circuit, the voltage (V) is equal at both circuit elements.

2.1.2 Graphical Data Representation^{23,24}

There are many ways to represent EIS data graphically. In this work, only a normalized admittance plot is used and will be explained in this part. This plot is based on the Cole-Cole plot, investigated by Kenneth S. Cole and Robert H. Cole, representing the frequency-dependent permittivity of the material²³

$$\varepsilon(\omega) = \varepsilon_{Re} + i\varepsilon_{Im}. \quad (2.42)$$

Here ε_{Re} represents the real (x-axis) and ε_{Im} the imaginary (y-axis) part of the permittivity plotted as a function of the frequency.^{23,25} The dielectric constant of liquids and solids was found to be frequency-dependent. In the Cole-Cole plot a semicircle between two permittivity limits (the static value ε_0 and the limiting permittivity ε_∞ at high frequencies) is observed. Taking the relation of the relative permittivity and the frequency-dependent permittivity into account

$$\varepsilon_r = \frac{\varepsilon(\omega)}{\varepsilon_0}. \quad (2.43)$$

equation (2.33) can be transformed to

$$C(\omega) = \varepsilon(\omega) \frac{A}{d}. \quad (2.44)$$

In this work the capacity of different systems was analysed. With the assumption of an ideal capacitor for the system, the admittance (which is the reciprocal of the complex impedance equation (2.39)) is

$$Y(\omega) = C(\omega)\omega i. \quad (2.45)$$

Inserting equation (2.44) in equation (2.45) leads to a relation between the frequency-dependent admittance and the frequency-dependent permittivity

2. Theoretical Background

$$Y(\omega) = \varepsilon(\omega) \frac{A}{d} \omega i. \quad (2.46)$$

In comparison to the Cole-Cole plot (permittivity plot), the normalized admittance plot displays the real part of the admittance ($\frac{Y_{Re}}{\omega A}$) versus the imaginary part ($-\frac{Y_{Im}}{\omega A}$), both divided by the circular frequency and the electrode area (the distance between the electrodes are negligible cause the spectro-electrochemical measurements are done in solution).

$$\varepsilon(\omega) = \frac{Y(\omega)}{A\omega i} = \frac{C(\omega)}{A}. \quad (2.47)$$

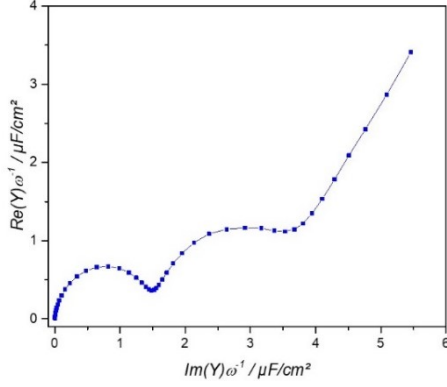


Figure 6: Normalized admittance plot used in this work to interpret EIS data, the capacitance per area of the system is shown by the diameter of the semicircle.

In consideration of **equation (2.47)** the capacitance per area of the system is shown by the radius of the semicircle (or better the diameter).^{10,26} In **Table 1** the relations between the complex impedance $Z^*(t, \omega)$, complex admittance $Y^*(t, \omega)$, permittivity $\varepsilon(\omega)$ and capacity $C(\omega)$ are summarized.

Table 1: Overview of different parameters used for EIS and their relation to each other.

	Complex impedance $Z^*(t, \omega)$	Complex admittance $Y^*(t, \omega)$	Permittivity $\varepsilon(\omega)$	Capacity $C(\omega)$
$Z^*(t, \omega)$	--	$Y^*(t, \omega)^{-1}$	$\left(\frac{A}{d}\varepsilon(\omega)\omega i\right)^{-1}$	$(C(\omega)\omega i)^{-1}$
$Y^*(t, \omega)$	$Z^*(t, \omega)^{-1}$	--	$\frac{A}{d}\varepsilon(\omega)\omega i$	$C(\omega)\omega i$
$\varepsilon(\omega)$	$Z^*(t, \omega)^{-1}(A\omega i)^{-1}$	$Y^*(t, \omega)(A\omega i)^{-1}$	--	$C(\omega)A$
$C(\omega)$	$Z^*(t, \omega)^{-1}(\omega i)^{-1}$	$Y^*(t, \omega)(\omega i)^{-1}$	$\varepsilon(\omega)A$	--

2.1.3 Constant Phase Element

As above-mentioned, for real life systems no ideal capacitor or ideal resistor elements can be used. Therefore, a constant phase element (CPE) was developed for the interpretation of EIS data.²² The impedance of the CPE depends on an effective CPE coefficient Q and a factor α

$$Z_{CPE} = \frac{1}{Q(\omega i)^\alpha} = \frac{1}{Q\omega} (\cos(\alpha\omega) - i\sin(\alpha\omega)). \quad (2.48)$$

If and $\alpha = 1$ the CPE element corresponds to an ideal capacitor ($Q = C$). For the case that $\alpha = 0$ an ideal resistor is obtained with $Q = 1/R$. Using the CPE element, the data of the normalized admittance plot can be explained as well

3. Biomimetic Interfaces

It is important to understand biological processes occur at the membrane interface to get a better insight into protein reactions and their mechanisms in and at the membranes. Using biomimetic interfaces is a powerful way to study these processes. For instance, they can consist of self-assembled monolayers on substrates.²⁷ This depicts the simplest case of a biological membrane with a head group region and a hydrocarbon interior. The membrane can be functionalized by choosing different molecules. Furthermore, an artificial bilayer lipid membrane can be structured on a self-assembled monolayer. The properties of different biomimetic interfaces are explained in this chapter.

3.1 Self-assembled Monolayer - SAM

The structure of chemisorbed long alkyl chain molecules on gold was first described by Nuzzo and Allara in 1983. This observation established the foundation of studies with self-assembled monolayers (SAM), which combine surface science with the flexibility of organic chemistry²⁸⁻³⁰. SAMs are based on surface-active molecules creating well-defined reproducible synthetic surfaces with known molecular and macroscopic parameters. They became an important tool in surface science since the preparation is easy and no specialized equipment is necessary. It is possible to form nanostructured thin films of 1-3 nm thickness to study heterogenous catalysis, electron transfers, growth of mammalian cells or study the wetting, adsorption and interactions with molecules especially biomolecules.²⁹ SAMs can provide a link to the environment studying its electronic (electrochemistry) or optical properties (surface-plasmon studies). It is common to use metal coated silicon, glass, mica or plastic as substrates. A thin metal film is generated with physical vapor deposition (PVD) or electroless deposition. By controlling the surface

2. Theoretical Background

composition structure-property relationships are investigated. For surface structure and macroscopic property studies different tools are applicable: surface reflectance IR, scanning probe microscopy, contact angle goniometry, ellipsometry, electrochemistry etc.. At the moment, the best theoretical and practical described systems consist of n-alkyl thiol ($HS - C_n - X$) or disulphide ($X - C_n - S - S - C_m - X$) monolayers on an Au or Ag substrate. The head group X defines the surface and interface properties and therefore they functionalize (charged, polarity, binding sites) the support material. For wetting, simple head groups (-CH₃, -OH) are used but for other applications in nanotechnology or biology various SAMs are required including organometallic complexes, aromatic hydrocarbons, biomolecules or ligands for proteins.^{6,11} These surfaces are more complicated and not accurately characterized. Using a mix of two different SAM molecules lead to a phase separation on the substrate with a scale diameter of ~ 100 nm².³¹ The disadvantages by working with SAMs are their relatively low thermal and mechanical stability and the creation of defects in the surface. In this work we use the biomimetic and biocompatible nature of n-alkyl thiol molecules and functionalize them with electric-field reporter groups.^{11,21,32,33}

3.1.1 Structure of Self-assembled Monolayers

SAM molecules consist of three components: (1) a linking group with a high affinity to bind to the substrate, like sulphur for gold or silver, (2) a spacer that is typically an alkyl chain and (3) a functionalized head group, like -CH₃, -COOH, -OH, -NH₂, -CN etc. (Figure 7).²⁹ The molecules form spontaneously a monolayer on the substrate with a defined tilt angle α with respect to the normal of the surface. Self-assembled on a surface the molecules can still rotate (torsion angle, β). We will focus on the structural properties of n-alkyl thiols on Au (111) surfaces because they are best characterized.

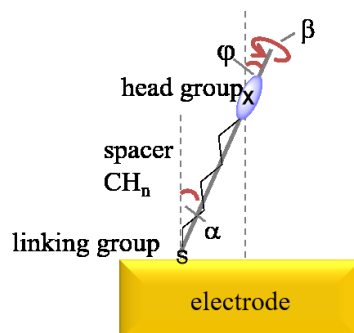
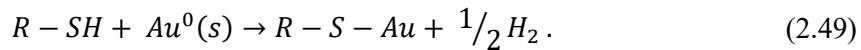


Figure 7: An electrode with a SAM and its three components are shown (the linking group, the spacer and the head group). Three angles define the structure of a SAM: (1) α the tilt of the molecule axis with respect to the surface normal (2) β defines the rotation of the SAM around its molecular axis and (3) φ as the tilt angle of the head group with respect to the surface normal.

The n-alkyl thiols orient with the linking group to the surface and a freely movable head group. For the formation of a SAM a chemical activation of the S-H (thiol) or S-S (disulphide) bond is necessary. Investigations showed a homolytic Au-S bond with a strength of ~ -50 kcal/mol (for comparison, S-S ~ -62 kcal/mol)^{30,34}. However, it is still not unequivocally determined what happens with the hydrogen atom.^{35,36} It seems to be that dihydrogen is formed due to³⁷



In vacuo the reductive elimination of H_2 is weakly activated whereas in aqueous solutions an oxidative conversion to water could take place. Absolutely, the Au-S bonding interaction is important for the creation of the SAM.

The sulphur binds in threefold hollows in the gold lattice and so the sulphur atoms occupy a circular area with a diameter of about 5 Å. This causes a lattice spacing in the molecular crystal of the Au and has a large effect on the van-der-Waals (VdW) interactions between the alkyl chains. To maximize the attractive VdW interactions the molecules tilt on Au by about $\sim 30^\circ$ (for $n \geq 11$, $n \leq 10$ forms more disordered structures).²⁹ Different tilt angles could be observed for other metals like Ag ($0\text{-}12^\circ$)^{38,39}, Cu (12°)⁴⁰ or Pt ($<15^\circ$).⁴¹ (**Table 2:**) The strength of VdW interactions lead to a preferential alignment in an all-trans conformation of the chains.

Table 2: Collection of tilt angles α on Ag and Au substrates of aromatic and aliphatic SAMs.

SAM	Tilt angle α on a metal substrate		Method	Reference
	Ag	Au		
Thiophenol	27°		SERS	Han et al 2001 ⁴²
Thiophenol	24°	49°	NEXAFS	Frey et al 2001 ⁴³
Thiophenol		54°	NEXAFS	Käfer et al. 2007 ⁴⁴
MBN	0°	40°		Au: Ballav et al. 2007 ⁴⁵ Ag: Shaw et al. 2009 ⁴⁶
HS-(CH ₂) ₁₇ -CH ₃	13°		IR-RAS	Laibinis et al. 1991 ³⁹
HS-(CH ₂) ₁₅ -CH ₃	11°		IR-RAS	Laibinis et al. 1991 ³⁹
HS-(CH ₂) ₁₉ -CH ₃	14°		IR-RAS	Laibinis et al. 1991 ³⁹
HS-(CH ₂) ₁₅ -CH ₃		40°	IR-RAS	Nuzzo et al. 1990 ⁴⁷
HS-(CH ₂) ₁₅ -CO ₂ CH ₃		38°	IR-RAS	Nuzzo et al. 1990 ⁴⁷
HS-(CH ₂) ₁₅ -CO ₂ H		32°	IR-RAS	Nuzzo et al. 1990 ⁴⁷
HS-(CH ₂) ₁₅ -CONH ₂		31°	IR-RAS	Nuzzo et al. 1990 ⁴⁷
HS-(CH ₂) ₁₅ -OH		28°	IR-RAS	Nuzzo et al. 1990 ⁴⁷

Disulphides and thiols showed similar surface structures on Au and Ag.^{48,49} It should be noted that monomers with large head groups cannot assemble in such well-ordered structures. Also defects can occur in n-alkyl thiol films.²⁹ Disordered boundaries within the SAM or vacancy island in the substrate surface can lead to defects in the monolayer. These disordered regions could conceivably have a significant effect on the overall structure. This is further important for

2. Theoretical Background

studies like wetting or adhesion but might also be a problem in electrochemistry (current-voltage) studies. SAM formation is achieved in most cases via incubation from ethanolic solutions. After the preparation of the Au support, materials from the atmosphere adsorb quickly on the surface. Hence, during the incubation the monomers must displace these materials and the solvent molecules on the surface. The majority of the SAMs adsorb rapidly and a 90 % coverage is obtained in 5-6 minutes. A low mass coverage with striped layers is observed followed by a dense upright layer formation. Secondly, the alkyl chains unfold to the all-trans conformation. This process is 3-4 times slower than the first one. The molecules reorder to maximize the VdW interactions and additional monolayers adsorb on the surface to create a well-packed system. Finally, the gauche defects disappear within 7 hours. Nevertheless, at the end there are still some gauche defects in the equilibrium state.

3.1.2 Biochemical and Biological Applications of Self-assembled Monolayers

In studies with biological systems often large, delicate and water-soluble ligands are used. The characteristic binding events of biological molecules, like proteins, can be studied with surface-plasmon resonance, ellipsometry or mass spectrometry. Also, inert surfaces can be created to prevent an adsorption of proteins from solution and an attachment of cells. The structure (hydrophobic hydrocarbon part and functionalized headgroup) and electrostatics at the interface of a phospholipid bilayer can be mimicked by alkyl thiol SAMs. Additionally, the head groups can be used as sensors e.g. for the electric field as done in this work.

3.2 Membrane Systems

Biological membranes are essential for cells. A 30 Å hydrophobic film isolates different environments from each other and protects the inside of the cell. Cellular communication and transportation across the membrane is a complex mechanism and essential for the cell. Further important membrane-based processes include ligand-receptor interactions and enzymatic reactions. Artificial membranes immobilized on solid surfaces are necessary to study these processes.²⁷ They are optimized to feature a high long-term and mechanically stability and allow studies with surface-sensitive analytical techniques (AFM and other microscopic techniques, fluorescence, surface-enhanced spectroscopy, ellipsometry, SPR). Artificial membranes consist of lipids which have the property to self-organize into specific supramolecular aggregates based on their amphiphilic nature. In the following chapter lipid properties and different artificial membranes are introduced.

3.2.1 Lipids – The Fundamental Building Block of a Biological Membrane

Eukaryotic cells create thousands of different lipids to generate various functionalized membranes. Basically, lipids have three functions: (1) they store energy, (2) they segregate internal components from the external environment and (3) they function as the platform for signal transduction. The phase behaviour of lipids is rather complex since they can adopt a fluid

or a solid state. The different phases are coined by the spatial arrangement and mobility of each lipid with respect to its neighbour. In the fluid phase the acetyl chains have a low order parameter and they exhibit fast translation diffusion. In contrast, in the solid phase, the order parameter is high and the translation diffusion slow. For different lipid compositions the temperature of the phase transition varies. In some special cases two existing fluid phases, a liquid ordered and liquid disordered phase, can occur characterized by specific lipid-lipid interactions like for phospholipids and cholesterol.⁵⁰ The major lipids in nature are phospholipids besides sphingolipids or sterols, like cholesterol.

The amphiphilic structure of lipids is essential for the self-organisation in specific supramolecular aggregates. The hydrophobic tails and the hydrophilic head group can spontaneously adopt different shapes.

3.2.2 Phospholipids

Structure Phospholipids consist of three parts: (1) the hydrophilic head group (2) a connecting backbone and (3) the hydrophobic alkyl chain. (**Figure 8**) Various variants of lipids are possible by combining different head group/tail combinations. Some common head groups are phosphatidylcholine (PC), phosphatidylglycerol (PG), phosphatidylserine (PS) or phosphatidylethanolamine (PE). The charge of the head group (zwitterionic, positive or negative at physiological pH) defines the property of the lipid. Glyceryl groups form the connecting backbone between the phosphate group of the head group and the two alkyl chains. Saturated or cis-unsaturated fatty acids at different lengths build the hydrophobic part. Intrinsic parameters as the polarity, size and charge of the head group as well as the branching and the presence and location of double bonds in the chain define the behaviour of the lipids in aqueous solutions likewise extrinsic parameters: pH, concentration and temperature (lyotropic and thermotropic respectively) of the solution.

Self-assembly In aqueous solutions lipids spontaneously self-assemble in mesophase structures like monolayers, bilayers, micelles, reverse micelles or in a hexagonal phase. The driving force for this fundamental behaviour of the lipids is the hydrophobic effect. Due to the self-assembly the entropy is minimized by the arrangement of water dipoles around the alkyl chains. The shape of the structures is given by the shape factor P , which is the ratio of the volume of the alkyl chains V_c and the product of the head group area A_0 and the effective alkyl chain length l_c :

$$P = \frac{V_c}{A_0 * l_c}. \quad (2.50)$$

2. Theoretical Background

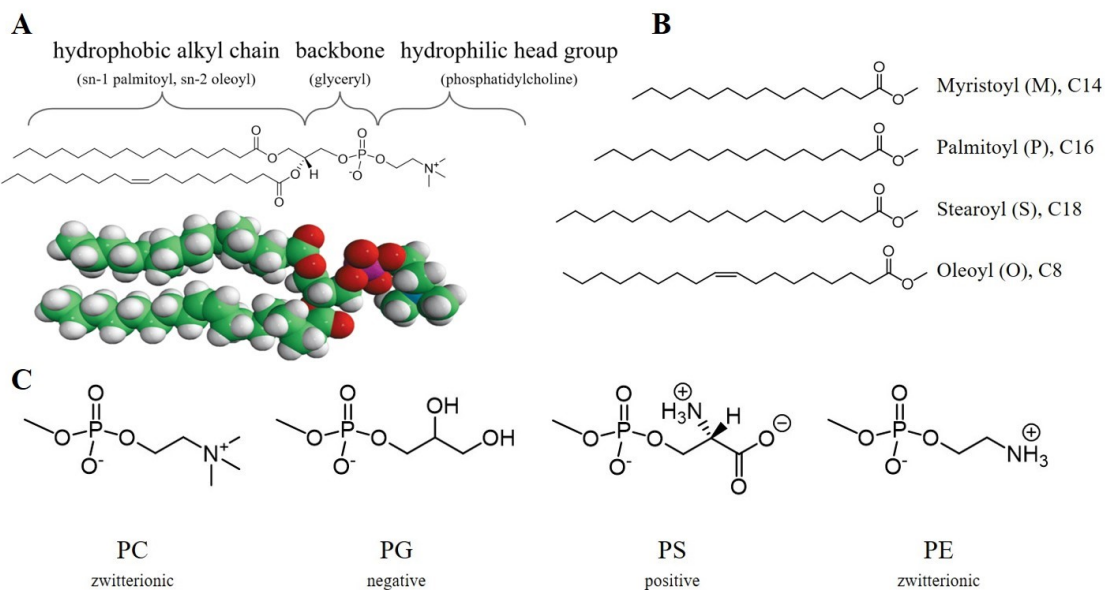


Figure 8: (A) A phospholipid with a hydrophilic head group, a backbone and a hydrophobic alkyl chain is shown in chemically (top) and in a 3D-structure (bottom). (B) Structure and nomenclature of common alkyl chains in phospholipids are presented. (C) Structure and nomenclature of common head groups in phospholipids are presented.

If $P < 1$ micelles are formed (the lipids adopt a triangular geometry), for $P \approx 1$ lamellar bilayers or vesicles are created (cylindrical geometry) and for $P > 1$ inverted micelles (trapezoidal geometry) are generated. The melting temperature or transition temperature T_m in bilayers increases with a longer alkyl chain. Unsaturated bonds in the alkyl chain disrupt the molecular packing and T_m is increased. Likewise, interactions between the head groups and the water molecules influence the phase behaviour. Due to the ordered structure and properties of the lipids the membrane has a highly selected permeability. Water can pass the membrane rather fast ($30\text{-}40 \mu\text{m/s}$) in comparison to sodium or chlorine ions ($10^{-10} \mu\text{m/s}$ and $10^{-7} \mu\text{m/s}$ respectively). Also, the composition of the membrane defines the permeability.

3.2.3 Transmembrane Potential

The transmembrane potential ($\Delta\phi$) is due to different ion concentrations (cations and anions) of the two bulk phases separated by the bilayer membrane. It can regulate the function of membrane proteins like ion channels. The site of action of the transmembrane potential is inside the membrane or at the membrane solution interface. The electric field created by the potential is responsible for conformational changes of membrane proteins and the distribution of charged substrates at the interface. A transmembrane potential of 100 mV creates a global electric field across a 4 nm bilayer of 0.25 MV/cm. Also, other potentials are generated at a bilayer membrane and influences biological processes. Any charged or dipolar group of a lipid influences the membrane conformation. The charges of the lipid head groups (zwitterionic, positive or negative), water dipoles and dipolar lipids are not uniformly distributed across the membrane. Therefore, the electric potential does not change linearly through the membrane but followed by a complex profile shown in **Figure 9**. In summary, three electrical potentials occur at a lipid bilayer: (1) the transmembrane potential ($\Delta\phi$), (2) the surface potential (ϕ_S) and (3)

the dipole potential (ϕ_D). The surface potential (ϕ_S), about 8-30 mV, occurs at the charged head groups and controls the concentration of ions on the lipid/solution interface. The dipole potential (ϕ_D) (220-280 mV) is due to the alignment of polar lipid residues and/or water dipoles in the head group region between solution and alkyl chains.^{51,52} The transmembrane potential can be measured by inserting two electrodes inside the bulk phases. For the determination of the surface potential the ζ -potential of the layer can be investigated by electrophoretic measurements. The analysis of the dipole potential is more complicated and harder to measure. However, with indirect experimental methods and theoretical calculations it can be quantified.

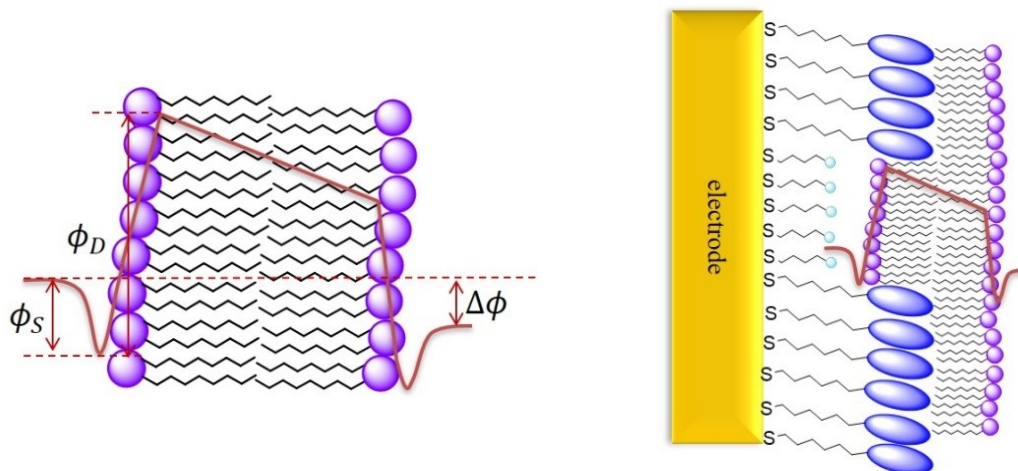


Figure 9: The potential distribution across a bilayer lipid membrane (left) and the potential distribution across an artificial membrane on an Au substrate consisting of a mixed SAM and phospholipids on top (right).

3.2.4 Solid Supported Membranes

In the 1960s Mueller et al. investigated the first biomimetic membrane, the black lipid membrane.⁵³ It consists of a bilayer between two solution chambers, thus including two large water reservoirs at both sides of the membrane. Unfortunately, these membranes are not very stable and 20 years later the first solid supported bilayer membrane was constructed. Thus, artificial membranes immobilized on appropriately substrates like glass, mercury, gold or silver are a promising tool to investigate structure-function relationships of membranes and proteins. Additionally, detailed information about physical properties can be obtained. Solid supported membranes are featured with a relatively high long-term and mechanically stability. A large number of surface analytical techniques can be applied to study these membranes, e.g. electrochemical methods (EIS, chronoamperometry), spectroscopic techniques (SPR, surface-enhanced vibrational spectroscopy, PM-IR-RAS), neutron scattering or surface imaging methods. For the formation of the bilayers different techniques are used like the fusion of vesicles or the Langmuir-Blodgett (LB) method also in combination with the Langmuir-Schaefer technique (LS) and will be described shortly:

- Fusion of vesicles

Lipid vesicles on a hydrophilic surface start to deform and finally rupture due to adhesion forces. The lipids are spread across the surface and based on the hydrophobic effect, a compact monolayer or bilayer is formed. Various factors as the vesicle size, temperature, presence of cations as well as the surface charge, surface roughness, pH,

2. Theoretical Background

ionic strength and the phase of the lipid inside the vesicles can influence the spreading. A great advantage with respect to the LB-LS technique is that membrane proteins can be directly incorporated inside the vesicles and thus inserted into the membranes

- LB and a combination with the LS technique

Using the LB technique, a layer-by-layer transfer of lipid monolayers from the air-water interface onto the substrate is carried out. The solid substrate is faced to a lipid monolayer covering a water surface. The monolayer is transferred onto the substrate by traction and immersion through the water-air interface. Thereby two layers are formed, a support-facing layer and a solution-exposed layer. An alternatively way creating a bilayer is the horizontal push of the substrate on the water covered surface (combined LB-LS). Because of the layer-by-layer structure an asymmetrical bilayer of the inner and outer leaflet of the bilayer can be formed by using different monolayers. With this method less defects compared to the vesicle fusion are obtained.

In the following section five different artificial solid membrane models such as supported lipid monolayers (sLM), hybrid bilayer lipid membranes (hBLM), supported bilayer lipid membranes (sBLM), tethered bilayer lipid membranes (tBLM) and floating bilayer lipid membranes (fBLM) are described (**Figure 10**):²⁷

- Supported lipid monolayers

In the beginning sLMs were formed on liquid mercury because the fluidity of the substrate is compatible with the fluidity of an adsorbed lipid monolayer. The lipid monolayers on the substrate were defect-free, self-sealing and impermeable for ions. An extruding mercury drop is covered by a lipid monolayer by spreading of the lipids at the air/solution interface. In case of Au as a substrate the fusion of vesicles are used and with additional molecules a bilayer can be formed.

- Hybrid bilayer membranes

The substrate is structured by a SAM of alkanethiols, aromatic thiols or lipid thiols and on top a phospholipid layer is generated. Long alkanethiols like 1-octadecanethiol form well-ordered and highly packed monolayers. The outer lipid leaflet can be created by vesicle fusion, LS-LB or membrane painting. By modifying the SAM in chain length and the lipids in head groups and alkyl chains, membranes with various properties in thickness, capacitance, phase and lipid symmetry can be formed. Adding ethylene oxide, a separated bilayer from the surface is formed due to the small space between the SAM and the electrode. HBLMs are easy to form and can be constructed with different components. Hence, various biomimetic membranes can be formed by changing the proximal SAM or distal phospholipid. A disadvantage is the reduced fluidity of the membrane and its environment which causes a more crystalline phase. Also, it is difficult to study transmembrane proteins since the aqueous solution is only at the outer leaflet of the bilayer.

- Supported bilayer lipid membranes

This kind of planar lipid bilayer is directly adsorbed on the substrate. Phospholipids build the proximal and distant leaflet of the bilayer. Both fusion of small unilamellar vesicles (SUV) and the LB-LS technique can be applied. The electric field of the sBLM (10^7 - 10^8 V/m) is similar to the one in native systems.⁵² The attachment of the lipids on the surface is dependent on the charge density of the substrate and can be studied by SEIRAS and neutron reflectometry. With this system the effect of the electric field on orientations and conformation changes of the membrane and proteins can be studied. A

disadvantage is again the low fluidity of the membrane and the asymmetric environment, since the inner leaflet is physically adsorbed on the surface and the outer one is exposed to the electrolyte. Also, this membrane does not allow studying transmembrane proteins.

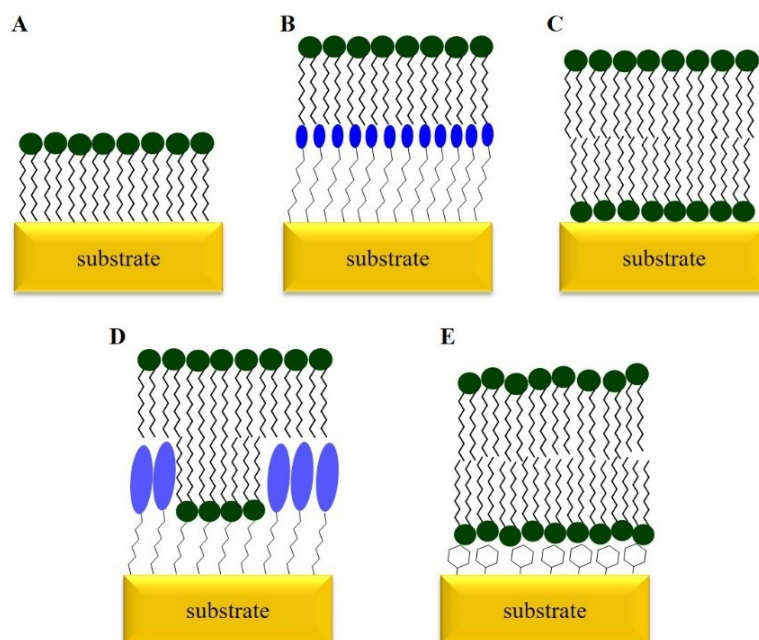


Figure 10: Five different biomimetic solid membrane models are shown: (A) supported lipid monolayer (sLM), (B) hybrid bilayer lipid membrane (hBLM), (C) supported bilayer lipid membrane (sBLM), (D) tethered bilayer lipid membrane (tBLM) and (E) floating bilayer lipid membrane (fBLM).

- Tethered bilayer lipid membranes

TBLMs are a combination of hBLMs and sBLMs. The bilayer is separated from the substrate by a hydrophilic spacer. For this spacer thiol-lipid derivates are used and consist of three parts: (1) the thiol or disulphide tail group, (2) a hydrophilic spacer and (3) a hydrophobic tail. Thus, a water rich region between the hydrophobic bilayer and the surface is created. The inner leaflet is self-assembled on the substrate and for the outer leaflet vesicle fusion or rapid solvent exchange can be applied. Increasing the water region, a second short hydrophilic self-assembled monolayer can be added to the lipid thiol. Because of the phase separation, rafts of the respective SAM are formed on the surface followed by fusion of vesicles. The inner lipid layer consists of thiol lipids and phospholipids and the outer leaflet just includes phospholipids from the vesicles. Thus, a quasi-free-standing PC-PC bilayer is surrounded by a PC-lipid thiol hybrid layer. Membrane active proteins (ion-channels or redox enzymes) and also transmembrane proteins can be analysed with this system and characterized by their resistance and capacitance. A disadvantage is the complex synthesis of the thiol lipids and the constrained mobility because the diffusion coefficient of the proximal leaflet is smaller than for the distal side.

2. Theoretical Background

- Floating bilayer lipid membranes

This system improves the fluidity and mobility of the membrane lipids a lot. It consists of a separate bilayer on a water rich lubricant like a water rich polymer or hydrogel film on a non-conductive substrate. The LB-LS technique is used for the water layer and a PEG molecule can be added to the proximal leaflet to increase the water layer.

In this work we used a tBLM system consisting of a mixed monolayer of dihydrocholesteryl (2-(2-(2-ethoxy) ethoxy) ethanethiol (WK3SH), a cholesteryl derivate, and 6-mercaptophexanol (6MH) or 4-mercaptopbenzonitrile (MBN) containing hydrophilic head groups. On top of this mixed SAM, lipid vesicles were spread to create a tBLM.¹⁰

3.3 Electrostatics at the Electrode Interfaces

*Parts of this section were published in Staffa, J. K. et al. Determination of the Local Electric Field at Au/SAM Interfaces Using the Vibrational Stark Effect. J. Phys. Chem. C **121**, 22274–22285 (2017).^{21,54} Copyright 2017 American Chemical Society.*

To quantify the electric field at biomimetic interfaces the electrostatics at the electrodes must be considered and understood. Coating an electrode with a SAM leads to an electrostatic model for the electrode/SAM/solution interface which was first described by Smith and White and later refined by Murgida and Hildebrandt.^{55,56}

Electrode/solution interface If a metal gets in contact with an electrolyte solution a charged interface is created (**Figure 11 A**). The metal charges and charges in solution will be redistributed and two layers of different polarities arise. Depending on the metal its electron density will be increased or reduced. The corresponding ions with opposite charge to the metal will create an ordered and compact layer on the metal resulting in a potential drop. This layer is known as inner Helmholtz plane (IHP) or Stern layer. It is about 1 nm thick and the gain of free energy for the formation compensates the partial loss of the hydration shell. Solvated ions are attracted by the charge of the IHP and diffuse freely. However, they are influenced by a concentration gradient defined by the interfacial electric field. This second layer is called outer Helmholtz plane (OHP) or diffuse layer. The charge distribution of the electric double layer is based on a concept by Helmholtz and Gouy-Chapman and can be described by an electrostatic model. According to Smith and White the charge densities (σ_i with $i = M, C, S$ for metal, IHP or SAM and solution, respectively) at each interface must be considered to describe the charge distribution. For the estimation of the charge density of the metal, Gauss' law is applied by using the potential difference between the metal (ϕ_M) and IHP (ϕ_C)

$$\sigma_M = \frac{\epsilon_0 \epsilon_C}{d_C} (\phi_M - \phi_C). \quad (2.51)$$

In this equation ϵ_0 is the permittivity, ϵ_C and d_C the dielectric constant and distance of the IHP, respectively. The decay of the charge density from the IHP to a potential at an infinite distance

to the electrode in solution is influenced by the potential difference of the IHP and the solution ϕ_S :

$$\sigma_S = -\varepsilon_0 \varepsilon_S \kappa \left(\frac{2kT}{ze} \right) \sinh \left(\frac{ze}{2kT} \right) (\phi_C - \phi_S). \quad (2.52)$$

Here, ε_S is the dielectric constant of the solution, z is the number of electrons and e the elementary charge. k is the Boltzmann constant and T the temperature. The Debye length κ defines the thickness of the OHP by an exponential decay of the potential to e^{-1} of its initial value and depends on the ionic strength I of the solution:

$$\kappa = \sqrt{\frac{\varepsilon_0 \varepsilon_S k T}{I}}. \quad (2.53)$$

At last the charge density of the IHP σ_C can be calculated on the basis of the charge neutrality of the complete system:

$$\sigma_M + \sigma_C + \sigma_S = 0. \quad (2.54)$$

When applying an external potential to the electrode, the potential of the metal ϕ_M changes. The absolute charge density on the metal surface and the effecting electric field perturbation in solution becomes zero when the potential of zero charge (E_{PZC}) is reached, which is a particularly interesting state.

$$E - E_{PZC} = \phi_M - \phi_S \quad (2.55)$$

Electrode/SAM/solution interface By covering the metal with an amphiphilic SAM a hydrophobic layer is created with a dielectric constant of 2-3 (Figure 11 B).⁵⁵ The potential drops linear over the SAM. The IHP is located at the counter layer of ions at the head groups and the OHP is nearby in solution. The charge density of the metal changes because of the SAM and follows the same behaviour like in equation (2.51) whereas ε_C , d_C and ϕ_C are the dielectric constant, distance and potential of the SAM, respectively. Equations (2.51) to (2.55) account in the same way for the metal/SAM/solution interface with exception that all parameters with the index c refer to the SAM.

The potential of zero charge E_{PZC} of the bare metal is related with the effective potential of zero charge ($E_{PZC,eff}$) of the SAM-coated metal according to

$$E_{PZC,eff} = E_{PZC} + \Delta\phi_{SAM}. \quad (2.56)$$

2. Theoretical Background

Often SAMs have a charged head group and therefore the dielectrics of the alkyl chain and head group differ. In a simple model this classification is not considered, and one layer is assumed with a linear potential drop. The model proposed by Smith and White, was later refined by Murgida and Hildebrandt, Schkolnik et al. and Staffa et al. by taking into account the properties of the SAM alkyl chain and head group (**Figure 11 C**).^{21,55-57} Thus, the potential drop over a SAM is described more accurately.

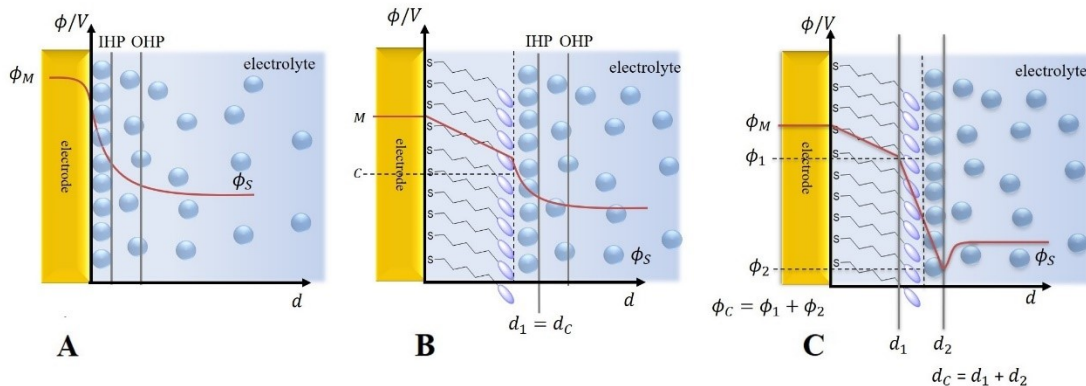


Figure 11: Potential distribution and formation of electrostatic double layers at a metal electrode in solution (**A**), a metal electrode covered by an alkanethiol SAM (**B**) and a metal electrode covered by an alkanethiol SAM with a separated hydrocarbon and head group region (**C**).

The quantity σ_C (Cm^{-2}) at the distance d_C (distance of the charges at the head groups to the electrode) refers to the charge density on the SAM surface. For carboxyl-terminated SAMs, σ_C has been related to apparent pK_a values.⁵⁶ Whereas for polar head groups like nitriles, σ_C includes the partial charges of ions and water dipoles aligned in the head group region. The partial charges of the CN head groups represent the IHP and thus the charge density at the electrode can be described as

$$\sigma_M = \frac{\epsilon_0 \epsilon_1 \epsilon_2}{d_1 \epsilon_2 + d_2 \epsilon_1} (\phi_M - \phi_C). \quad (2.57)$$

Here, ϵ_1 , ϵ_2 and d_1 , d_2 refer to the dielectric constants and distances of the head group (1) and acetyl chain (2) of the SAM. ϕ_C is the potential of the SAM at $d_1 + d_2 = d_C$. The potential drops linear at the acetyl chain and then exhibits a sharp potential drop generated by the charged head groups followed by an exponential decay according to the Gouy-chapman theory abovementioned. The charge density in solution described in equation (2.52) can then be simplified to

$$\sigma_S = -\epsilon_0 \epsilon_S \kappa \left(\frac{2kT}{ze} \right) \sinh \left(\frac{ze}{2kT} \right) (\phi_C - \phi_S) \approx -\epsilon_0 \epsilon_S \kappa (\phi_C - \phi_S). \quad (2.58)$$

Using equations (2.57), (2.58), (2.54) and (2.55) an expression for the electric field strength between d_1 and d_c ($E_F = \frac{\epsilon_1}{d_1 \epsilon_2 + d_2 \epsilon_1} (\phi_M - \phi_C)$) can be obtained of

$$E_F = \frac{\varepsilon_0 \varepsilon_S \kappa}{\varepsilon_0 \left[\frac{\varepsilon_1 \varepsilon_2 \cdot (d_1 + d_2)}{d_1 \varepsilon_2 + d_2 \varepsilon_1} + \varepsilon_S \kappa (d_1 + d_2) \right]} (E - E_{PZC}) - \frac{\sigma_C}{\varepsilon_0 \left[\frac{\varepsilon_1 \varepsilon_2 \cdot (d_1 + d_2)}{d_1 \varepsilon_2 + d_2 \varepsilon_1} + \varepsilon_S \kappa (d_1 + d_2) \right]} \quad (2.59)$$

Showing the analogous behaviour to the more simplified model described above, layer 2 can be removed from this equation by setting $d_2 = 0$; and the simpler equation describes a capacitor including only one dielectric medium. For the potential-dependence of the charge density at the SAM σ_C in a first approximation a linear relationship with respect to $(E - E_{PZC,eff})$ is assumed (by substitution of E_{PZC} with $E_{PZC,eff}$ for SAM coated electrodes)⁵⁶

$$\sigma_C = \sigma_0 + k(E - E_{PZC,eff}) \quad (2.60)$$

with k as a constant and σ_0 the charge density at the potential of zero charge. Combining equation (2.56) and (2.60) with (2.59) leads to

$$E_F = \frac{\varepsilon_0 \varepsilon_S \kappa - k}{\varepsilon_0 \left[\frac{\varepsilon_1 \varepsilon_2 \cdot (d_1 + d_2)}{d_1 \varepsilon_2 + d_2 \varepsilon_1} + \varepsilon_S \kappa (d_1 + d_2) \right]} (E - E_{PZC,eff}) - \frac{\sigma_0 - \varepsilon_0 \varepsilon_S \kappa \Delta \phi_{SAM}}{\varepsilon_0 \left[\frac{\varepsilon_1 \varepsilon_2 \cdot (d_1 + d_2)}{d_1 \varepsilon_2 + d_2 \varepsilon_1} + \varepsilon_S \kappa (d_1 + d_2) \right]}. \quad (2.61)$$

Thus, the electric field is zero, when $E = E_{PZC,eff}$, which implies

$$\sigma_0 = \varepsilon_0 \varepsilon_S \kappa \Delta \phi_{SAM}. \quad (2.62)$$

Equation (2.61) can then be simplified to

$$E_F = \frac{\varepsilon_0 \varepsilon_S \kappa - k}{\varepsilon_0 \left[\frac{\varepsilon_1 \varepsilon_2 \cdot (d_1 + d_2)}{d_1 \varepsilon_2 + d_2 \varepsilon_1} + \varepsilon_S \kappa (d_1 + d_2) \right]} (E - E_{PZC,eff}). \quad (2.63)$$

E_F is a scalar that varies its sign depending on $(E - E_{PZC,eff})$, which is acceptable to describe the interfacial electric field that is parallel or antiparallel to the surface normal. If $E > E_{PZC,eff}$ the electric field E_F is positive whereas its negative for $E < E_{PZC,eff}$.

Electrode/tBLM/solution A more complicated model is required when building a tBLM on the electrode as it was done in this work. The adaptation of the electrostatic model mentioned before is not trivial, since the profile of the potential is a combination of the metal/SAM/solution interface and a phospholipid membrane. First it must be considered that a mixed SAM is adsorbed on the electrode. Based on the phase separation of the two different SAM's there are two IHPs and two OHPs.²⁶ Since the phospholipid membrane is built on top of

2. Theoretical Background

the mixed SAM the hydrophobic head group of the long SAM directly interacts with the hydrophobic alkyl chains of the lipids. We assume that in this area no changes of the electrostatics occur and the potential drops linearly from the SAM head group to the lipid head group like in the inside of a phospholipid membrane (d_4 to d_5). Furthermore, a small water reservoir of a few nm is created in between the short SAM and lipid head groups. As a second assumption we consider the potential drop in the reservoir as linear. (d_2 to d_3) At the edges of the reservoir double layers are formed with the SAM head groups (d_2) and lipid head groups (d_3). These double layers can be treated like the one described in the electrode/SAM/solution interface part. Summarizing, the potential drops are linear inside the SAM alkyl chains, the water reservoir and the lipid double layer. Additionally, three double layers are created at the SAM/water interface (d_2), the water/lipid interface (d_3) and lipid/water interface (d_6) interface. The double layers are nearby so they should sense each other. A schematically description of the potential curve is shown in **Figure 12**.

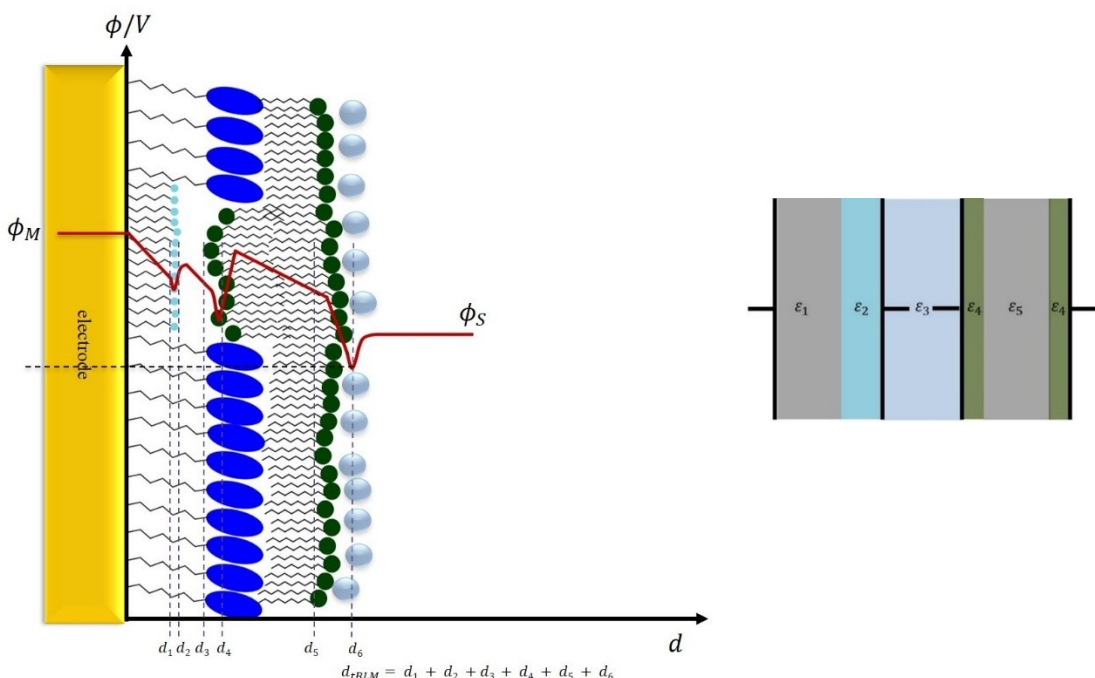


Figure 12: Schematic representation of the potential profile over a tBLM system structured on an Au-Electrode with the distances of the single units of the electrostatic model. (left) As well as an analogous capacitor with five different dielectric constants representing the alkyl chain (ε_1), the head group with the first layer of charges of the short SAM (ε_2), the water reservoir (ε_3), the lipid head groups with the first layer of charges (ε_4) and the lipid alkyl chains (ε_5). (right)

In analogy to the treatment in the previous section the charge density of the metal changes according to:

$$\sigma_M = \frac{\varepsilon_0 \sum_{\substack{i=1, \dots, 5 \\ j=1, \dots, 6}} \varepsilon_i}{\sum_{\substack{i=1, \dots, 5 \\ j=1, \dots, 6}} \varepsilon_i d_j} (\phi_M - \phi_C) \quad (2.64)$$

with $i \neq j$. The amount of the dielectrics is weighted with their distance from the electrode (d_j).

This equation holds under the same conditions like for the electrode/SAM/solution interface. For the effective potential of zero charge now the contribution of the tBLM must be considered ($\phi_C = \phi_{tBLM}$):

$$E_{PZC,eff} = E_{PZC} + \Delta\phi_{tBLM}. \quad (2.65)$$

In the case of uncharged lipids, the surface potentials are deleted and the potential drops at the water/lipid and lipid/water interface with κ . The double layers at d_3 and d_6 have been omitted.

4. Models to Quantify the Electric Field

Quantifying electric fields in biological systems is experimentally still a challenge. At the interface of lipid membranes electric potentials around 220 mV – 280 mV correspond to very large electric fields (10^8 - 10^9 V/m) in this region.⁵² These local electric fields influence the activity and conformation of membrane proteins like potential dependent ion channels. It is known that the local electric field strength regulates the conformational state of ion channels.⁵⁸

It is of great interest to quantify electric fields at biological processes and provide an insight into their effect on the mechanism. Indeed, in-situ quantifications are still a challenge. With voltage sensitive dyes and fluoresce spectroscopy it is possible to determine the dipole potential at the head group region of phospholipid membranes by incorporating the dyes into lipid vesicle membranes.⁵¹ Another promising tool to calculate electric fields is the vibrational Stark effect (VSE). Here, small reporter groups, like cyanide or carbonyl, exhibit localised stretching modes whose frequencies respond very sensitively to changes of the electric field. Thus, the local electric field can be determined by the shift of the vibrational frequency compared to the frequency at zero-field. Boxer and co-workers used the VSE to study the enzymatic reaction of ketosteroid isomerase, an enzyme with the highest known unimolecular rate constant in biochemistry and found out that an extremely large electric field occurs during a charge rearrangement in the rate-determining step.⁵⁹ In this work the VSE is applied to quantify interfacial electric fields and determine the transmembrane potential of biomimetic interfaces.

4.1 The Vibrational Stark-effect

In 1913 Johannes Stark and Anthony Lo Surdo simultaneously discovered the splitting of the spectral lines of hydrogen in presence of an external electric field.⁶⁰ Hence the vibrational Stark effect (VSE) was developed and describes the change in the vibrational transition frequency of a molecule by an external electric field applied to the system (**Figure 13 A, B**):

$$\nu = \nu_0 - \left(\Delta\vec{\mu}\vec{E}_F + \frac{1}{2}\vec{E}_F\Delta\alpha\vec{E}_F \right). \quad (2.66)$$

Here $\Delta\vec{\mu}$ is the difference dipole moment (between the ground and excited vibrational states), $\Delta\alpha$ is the difference polarizability and ν_0 the frequency in the absence of an external electric field \vec{E}_F . For electric field strengths below 10^{10} V/m, the quadratic term can be neglected, and then the frequency has a linear relationship to the electric field with⁶¹

$$\nu \cong \nu_0 - |\Delta\vec{\mu}| |\vec{E}_F| \cos\theta, \quad (2.67)$$

where θ is the tilt angle between the vectors of the difference dipole moment and the electric field. Strong electric fields occur at the solvation of charges or dipolar molecules, in biological systems or at electrode surfaces. If the relationship between the frequency of a vibration and the electric field is established, suitable reporter groups can be incorporated in the molecular region of interest, for instance proteins, to determine the local electric field on the basis of the respective frequency shifts.

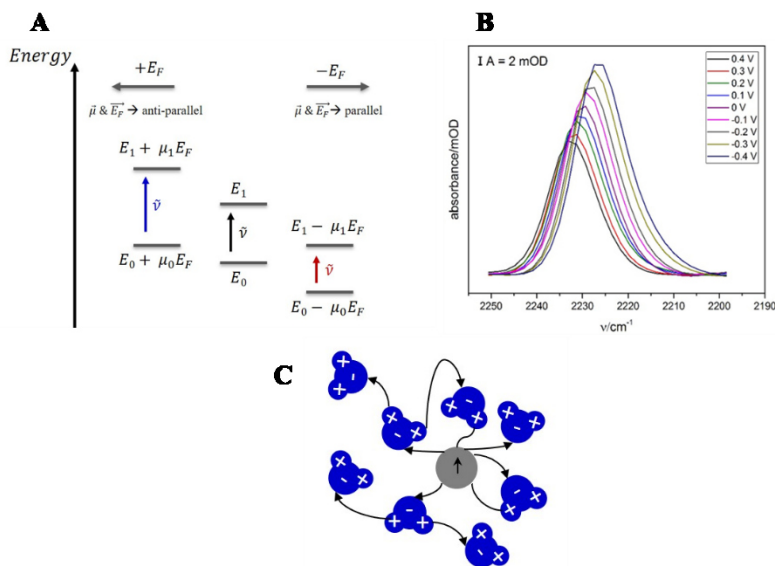


Figure 13: Description of the vibrational Stark effect with the ground (E_0) and excited (E_1) vibrational state and the shift by an interaction with an electric field (E_F) to the red (smaller energy gap) and to the blue (bigger energy gap) depending on the alignment of the dipole moment vector of the vibration and the electric field vector. **(A)** The shift in frequency and intensity of an absorbance band by applying different potentials. **(B)** Illustration of non-covalent interactions of a dipole surrounded by an electric field of the solvent. **(C)**

With the scalar product of $|\Delta\vec{\mu}|$ and $|\vec{E}_F|$ in **equation (2.67)** the energetic effect of the electric field on a vibrational transition is expressed. The energy is reduced for $\nu < \nu_0$ (red-shift), when the tilt angle is $\theta < 90^\circ$, so the projection of $|\Delta\vec{\mu}|$ and $|\vec{E}_F|$ is parallel to \vec{E}_F . In that case $-|\Delta\vec{\mu}||\vec{E}_F|cos\theta$ is negative. For the case of $\theta > 90^\circ$ the term gets positive for an increase in energy $\nu > \nu_0$ (blue-shift) and the projection of $|\Delta\vec{\mu}|$ and $|\vec{E}_F|$ will be anti-parallel. (**Figure 13 A**)

The Stark-tuning rate: The difference dipole moment, expressed in $\frac{cm^{-1}}{MV/cm}$, illustrates the sensitivity of the vibrational frequency to an external electric field, therefore called Stark tuning rate. Applying an electric field of $1\text{ MV}/cm$ along the vibrational axis affords a vibrational shift of 1 cm^{-1} . By analysing biological systems, the Boxer group and co-workers determined many Stark tuning rates for Stark reporter groups (**Table 3**). They provided the values with the frozen glass method, whereas the sample was dissolved in an organic solvent and spectra were measured with FTIR spectroscopy in a sandwich cell. These spectra display the difference between ‘field-on’, by applying an external electric field, and ‘field-off’.

Table 3: Collection of Stark-tuning rates for different Stark reporter groups in different molecules. In some of the literature the Stark tuning rate were declared with a dependence on the local electric field factor as $|\Delta\vec{\mu}|f$, for these values f was assumed to be $f = 2$ (see section above).

Molecule	Reporter group	Stark tuning rate / $\frac{cm^{-1}}{MV/cm}$	Molecule	Reporter group	Stark tuning rate / $\frac{cm^{-1}}{MV/cm}$
CO free	$-\text{C}\equiv\text{O}$	0.34 ^c	acetonitrile	$-\text{CN}$	0.34 ^d
4-fluorobenzenethiol	$-\text{CF}$	0.45 ^b	benzonitrile	$-\text{CN}$	0.38 ^b
fluorobenzene	$-\text{CF}$	0.42 ^b	4-mercaptopbenzonitrile	$-\text{CN}$	0.42 ^e
2-ABN	$-\text{CN}$	0.4 ^a	p-DCB (dicyanobenzene)	$-\text{CN}$	0.4 ^a
3-ABN	$-\text{CN}$	0.32 ^a	azidotrimethylsilane	$-\text{N}_3$	0.32 ^a
3-cyanopyridine	$-\text{CN}$	0.28 ^b	p-toluidine	$-\text{NH}_2$	0.28 ^b
4-Aminobenzonitrile (4-ABN)	$-\text{CN}$	0.6 ^a	acetone	$-\text{OH}$	0.6 ^a
4-cyanopyridine	$-\text{CN}$	0.3 ^b	methyl thiocyanate	$-\text{SCN}$	0.3 ^b
5-cyanoindole	$-\text{CN}$	0.43 ^b			

Data taken from ^aLevinson, Fried and Boxer³³ ^bSuydam and Boxer⁶² ^cPark and Boxer⁶³ ^dFried, Bagchi and Boxer⁶⁴ ^eSchkolnik⁵⁷

2. Theoretical Background

Local field effect It was observed that the Stark tuning rate measured with solvatochromic measurements is 2-fold lower than the value determined with Stark spectroscopy with the frozen glass method. The local field effect significantly influences the Stark tuning rate due to the applied potential when performing Stark spectroscopy. For the empty parallel plate capacitor, the electric field depends on the ratio of the applied voltage and the distance between the plates. By adding a dielectric material, this relationship is still applicable in a macroscopic view but microscopically the local electric field created by the applied potential differs from U/d because of the heterogeneous charge distribution. This effect is induced by charges accumulated at the capacitor plates. It also occurs when applying electric fields on molecules immobilized on an electrode. Thus, the local electric field $\vec{E}_{F,loc}$ differ in direction and magnitude of the applied field $\vec{E}_{F,ext}$, which can be indicated by the tensor f .⁵⁹

$$\vec{E}_{F,loc} = f \vec{E}_{F,ext}. \quad (2.68)$$

The magnitude of f is not known experimentally but can be proposed with theoretical calculations using continuum dielectrics, it is estimated to be 1.5 – 2.5 but the complete understanding is still subject of ongoing research.^{61,65} Accordingly, with Stark spectroscopy the effective Stark tuning rate modified by f is determined

$$|\Delta\vec{\mu}|_{eff} = |\Delta\vec{\mu}|f. \quad (2.69)$$

Noncovalent interactions Noncovalent interactions are important for self-organization or to develop complex structures like in biological systems, such as protein folding, enzyme catalysis or receptor-ligand interactions. The most important noncovalent interactions in nature are electrostatic and therefore explanations with orbitals and electron densities are not suggestive. The electric field applies to specific and non-specific interactions, quantitatively and microscopically, thus is a good way to describe noncovalent interactions. The interaction between a molecule and its surroundings with noncovalent character can be treated as the interaction of a dipole in an electric field. (Figure 13) Noncovalent interactions create electric fields in a range between dipole-induced dipole interactions ($< 10 \text{ MV/cm}$) and strong H-bonds ($70\text{-}100 \text{ MV/cm}$). Solvation forces with nonpolar solvents are limited to induced dipole interactions, with polar solvents also permanent dipoles can occur and create larger electric fields. Specific noncovalent interaction like H-bonding or halogen-bonds include one specific molecule in the environment and a specific geometry between the solute and solvent is necessary. H-bonds exert large electric fields in comparison to dipole-dipole interactions because hydrogen is the smallest atom. When it generates a dipole with another atom, the hydrogen bond distance can be strongly reduced. Therefore, water with a high density of H-bonds forms multiple H-bonds simultaneously and has a high solvent field.⁶¹

VSE in biological systems Biological systems are highly organized and the environment of active sites or binding pockets are structurally and electrostatically optimized for the specific function of the biomolecule. For the determination of local electric fields at these sites, one may incorporate labelled amino acids including VSE reporter groups via genetic engineering or chemical syntheses. Inserting p-acetyl-phenylalanine in the hydrophobic core of ribonuclease S

the CO-reporter group leads to an electric field of -19 MV/cm .⁶⁴ Ketosteroid isomerase undergoes a charge rearrangement in the reaction mechanism and the local electric field at the CO-bond of 19-nortestosterone was found to be -140 MV/cm .⁵⁹ Also the nitrile group can be used in this respect, for instance, via incorporating CN-phenylalanine or CN-alanine. The nitrile stretching is a commonly used Stark reporter group in biological systems, because its vibration is in a region where no other fundamental vibrations of biomolecules occur. It is thus easy to detect and shows narrow and intense bands. However, the shift of the nitrile vibration is highly influenced by hydrogen bonds and noncovalent interaction.^{57,61,66–68}

4.2 The Onsager Model to Calculate Solvent Reaction Fields

The vibrational frequency of a VSE reporter group is influenced by the solvent polarity, such that its Stark tuning rate can be determined by solvatochromic measurements. The solvent reaction field can be identified with the total electric field the reporter group is exposed to.⁶⁹ The Onsager reaction field theory is a common model to calculate the solvent reaction field. The solute occupies a spherical cavity with a radius a inside a continuum dielectric medium:

$$\frac{4}{3}\pi * a^3 * N_T = 1. \quad (2.70)$$

Here N_T represents the number of molecules per volume, which can be calculated with the Avogadro constant N_a and the ratio of the density ρ and molecular mass M of the solute:

$$N_T = \frac{\rho}{M} N_a. \quad (2.71)$$

The solvent reaction field $\vec{R}_{F,solv}$ in CGS-units is given as:

$$\vec{R}_{F,solv} = \frac{1}{a^3} \frac{2(\varepsilon - 1)}{2\varepsilon + 1} \mu = f\mu. \quad (2.72)$$

The dielectric constant of the solvent is ε and the dipole moment of the solute μ . Because the reaction field induced a dipole ($\alpha\vec{R}_{F,solv}$) **equation (2.72)** must be extended to

$$\vec{R}_{F,solv} = f(\mu + \alpha\vec{R}_{F,solv}) = \frac{f}{1-f\alpha}\mu. \quad (2.73)$$

Combining **equation (2.72)** and **(2.73)** leads to:

$$\vec{R}_{F,solv} = \frac{1}{\frac{2(\varepsilon - 1)}{2\varepsilon + 1} - \frac{a}{a^3}} \frac{1}{a^3} \mu. \quad (2.74)$$

2. Theoretical Background

The ratio between the radius a and the volume a^3 can be substituted with the use of the refractive index n to

$$\frac{a}{a^3} = \frac{n^2 - 1}{n^2 + 2}. \quad (2.75)$$

This leads to a description of the reaction field with

$$\vec{R}_{F,solv} = \frac{2(\varepsilon - 1)}{2\varepsilon + n^2} \frac{n^2 + 2}{3} \frac{1}{a^3} \mu. \quad (2.76)$$

Substituting the volume of the solute by **equations (2.70) and (2.71)** the reaction field in CGS-units is given by

$$\vec{R}_{F,solv} = \frac{2(\varepsilon - 1)}{2\varepsilon + n^2} \frac{n^2 + 2}{3} \frac{4}{3} \pi \mu \frac{\rho}{M} N_a. \quad (2.77)$$

Transferring this equation into SI-units, this equation must be multiplied by $1/4\pi\varepsilon_0$

$$\vec{R}_{F,solv} = \frac{\mu}{3\varepsilon_0} \frac{\rho}{M} N_a \frac{2(\varepsilon - 1)}{2\varepsilon + n^2} \frac{n^2 + 2}{3}. \quad (2.78)$$

Solvatochromic shifts depend linearly on the solute's dipole moment. More polar solvents create larger dipoles and thus larger solvent reaction fields. The sensitivity of the reporter group vibration to solvent variations ($\Delta\nu_{solv}$) is directly proportional to the difference dipole of the molecule

$$\Delta\nu_{solv} \propto |\Delta\vec{\mu}|. \quad (2.79)$$

For example, the difference dipole of CO is twice than that of CN and the band shifts in solvatochromic measurements twice as much.⁶¹ Since the CN vibration is highly influenced by hydrogen bonds, deviations from the linear behaviour are found for protic solvents. Hydrogen bonding preferentially occurs via the lone pair of the nitrile nitrogen and leads to a shift of the charge density to the hydrogen donor. Since the electron density is reduced the bond becomes stronger and the vibration shifts to higher frequencies. This effect can be more pronounced than the downshift of the frequency caused of the electrostatic field. For the halogen-interaction the halogen σ -hole is the electron acceptor for the lone-pair of the CN and a shift of the electron density leads to a shift to higher frequencies.

5. Theoretical Methods

In this work density functional theory (DFT) calculations were carried out to support the interpretation of the experimental data. DFT calculations can predict chemical and physical properties of molecules. This method is used to solve the electronic Schrödinger equation for many-body systems. Here, the entire system of N electrons is presented by an electron density distribution. The electron density of the ground state is changed during the calculation until an energy minimum is achieved by the help of calculations of auxiliary orbitals. A problem in DFT calculations are the exchange-correlation term because the exact form of the correlation of a system of interacting electrons is unknown. Thus, hybrid functions are used, which combine DFT with Hartree-Fock calculations by the use of the exchange integral. The Becke-Three-Parameter Hybrid Functional (B3LYP), based on functionals from Becke in 1993, was used in this thesis and can be described as:⁷⁰

$$A E_X^{Slater} + (1 - A)E_X^{HF} + B + \Delta E_X^{Becke} + E_C^{VWN} + C \Delta E_C^{non-local} . \quad (2.80)$$

Here A, B and C are constants determined by Becke. E^{Slater} describes the Slater functionals, E^{HF} the Hartree-Fock functional, E^{Becke} the Becke functional, E^{VWN} the Vsoko, Wilk and Nusair correlation functional and $E^{non-local}$ the non-local functional.³⁸

Within this work, frequencies of molecules with a Stark reporter group were calculated in different solvents. Therefore, the SCRF model of Gaussian was used. Like the Onsager model, calculations are performed by placing the solute in a cavity within the solvent reaction field. The solvent reaction field was described by its dielectric constant.

3. Material and Methods

1. Chemicals and Biomolecules

Table 4: All chemicals listed and used in this work were of highest purity.

Chemical	provider	Chemical	provider
1-propanol	merck	hydrofluoric acid	sigma aldrich
2-methylbutane	sigma aldrich	potassium dihydrogen phosphate	merck
3-methoxypropionitrile	sigma aldrich	4-mercaptopbenzonitrile (MBN)	sigma aldrich
3-sulfanylpropanenitrile	otava	methanol	sigma aldrich
5-Azidopentanoic acid	sigma aldrich	methyl thiocyanate	sigma aldrich
5-Azidopentanoic acid (COOHC ₅ N ₃)	sigma aldrich	n-heptane	sigma aldrich
6- bromo-hexanitrile	sigma aldrich	n-hexane	merck
6-mercaptophexanol (6MH)		n-mercaptopbutylnitrile	sigma aldrich
7-bromo-heptanitrile	sigma aldrich	POPC	avanti lipids
7-bromo-heptanitrile	sigma aldrich	POPG	avanti lipids
acetone	merck	propylene carbonate	sigma aldrich
acetonitrile	merck	propylene carbonate	sigma aldrich
ammonium fluoride	sigma aldrich	silver nitrate	merck
bis trispropane	sigma aldrich	sodium aurumchloird	sigma aldrich
borhydride, polymer supported	sigma aldrich	sodiumchlorid	merck
borohydride	sigma aldrich	sodiumsulfit	merck
Cholesterol	avanti lipids	sodium thiosulfate	sigma aldrich
cyclohexane	sigma aldrich	sulphur powder	sigma aldrich
cyclohexane carbonitrile (CHCN)	sigma aldrich	sulfuric acid	sigma aldrich
dichloromethane	sigma aldrich	tetrachloromethane	sigma aldrich

di-potassiumhydrogenphosphate	merck	tetrahydrofuran	sigma aldrich
dimethyl sulfoxide	sigma aldrich	toluol	sigma aldrich
ethanol	sigma aldrich	WK3SH	synthesized by S. Wielback & J. Kozuch ¹⁰
hydrochloric acid	merck		

If not mentioned otherwise, buffer solution containing 20 mM BTP and 150 mM NaCl adjusted to pH 7.4 were employed. In this whole work millipore water was used.

As lipids with Stark reporter groups 7-beta-thiocyanocholeste-5-en-3-betyl acetate (CL-SCN) from Sigma-Aldrich and 1,2-dipalmitoyl-sn-glycero-3-phosphoethanolamine-N-(6-azido-hexanoyl) (ammonium salt) (PE-N₃) from Avanti Polar Lipids were used. (**Figure 14 A, B**)

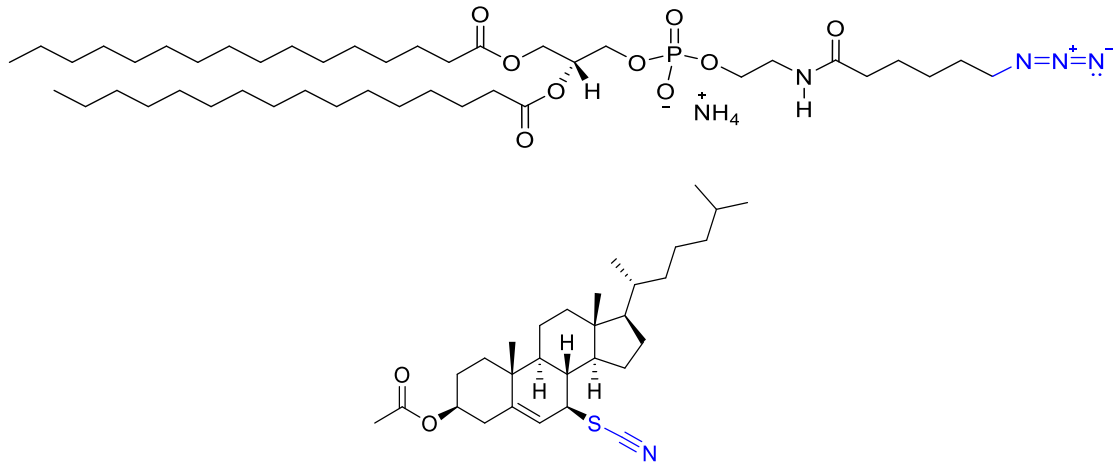


Figure 14: Chemical structure of the used lipids 1,2-dipalmitoyl-sn-glycero-3-phosphoethanolamine-N-(6-azidohexanoyl) (ammonium salt) (**A**) and 7-beta-thiocyanocholeste-5-en-3-betyl acetate (**B**).

1.1 Synthesis of Di-alkyl-nitriles-disulphides

Like it was already described in my master thesis and in Staffa et al. 2017 di(6-hexanenitrile)-disulphide and di(7-heptanenitrile)-disulphide were synthesized according to the synthesis done by Lisa Lorenz in 2004.^{21,54,71}

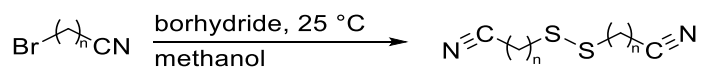


Figure 15: Chemical equation for the synthesis of di-alkyl-nitriles-disulphides.

¹H – NMR and ¹³C – NMR were measured with the Bruker Advance 400 MHz NMR spectrometer. As solvent, deuterated dimethyl sulfoxide was used. The chemical shifts are

3. Material and Methods

presented in ppm. The LCMS measurements were done in the Süssmuth Group at the TU Berlin. The validated LCMS system consisted of two HPLC pumps (PU-980, Jasco, Gro-Umstadt, Germany), one binary pump (G1312A, Agilent, Walbronn, Germany), coupled to a 2000QTrap mass spectrometer (AB Sciex, Foster City, CA, USA) and was run with column switching technology and a throughput of 1 min/sample.⁷² As a solvent for the HPLC acetonitrile was used.

For the synthesis of the disulphides borohydride (1 g, 5 mmol, 1 eq) was stirred with sulphur powder (0.16 g, 5 mmol, 1 eq) in 3 mL methanol for ten minutes at room temperature. Then 6-bromo-hexanitrile (0.88 g, 5 mmol, 1 eq) or 7-bromoheptanitrile (0.95 g, 5 mmol, 1 eq) was added and the solution was stirred for further 10 minutes. The resin was filtered, and methanol was removed under reduced pressure. The resulting oil was purified by column chromatography on silica gel and the di(6-hexanenitrile)-disulphide (9 mg, 1 %) and di(7-heptanenitrile)-disulphide (14 mg, 1.5 %) was obtained, respectively. The product was analysed with ¹H-NMR, ¹³C-NMR and MS and the results are shown in **Table 5**

Table 5. Analysis data for di(6-hexanenitrile)-disulphide and di(7-heptanenitrile)-disulphide.

Analysis of di(6-hexanenitrile)-disulphide:

¹H-NMR (200MHz, DMSO): δ(ppm) = 3.3 (H₂O) 2.73 (t, 4H, CH₂-S), 2.5 (t, 4H, CH₂-CN) 1.66 (qi, 4H), 1.56 (qi, 4H), 1.45 (qi, 4H)

¹³C-NMR (200MHz, DMSO): δ(ppm) = 121.11 (C-6), 37.92 (C-1), 28.20(C-2), 27.32(C-3), 24.82(C-4), 16.54 (C-5)

MS: m/z (%) = 257 [M+H]⁺; 279 [M+Na]⁺

Analysis of di(7-heptanenitrile)-disulphide:

¹H-NMR (200MHz, DMSO): δ(ppm) = 3.3 (H₂O) 2.73 (t, 4H, CH₂-S), 2.5 (t, 4H, CH₂-CN) 1.64 (qi, 4H), 1.55 (qi, 4H), 1.38 (septet, 4H)

¹³C-NMR (200MHz, DMSO): δ(ppm) = 121.15 (C-7), 38.13 (C-1), 28.74(C- 2), 28.10(C-3), 27.37(C-4), 25.08 (C-5), 16.56 (C-6)

These disulphides dissociate in thiolates, correspond to the thiol species 6-mercaptophexanenitrile (C₅CN) and 7-mercaptopheptanenitrile (C₆CN), upon self-assembly on the Au surface due to the formation of Au-S bonds.

2. Instrumentation

2.1 IR Spectrometer

IR spectra (SEIRA, ATR or transmission) were measured either with a Bruker IFS66v/s FTIR-spectrometer or TENSOR 27. For SEIRA and ATR an ATR set-up in the Kretschmann configuration with an incidence angle of 60° was used. Both spectrometers are equipped with a liquid-nitrogen-cooled photovoltaic mercury-cadmium-telluride (MCT) detector and a globar® as the IR source. The interferometer of the Tensor 27 is a ROCKSOLID™ and in the IFS66v/s a Michelson interferometer is implemented. Interferometer, globar® and detector are under vacuum and the sample chamber was carefully purged with nitrogen gas in the case if the IFS66v/s. For the TENSOR 27 the devices were purged with dry air. Using the SEIRA and ATR technique, a trapezoidal prism (LxWxH = 25 mm x 20 mm x 10 mm) served as IRE.

2.1.1 Cells for IR Measurements

SEIRA and ATR-IR Spectroscopy Performing SEIRA and ATR measurements a homemade spectro-electrochemical cell, depicted in **Figure 16** was used. Basically, the glass cell consists of two parts: (1) the spectroscopic part at the bottom with the IRE and (2) the electrochemical part on the top with the buffer solution and a three-electrode system. For electrochemical applications a Pt-wire as a counter electrode (CE) and an Ag/AgCl (3 M KCl) reference electrode (RE) were placed in the solution. The gold film, created by electroless gold deposition, serves as working electrode (WE). For IR measurements, spectra were recorded in a spectral region between 4000 and 800 cm⁻¹ with a spectral resolution of 4 cm⁻¹. About 400 scans were accumulated for one spectrum in 3 minutes.

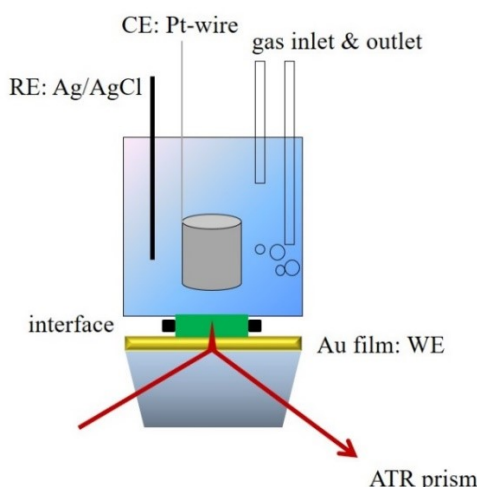


Figure 16: The homemade spectro-electrochemical cell for SEIRA and ATR-IR measurements. On the bottom is an ATR prism with an electroless deposited Au-film. On top is a vessel with a 3-electrode system (Pt-wire as counter electrode, Ag/AgCl reference electrode and Au-film as working electrode).

BioATR-IR Spectroscopy For measurements of vesicles in solution the Harrick BioATR cell™ sampling accessory was applied with an IRE element of Si/ZnSe and an isolated compartment, enclosing the optical path. The sample volumes for the IRE comprised 20 µL. For each sample

3. Material and Methods

and background measurement 400 scans were accumulated with a spectral resolution of 4 cm^{-1} and an aperture of 2.5 mm. The measurement was controlled by the Bruker OPUS 5.5 software.

IR-Transmission Spectroscopy For transmission measurements a sandwich cell shown in **Figure 15** was used and spectra were detected with 200 scans, a spectral resolution of 2 cm^{-1} and an aperture of 2.5 mm. The measurement was controlled by the Bruker OPUS 5.5 software. Background measurements were done for at least 2 h and for the sample a concentration of 4 mM and a volume of 8 μL was employed.

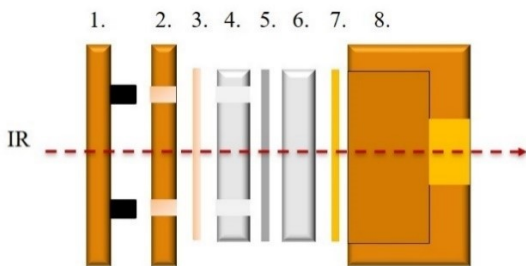


Figure 17: The transmission cell consists of 1. Upper cap, 2. lower cap with filling notches, 3. septum, 4. upper CaF_2 window with filling wholes, 5. teflon spacer, 6. lower CaF_2 window, 7. aperture and 8. brass body.

2.2 Electrochemistry and EIS

Electrochemical treatments were conducted using a $\mu\text{AutolabIII/FRA2}$ or a BIGautolab/FRA32M. For potential-dependent SEIRA measurements a static potential was applied with the Nova 2.1 software or the GPES software, for electrochemical impedance spectroscopy the Nova 2.1 software or FRA software was used. Impedance spectra were monitored in a frequency range of 0.1 to 100 kHz using a static potential of 0.25 V and an amplitude of 25 mV (rms value), also potential-dependent impedance spectra were recorded in the same frequency range.

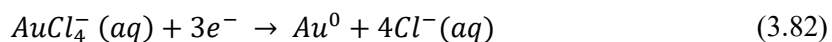
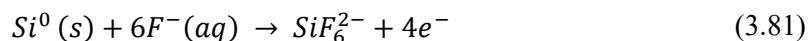
3. Procedures

3.1 SEIRA Spectroscopy

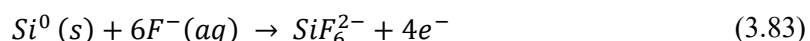
3.1.1 Electroless Deposition

Au-Film The nanostructured Au-film was created by electroless gold deposition described by Miyake et al.⁷³ First the surface of the Si prism was polished with alumina powder (microgrit WCA-9, grain size: 6 μm) and rinsed with water. Afterwards it was immersed into a 400 g/L NH_4F solution for 2 minutes to remove the oxide layer on the surface. Subsequently, at a temperature of 65 °C, the Au-film was deposit by adding an Au plating solution to the surface.

The deposition was aborted after 1:10 min by dilution with water. The plating solution contains a mixture of reductants (0.3 M Na₂SO₃, 0.1 M Na₂S₂O₃*5H₂O and 0.1 M NH₄Cl), 2 % HF and 0.03 M NaAuCl₄*H₂O. During the deposition an Au (III) reduction and a Si oxidation reaction takes place:



Ag Film The Ag Film was also created by electroless deposition. Here, the prism was polished with alumina powder (microgrit WCA-9, grain size: 6 µm) and rinsed with water. The immersion of the prism into the NH₄F is equally to the Au film production. The deposition occurred at room temperature in a water bath. For 2 min. a solution of 2 % HF and AgNO₃ (0.02 mM) was added to the prism and the reaction was stopped by dilution of water. The redox reaction on the prism created a thin Ag-film.



3.1.2 Electrochemically Cleaning

Au-Film After the electroless deposition the Au-film was cleaned electrochemically. For this purpose, the Si prism with the Au film was implemented in the spectro-electrochemical cell as explained in chapter 2.1.1. Afterwards six oxidation/reduction cycles were conducted in a potential range between 0.1 V to 1.4 V in 0.1 M HClO₄ solution. During and before the electrochemical treatment the cell was purged with argon to avoid the production of aggressive oxygen species. A voltammogram of the cleaning process is shown in **Figure 18**.

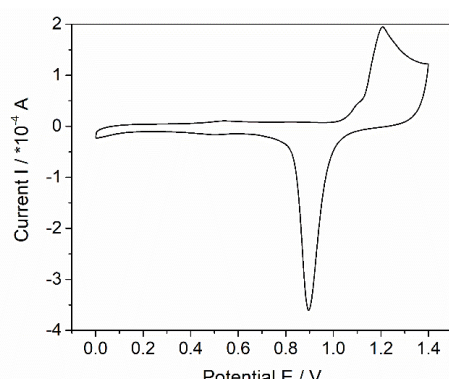


Figure 18: Voltammogram of the cleaning process for the Au-film with a reduction peak at 0.92 V.

3. Material and Methods

Here Au oxidation occurs at a potential higher than 1.1 V and a single reduction peak at ca. 0.92 V can be seen. Based on the reduction peak area the real Au surface area can be calculated using the Au oxide reduction charge density method. Therefore, the amount of charge that was necessary to reduce the surface Au-oxide was determined with the reduction area and compared with the specific charge density of $400 \mu\text{C cm}^{-2}$. After the cleaning procedure the surface was cleaned with water.⁷⁴

Ag Film Like the Au film also the Ag film was treated electrochemically. In a potential range from 0 V to -2 V six oxidation/reduction cycles were applied, before and during the measurement the cell was purged with Ar. The voltammogram does not show specific Ag reduction/oxidation peaks. After the electrochemical treatment the surface was cleaned with water. SEM pictures show a different morphology before and after the cleaning procedure (**Figure 19**). Individual Ag islands connect during the electrochemical measurement. Compared to the Au film the Ag islands are of higher diameter and the film is less dense. With EDX-spectra (energy dispersive X-ray spectroscopy) of the prism Ag and Si can be detected (**Figure A 2**). SEM pictures and EDX spectra were recorded together with C. Fahrenson from the ZELMI at the TU Berlin.

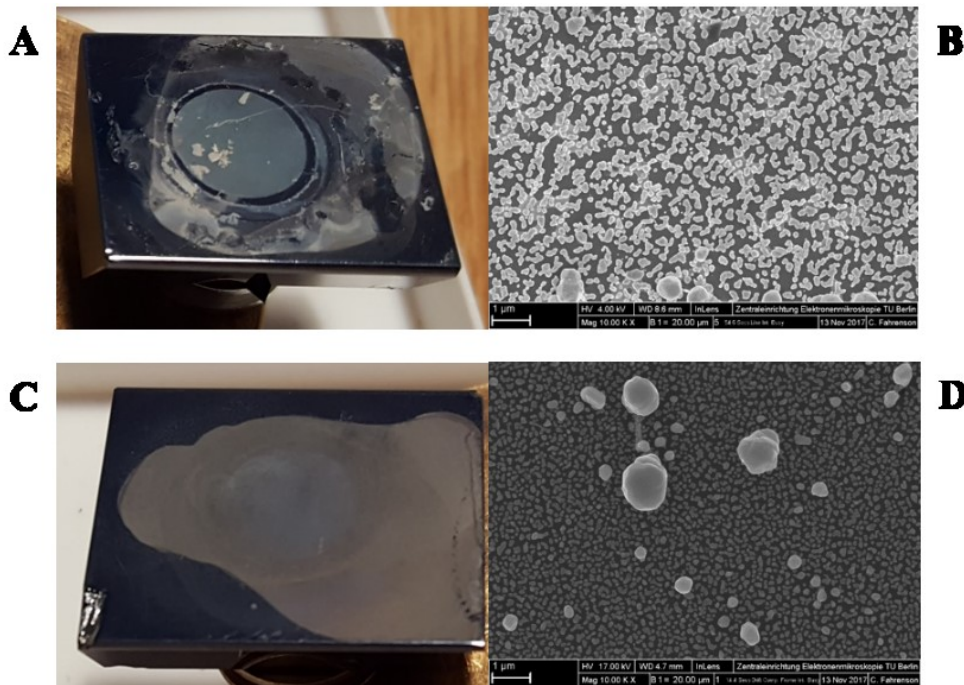


Figure 19: Picture of the prism and SEM picture of the Ag-film before (**C, D**) and after (**A, B**) an electrochemically treatment, is shown. SEM pictures were recorded together with C. Fahrenson from the ZELMI at the TU Berlin.

3.1.3 Vibrational Spectroscopy of the Biomimetic Interfaces

To detect the formation of the SAM, the spectro-electrochemical cell was implemented in the spectrometer after the electrochemical cleaning and buffer spectra were detected until an equilibrium was reached. Subsequently, the surface was cleaned with buffer and water to get rid

of ions on the surface. After cleaning with alcohol, a 1 mM solution of SAM diluted in alcohol (ethanol or 1-propanol) was added to the surface. After 16-20 h the solution was removed, and the surface cleaned with alcohol, water and buffer. Finally, buffer was filled inside the cell. The different steps were detected using SEIRAS. The spectrum of a nitrile SAM is shown in **Figure 20 A** and of the mixed WK3SH/6MH SAM in **Figure 20 B**. To prepare the vesicles for the tBLM a procedure by Schmitt et al was followed with a final concentration of 0.5 mg mL⁻¹ by extrusion through a polycarbonate filter with a pore size of 100 nm.⁷⁵ For the construction of the tBLM on top of the phase-separated SAM, unilamellar vesicles of the corresponding lipids (for POPC:POPG:CLSCN a ratio of 5:4 and for POPC:PE-N₃ a ratio of 4:1 was used) were added. After 2 h, the assembly was aborted by exchange with fresh buffer.

For spectro-electrochemical measurements the buffer solution was purged with Ar for 10 minutes to avoid electrochemical reactions of oxygen species on the metal surface. Then the chosen potential was applied, and the solution was purged during the measurement.

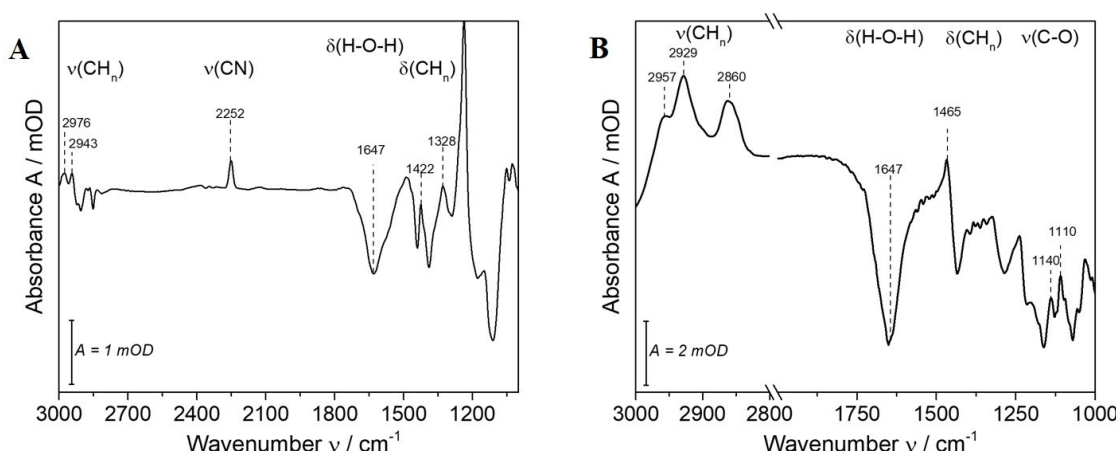


Figure 20: IR difference spectra of MBN against buffer (**A**), the CN vibration is marked at 2252 cm⁻¹, the huge negative band at 1647 cm⁻¹ corresponds to the H-O-H vibration of displaced water and at high frequencies (~2900-3000 cm⁻¹) and around 1300-1470 cm⁻¹ the CH_n bending and stretching vibrations of the alkyl chains are observable. The IR difference spectra of WK3SH/6MH against buffer is shown in (**B**), here additional to the vibrations mentioned for the MBN SAM the vibrations of the buffer around ~1100 cm⁻¹ is shown.

3.2 ATR-IR and BioATR-IR Spectroscopy

ATR ATR-IR was used for solvatochromic measurements. On that account the Si prism was polished and immersed with NH₄F like for the electroless metal deposition (chapter 2.1.1). Afterwards, the prism was cleaned with water and the spectro-electrochemical cell was assembled. Once the cell was implemented in the spectrometer the pure solvent was detected until the equilibrium is reached followed by the measurement of the sample dissolved in the solvent. Difference spectra were calculated using the OPUS 5.5 software. Solvents used for this

3. Material and Methods

solvatochromic measurements and their properties are summarized in **Table 6**. The parameters of the solutes for the solvatochromic measurements are summarized in **Table 7**.

Table 6: Summary of the solvents used for solvatochromic measurements and their corresponding dielectric constant and refractive indices.^{76,77}

Solution	dielectric constant	refractive index
2-methylbutan	1.84	1.35
n-hexane	1.88	1.37
n-heptane	1.92	1.39
cyclohexane	2.02	1.43
toluol	2.38	1.50
tetrachloromethane	4.89	1.45
tetrahydrofuran	7.58	1.41
dichloromethane	8.93	1.42
1-Propanol	20.45	1.39
acetone	20.56	1.36
ethanol	24.55	1.36
methanol	32.66	1.33
dimethyl sulfoxide	46.45	1.48
propylene carbonate	64.92	1.42
aqueous solution (phosphate buffer pH 7.0)	78.36	1.33

Table 7: Parameters for the Onsager model of the solutes used in this work.

Solution	density/ kg×m ⁻³	dipole moment/ Cm
ACN	786	1.3×10 ⁻²⁹
CHCN	919	1.53×10 ⁻²⁹ a
MeSCN	1052	7.83×10 ⁻²⁹ a
COOHC ₅ N ₃	a	1.46×10 ⁻²⁹ a

^aValue obtained from the DFT calculations. As there were no data available for the density of COOHC₅N₃ the cavity radius was determined by the DFT calculation.

BioATR For the IR spectroscopic measurements with the BioATR setup the sample compartment must be cleaned first. Therefore, a spectrum ‘cleaning_0’ of the empty compartment was taken and served as reference. Subsequently the compartment was cleaned with 20 µL of a 1% SDS solution followed by 20 µL of water for 10 times to remove the SDS residues and dry the compartment with nitrogen gas. Afterwards a spectrum ‘cleaning_1’ was detected and the difference spectrum with the reference was calculated. The procedure was repeated as long as there occur no difference bands between two cleaning steps. If the cell compartment was clean the buffer solution was measured overnight, and an average absorption spectrum was generated using the Bruker OPUS software 5.5. Next, the sample with the buffer was filled in the compartment and measured for at least 30 minutes.

3.3 EIS

For EIS measurements the cell was purged with Ar for 10 min.. Then the needle was taken out of the solution but the cell over the solution phase was further purged to prevent oxygen dissolved into the buffer. The measurement was controlled using the FRA or Nova software. For the evaluation, the data were plotted in the normalized admittance plot **Figure 6**. Thus, the capacitance of the system could be calculated pro area using the Au area determined by the oxide reduction charge density method. For the metal/SAM interface an electric circuit of $R_{SAM}C_{SAM}-R_{sol}$ and for the metal/tBLM $R_{spacer}C_{spacer}-R_{bilayer}C_{bilayer}-R_{sol}$ was applied, but more precisely the CPE will be applicable to $R_{spacer}Q_{spacer}-R_{bilayer}Q_{bilayer}-R_{sol}$. (**Figure 21**)

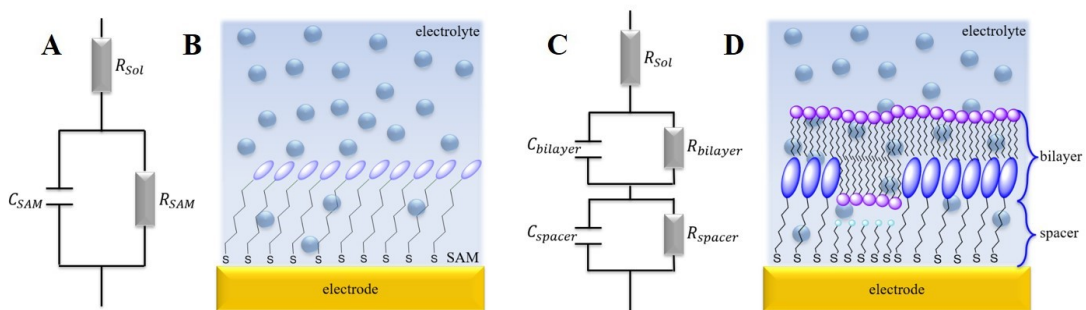


Figure 21: The electric circuit for the corresponding Au/SAM system with C_{SAM} , R_{SAM} and R_{sol} (A, B) and for the Au/tBLM system with C_{Spacer} , R_{Spacer} , $C_{bilayer}$, $R_{bilayer}$ and R_{sol} (C, D) is shown.

3.4 DFT

To perform DFT calculations the software Gaussian09 was used.⁷⁸ The hybrid functional B3LYP and the basis set 6-311++G(2d,2p) was selected for the solvatochromic calculations.⁷⁹⁻⁸²

3. Material and Methods

For the electric-field dependent C5CN and C6CN calculations for the first optimization 6-311G* was used and for the optimization and frequency calculation with an applied electric field 6-311++G(d,p).

To investigate the sensitivity of different nitrogen containing Stark reporter groups solvatochromic calculations of small molecules were done. As reporter groups the nitrile (-CN), the thiocyanate (-SCN) and azide ($-N_3$) group and for the small molecules cyclohexane carbonitrile (CHCN), methyl thiocyanate (MeSCN) and 5-Azidopentanoic acid ($COOHC_5N_3$) were chosen. First, optimization in vacuo was carried out, followed by optimization in different solvents by using the SCRF method.^{83–102} For this method the dielectric constant of the chosen solvent was written at the end (under the molecule coordinates) in the *.com file and in the input line the command scrf=(solvent= generic, read) was selected. After the optimization the frequencies were calculated, and the vibrational frequency of the Stark reporter plotted against the solvent electric field to investigate the Stark tuning rate.

For electric-field dependent calculations of C5CN and C6CN the 6-311G* basis set and B3LYP functional were used. The optimized molecular structure was oriented with the C≡N bond along the z-axis. For the optimization, the keywords “opt=tight” and “int=ultrafine” and anharmonic frequency calculations with 6-311++G** were selected while applying different electric fields along the z-axis.

4. Results and Discussion

1. Stark Reporter Groups

1.1 Results of the Solvatochromic IR and DFT Experiments

The nitrile, thiocyanate and azide group are VSE reporters and are applicable in biological systems. The respective modes appear in a spectral region which is free from any interfering contributions from vibrational modes of proteins or membrane components.

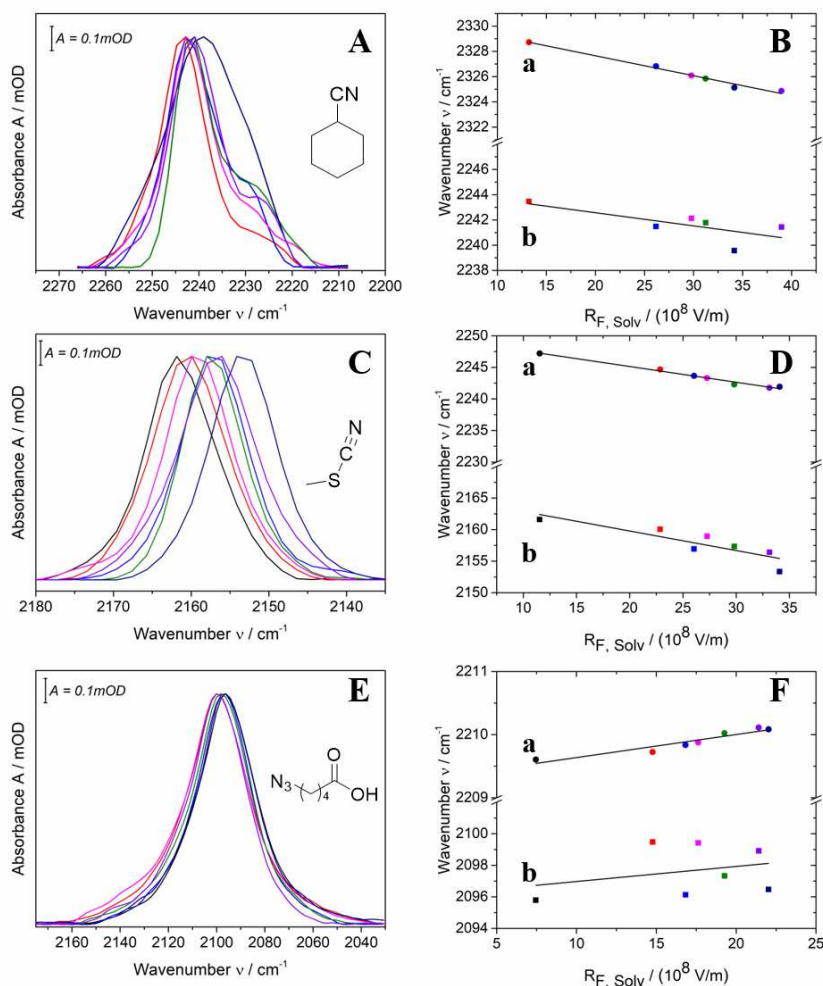


Figure 22: A, C, E show the normalized bands obtained in Bio-ATR experiments of the nitrile, thiocyanate and azide Stark reporter group in different solvents: Cyclohexane (black), trichloromethane (red), tetrahydrofuran (blue), dichloromethane (magenta), acetone (green), dimethyl sulfoxide (dark blue) and propylene carbonate (purple). In B, D, F the respective frequencies are plotted against the solvent reaction field calculated from the Onsager theory (equation (2.78)) (b) and DFT calculations (a). The solid lines represent a linear fit to the data.

4. Results and Discussion

To demonstrate the sensitivity of these reporter groups to changes in the local electric field, solvatochromic Bio-ATR experiments and DFT calculations of small molecules were performed. The nitrile stretching mode exhibited an asymmetric band shape. Over a solvent reaction field from trichloromethane to propylene carbonate, the frequency of CHCN shifts approximately 2.03 cm^{-1} and 3.98 cm^{-1} in experiment and theory, respectively. (**Figure 22 A, B**) CHCN was not soluble in cyclohexane. MeSCN shows a single absorbance band and shifts of 5.2 cm^{-1} and 5.46 cm^{-1} for Bio-ATR measurements and DFT calculations, respectively, which represent the most pronounced shifts in the chosen solvent reaction field. (**Figure 22 C, D**) For COOHC_5N_3 , a broad absorbance band with a small shift of 3.13 cm^{-1} and 0.51 cm^{-1} for experiment and calculation were determined, respectively. (**Figure 22 E, F**) The most pronounced frequency shift of the nitrile and thiocyanate group was found in DMSO. It was observed that sulphur containing solvents have an influence on the frequency shift, similar to H-bonding or halogen containing solvents. Therefore, to calculate the frequency shifts of the reporter molecules, DMSO (dark blue in the spectra and fit) was neglected. The wavenumbers were plotted against the solvent reaction fields calculated with **equation (2.78)**. They followed a linear behaviour according to **equation (2.78)**, with the slope corresponding to the Stark tuning rate. The determined Stark tuning rate for both, experiments and calculations, for CHCN, MeSCN and COOHC_5N_3 are listed in **Table 8**.

1.2 Methods to Obtain the Stark Tuning Rate

Many techniques can be applied to determine the Stark tuning rate i.e. using vibrational Stark spectroscopy (VSS) in a frozen glass, solvatochromic IR measurements or quantum mechanical calculations.⁶¹ Each of these techniques suffer from considerable pitfalls. The most direct method to obtain the Stark tuning rate is the VSS. Whereas the resulting value $|\Delta\vec{\mu}|f$ contains the local electric field factor f , which is assumed to be $f=1.5 - 2.5$.^{61,65} Performing DFT calculations to determine the Stark tuning-rate an overestimation of ca. 25 % is observed.⁵⁹ Using the Onsager theory (**equation (2.78)**) to quantify the Stark tuning rate, also slightly overestimates the value due to the neglection of higher order polarizability effects.⁶¹ Nevertheless, assumptions made within in the Onsager theory lead to an underestimation of the Stark tuning rate. A spherical cavity accounts for only a few molecules; for most molecules the cavity would have another shape, such as ellipsoidal. Additionally, the Onsager theory lacks specific solute-solvent interactions. The assumptions of the Onsager theory and the resulting underestimations also apply for DFT-calculated wavenumbers using the polarizable continuum model (Theoretical Background chap. 5). Taking these underestimations into account, the different Stark tuning rates for benzonitrile of $1.43 \times 10^{-9}\text{ cm}^{-1}/(\text{Vm}^{-1})$ (after the correction with the missing factor of $4\pi/3$ in the Onsager equation in Bagchi, Fried Boxer)^{61,103} for solvatochromic measurements and $\approx 3.2 \times 10^{-9}\text{ cm}^{-1}/(\text{Vm}^{-1})$ for VSS, based on $|\Delta\vec{\mu}|f = 6.0 \times 10^{-9}\text{ cm}^{-1}/(\text{Vm}^{-1})$ can be explained. This underestimation by a factor of ca. 2 also accounts for different carbonyls (ethyl acetate, methyl benzoate, ethyl thioacetate, butyl thiobenzoate and *N,N*-dimethylacetamide) when compared VSS to solvatochromic results.⁶⁵ Schneider and Boxer analysed the effect of different substitutions and conjugation of simple oxoesters, thioesters and amides on the Stark tuning rate. They found out that the carbonyl tuning rate ($|\Delta\vec{\mu}_{C=O}|f$) of R-C(O)X-R is mostly influenced by the heteroatom (X), with larger effects for less electronegative heteroatoms, which can be represented by the general trend of O < N < S. Increasing conjugations showed only a small effect on the Stark tuning rate.

Nevertheless, the substituent can significantly increase the Stark tuning rate among others due to intramolecular interactions.⁶⁵

1.3 Determination of the Stark Tuning Rates for -CN, -SCN and -N₃

In this work we used the solvatochromic IR and DFT method to obtain the Stark tuning rate (STR).

Comparing the literature values of the Stark tuning rate for acetonitrile (ACN) $2.3 \times 10^{-9} \text{ cm}^{-1}/(\text{Vm}^{-1})$ and MeSCN $3.6 \times 10^{-9} \text{ cm}^{-1}/(\text{Vm}^{-1})$, it can be seen that the Stark tuning rate for MeSCN is larger by a factor of ca. 0.6.^{62,64} Both molecules consist of one methylene group with no electron donating or withdrawing characteristic.

Table 8: Results of the solvatochromic experiments and calculations for CHCN, MeSCN and COOHC₅N₃; the frequency shifts and the determined Stark tuning rates are summarized.

	-CN		-SCN		-N ₃	
	exp.	calc.	exp.	calc.	exp.	calc.
Frequency shift $\Delta\tilde{\nu}$ / cm ⁻¹	2.03	3.98	5.2	5.46	3.13	0.51
$ \Delta\vec{\mu} \times 10^{-9} \text{ cm}^{-1}/(\text{Vm}^{-1})$	2.0	3.2	6.6	5.0	2.0	0.88
$ \Delta\vec{\mu} \times 10^{-9} \text{ cm}^{-1}/(\text{Vm}^{-1})$ without DMSO ^a	1.6	--	4.8	---	---	---

^a The -CN and -SCN vibrations showed greater than expected frequency shifts in DMSO due to further DMSO C≡N interactions. This effect was larger than the influence of the solvent electric field. Therefore, values with DMSO were neglected for -CN and -SCN.

Therefore, the additional sulphur may be responsible for the higher sensitivity to changes of the local electric field, perhaps because of a higher electron density and electron movement based on the mesomeric character of the thiocyanate group. In the present solvatochromic experiments, the Stark tuning rate obtained by the slope in **Figure 22 D** and multiplied by a factor of 2 (*vide supra*) is $6.6 \times 10^{-9} \text{ cm}^{-1}/(\text{Vm}^{-1})$ for the ATR measurement and $5.0 \times 10^{-9} \text{ cm}^{-1}/(\text{Vm}^{-1})$ for DFT calculations. These two values are approximately two times larger than the value obtained from VSS. The literature value $|\Delta\vec{\mu}|f$ for MeSCN was found to be $7.2 \times 10^{-9} \text{ cm}^{-1}/(\text{Vm}^{-1})$. We assumed f to be 2 but it was not explicitly calculated for MeSCN. It is expected to be in the range from $f = 1.5$ to 2.5, which leads to a Stark tuning rate from $2.9 \times 10^{-9} \text{ cm}^{-1}/(\text{Vm}^{-1})$ to $4.8 \times 10^{-9} \text{ cm}^{-1}/(\text{Vm}^{-1})$. The experimental value for the Stark tuning rate is still not in this range but the one obtained from DFT calculations is close to the value obtained by VSS with a local correction factor of $f = 1.5$. The experimental data include the frequency of MeSCN in DMSO, which is not only influenced by the solvent electric field, but other effects have a large influence on the frequency (*vide supra*). The linear fit in **Figure 22 D** without the value for DMSO leads to a slope of -0.24 and thereby to a Stark tuning rate of $4.8 \times 10^{-9} \text{ cm}^{-1}/(\text{Vm}^{-1})$, which is in perfect agreement with the VSS value and a local

4. Results and Discussion

correction factor of $f = 1.5$. Hence, it was used for further calculations in this work as the Stark tuning rate for thiocyanate.

Suydam and Boxer found that the Stark tuning rate of aromatic nitriles are greater than for aliphatic nitriles.⁶² Therefore, the Stark tuning rate of CHCN is expected to be between the value for ACN and benzonitrile of $3.2 \times 10^{-9} \text{ cm}^{-1}/(\text{Vm}^{-1})$.^{62,64} In comparison to benzonitrile, CHCN lacks a conjugated π -system which is associated with the -I-effect of the cyanide group that withdraws electrons from the aromatic π -system. For the solvatochromic ATR and DFT measurements $2.0 \times 10^{-9} \text{ cm}^{-1}/(\text{Vm}^{-1})$ and $3.2 \times 10^{-9} \text{ cm}^{-1}/(\text{Vm}^{-1})$ were obtained as Stark tuning rates, respectively (**Figure 22 B**), multiplied by a factor of 2. Whereas the DFT value is similar to the one for benzonitrile obtained with VSS, the Stark tuning rate determined by ATR is closer to the Stark tuning rate of ACN. Similarly, to thiocyanate, the experimental data were fitted without the value for DMSO, which leads to an even smaller Stark tuning rate of $1.6 \times 10^{-9} \text{ cm}^{-1}/(\text{Vm}^{-1})$. The C≡N vibrational band shows a very asymmetric band shape, which could lead to mistakes in the frequency determination. As above-mentioned, Schneider and Boxer showed that the Stark tuning rate undergoes only small changes with increasing conjugation. Therefore, the Stark tuning rate of CHCN should be close to the Stark tuning rate of benzonitrile, which is true for the DFT calculated solvatochromic value of $3.2 \times 10^{-9} \text{ cm}^{-1}/(\text{Vm}^{-1})$.⁶⁵

For the azide stretching mode, only a few values were obtained in literature due to the small frequency shifts in different solvents and thus the small resultant sensitivity to changes of the local electric field. However, azides are popular in biomimetic systems, since they can easily be introduced by so-called ‘click’ reactions.^{104,105} One example for an azide Stark tuning rate was obtained by Suydam and Boxer of azidotrimethylsilane with VSS, i.e. $(2.9 \pm 0.72) \times 10^{-9} \text{ cm}^{-1}/(\text{Vm}^{-1})$ (with a correction factor of $f = 1.5$ to 2.5).⁶² The solvatochromic IR and DFT experiments reveal values of $2.0 \times 10^{-9} \text{ cm}^{-1}/(\text{Vm}^{-1})$ and $0.88 \times 10^{-9} \text{ cm}^{-1}/(\text{Vm}^{-1})$, respectively. However, DMSO does not have such a strong influence on the azide vibration and therefore was included for the fit. The values obtained with ATR are within the abovementioned limits of the Stark tuning rate determined by VSS. Thus, for the azide vibration a Stark tuning rate of $2.0 \times 10^{-9} \text{ cm}^{-1}/(\text{Vm}^{-1})$ is assumed, which represents the upper limit for the Stark tuning rate. Thus, the calculated electric field will represent a lower limit calculated with this value.

2. Self-assembled Monolayers on Au and Ag Electrodes

Results of this chapter were part of my master thesis and were published in Staffa, J. K. et al. Determination of the Local Electric Field at Au/SAM Interfaces Using the Vibrational Stark Effect. *J. Phys. Chem. C* **121**, 22274–22285 (2017).^{21,54} Copyright 2017 American Chemical Society.

C5CN, C6CN and MBN immobilized on Au and Ag were analysed in order to study the local electric field of the simplest biomimetic interface. Measurements were performed in a potential range of 0.4 V to -0.4 V and 0.1 V to -0.6 V for Au/SAM and Ag/SAM, respectively.

2.1 Alkyl Nitrile SAMs on Au Electrodes

Electrochemical impedance measurements Potential-dependent EIS measurements were conducted between 0.4 V and -0.4 V in 0.5 V steps. The normalised admittance plots are shown in **Figure 23 A, B** considering an Au surface of 1.6 cm^2 . The capacitance C of each applied potential E was determined graphically by taking the radius of the semicircle and multiplied by a factor of two.^{10,26} The capacitances of the potential-dependent plots varied in different measurements by the minima, depending on the quality of the SAM, leading to capacitances between 5 and $8 \mu\text{F}/\text{cm}^2$ and 5 and $13 \mu\text{F}/\text{cm}^2$ for C5CN and C6CN, respectively. These values are in good agreement with literature.^{106,107}

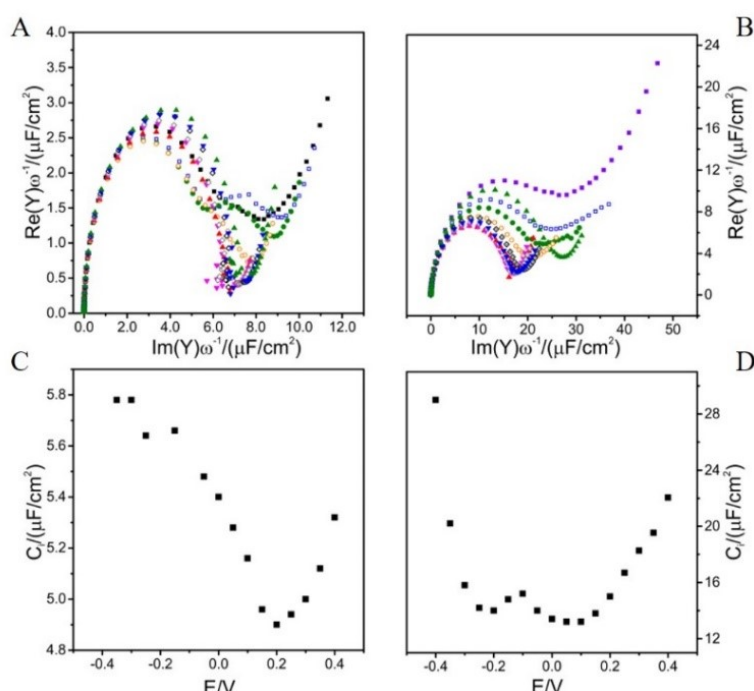


Figure 23: Potential-dependent normalized admittance plot for C5CN (**A**) and C6CN (**B**) on nanostructured Au-electrodes: 0.4 V (black ■), 0.3 V (blue □), 0.25 V (olive ●), 0.2 V (orange ○), 0.1 V (red ▲), 0.0 V (magenta ▼), -0.05 V (grey ◇), -0.15 V (black ◇), -0.25 V (blue ▼), -0.35 V (olive ▲). (**C**) and (**D**) represent the potential-capacitance plots for C5CN and C6CN, respectively. *Reprinted with permission from Staffa, J. K. et al. Determination of the Local Electric Field at Au/SAM Interfaces Using the Vibrational Stark Effect. J. Phys. Chem. C 121, 22274–22285 (2017). Copyright 2017 American Chemical Society.*

Solvatochromic measurements To determine the Stark-tuning rate, solvatochromic experiments were performed with acetonitrile (ACN) in the ATR-IR mode and with DFT calculations. ACN shows a good solubility in different solvents compared to C5CN and C6CN. Solvents with the ability to form H-bonds have a strong influence on the CN vibration (Theoretical Background chap. 4.1). Determining the H-bonding effect on the C≡N vibration, ACN and *n*-mercaptopbutylnitrile (C4CN) were dissolved in buffer (PBS, pH 7) and propylene carbonate (PC) and measured in the transmission sandwich cell. PC generates a similar, but not identical, solvent reaction field according to equation (2.78). Thereby a shift of 7.8 cm^{-1} for ACN and 8.3 cm^{-1} for C4CN was determined. (**Figure 24 B, Figure A 3**) Hence, in the case of

4. Results and Discussion

protic solvents the wavenumber was corrected by 8 cm^{-1} . Taking **equation (2.78)** into account the frequencies follow the solvent reaction field in an approximately linear behaviour with a slope of $1.2 \times 10^{-9}\text{ cm}^{-1}/(\text{Vm}^{-1})$ for the ATR measurement. Actually, the frequencies of ACN in methanol, ethanol and propanol also follow the linear relationship after the abovementioned correction. Previous results showed similar Stark tuning rates for H-bonded and non-H-bonded nitriles.⁶⁷ The broadening of the absorbance band in the case of C4CN in H₂O (15 cm^{-1}) compared to PC (10 cm^{-1}) was described before, as being due to interactions of the nitrile group and the solvent, either via the π -orbital or the p-orbital on the nitrogen, or due to different angles of the H-bond with respect to the C≡N axis.⁶⁶ (**Figure A 3**)

For solvatochromic DFT calculations, first ACN was calculated in different solvents using the solvent model described in Theoretical Background Chap. 5. The calculated C≡N frequencies are shown in **Figure 24 A**, corresponding to a slope of $0.9 \times 10^{-9}\text{ cm}^{-1}/(\text{Vm}^{-1})$. Compared with the Stark tuning rate of the ATR experiments this value is slightly smaller. It should be taken into account that the higher calculated wavenumbers compared to the experimental data are due to intrinsic errors of the DFT calculations. These errors are systematic and can be neglected with respect to the effect of the solvent reaction field. Second, DFT calculations were performed for C5CN and C6CN in vacuo by employing an external electric field. The optimised SAM structures were oriented such that the C≡N axis and the direction of the electric field were parallel to each other. Taking this as a starting point, the anharmonic C≡N stretching was calculated and plotted against the external electric field in **Figure 24 C**. The wavenumber increased linearly with the electric field corresponding to a Stark tuning rate of $3.9 \times 10^{-9}\text{ cm}^{-1}/(\text{Vm}^{-1})$ for both C5CN and C6CN.

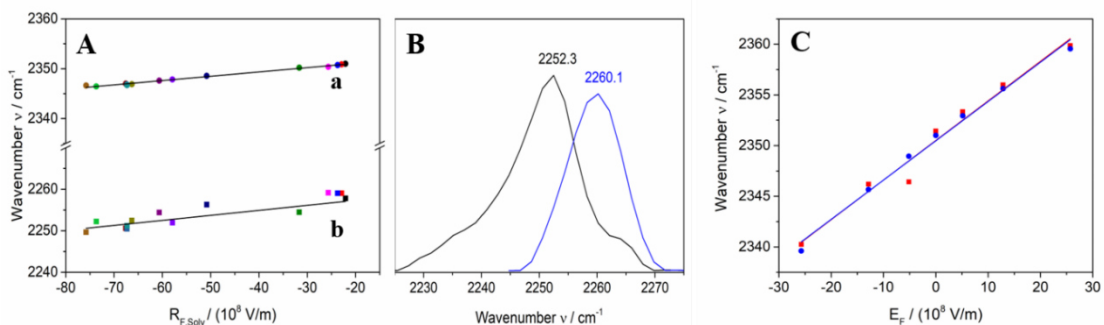


Figure 24: Solvatochromic ATR measurements (**A**) of ACN (**b**) and DFT calculations (**a**). The data points from left to right refer to isopentane, n-hexane, n-heptane, cyclohexane, tetrachloromethane, tetrahydrofuran, dichloromethane, propanol, acetone, ethanol, methanol, dimethyl sulfoxide, propylene carbonate. The frequencies determined in solutions of the three alcohols were corrected for the hydrogen bonding effects by -8 cm^{-1} . (**B**) shows the H-bonding effect on ACN in water (black) and PC (blue). In (**C**) the results of the DFT calculations with an external applied electric field on the C≡N vibration of C5CN (blue) and C6CN (red) is represented.

Reprinted with permission from Staffa, J. K. et al. Determination of the Local Electric Field at Au/SAM Interfaces Using the Vibrational Stark Effect. J. Phys. Chem. C 121, 22274–22285 (2017). Copyright 2017 American Chemical Society.

SEIRA Potential-dependent SEIRA experiments for C5CN and C6CN were performed in 0.1 V steps and the absorbance bands are shown in **Figure 25 A, D**. With increasing potential, the intensity decreases, and the frequency shows a blue-shift. These shifts were reversible in the

same experiment and showed a high reproducibility of SEIRA in different experiments within the experimental accuracy.

The slightly asymmetric band shape could be described satisfactorily by a single Gaussian function (**Figure 26 A**). A second Gaussian function (**Figure 26 B**) did not lead to an improvement of the fit (**Figure 26 C**). The results of the analysis reveal a linear relationship between the potential and the intensity and a non-linear behaviour for the frequencies (**Figure 25 C, F and B, E**).

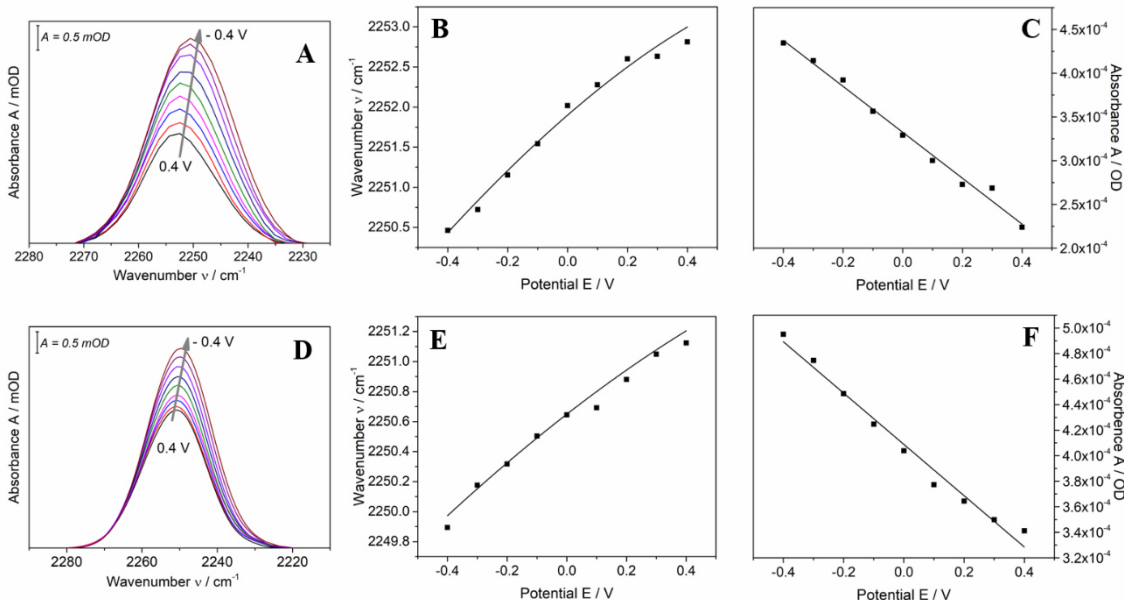


Figure 25: Potential-dependent C≡N absorbance band of C5CN (**A**) and C6CN (**D**). The colours belong to a potential of 0.4 V (black), 0.3 V (red), 0.2 V (blue), 0.1 V (magenta), 0 V (green), -0.1 V (dark blue), -0.2 V (purple), -0.3 V (dark purple) and -0.4 (brown). Potential-dependent changes of the frequency (**B, E**) and the intensity (**C, F**) are shown for C5CN and C6CN, respectively.

*Reprinted with permission from Staffa, J. K. et al. Determination of the Local Electric Field at Au/SAM Interfaces Using the Vibrational Stark Effect. *J. Phys. Chem. C* **121**, 22274–22285 (2017). Copyright 2017 American Chemical Society.*

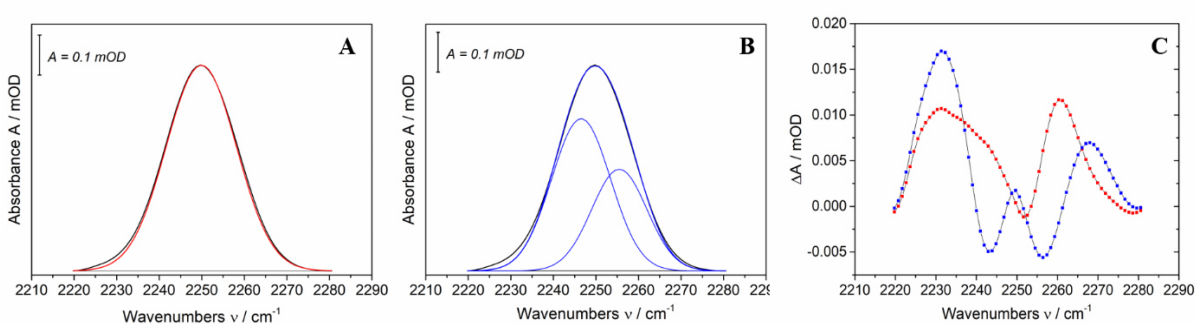


Figure 26: Fit of the C6CN absorbance band (black) at -0.4 V with one Gaussian band (red) and two Gaussian bands (blue) (**A, B**). The difference between the absorbance band and the Gaussian fit for one (red) and two (blue) Gaussian bands are shown in (**C**).

2.2 Aromatic and Aliphatic SAMs on Ag Electrodes

Potential-dependent SEIRA experiments were performed for three different SAMs (MBN, C5CN and C6CN) on a nanostructured Ag-film and compared to the electric fields on a nanostructured Au-film.

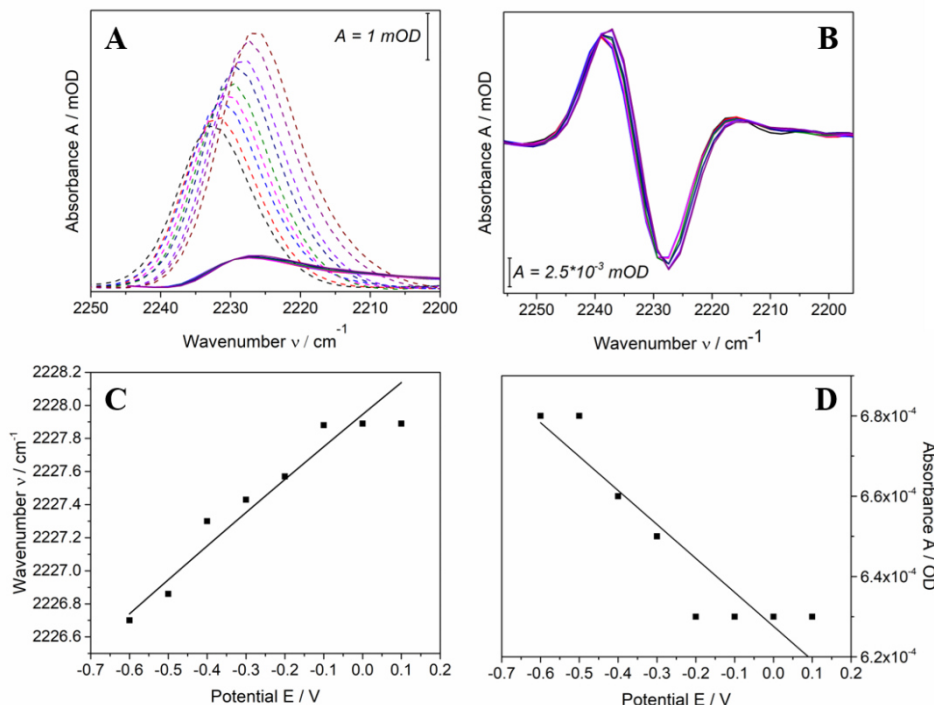


Figure 27: The C≡N absorbance band of MBN on nanostructured Au (dotted lines) and on nanostructured Ag (compact lines) and the corresponding second derivative is shown in (A, B) with the potentials 0.4 V (dotted black), 0.3 V (dotted red), 0.2 V (dotted green), 0.1 V (dotted blue, black), 0 V (dotted purple, red), -0.1 V (dotted magenta, blue), -0.2 V (dotted grey, magenta), -0.3 V (dotted dark yellow, green), -0.4 V (dotted dark blue, dark blue), -0.5 V (purple), -0.6 V (dark purple). In (C, D) the potential-dependent wavenumber and intensity changes are shown and can be described with a linear relationship, respectively.

MBN is an aromatic nitrile molecule that was already studied in the past.^{57,108} The potential-dependent SEIRA measurements on Au by Schkolnik et al. could be reproduced in this work with a shift of the nitrile stretching frequency of 5.6 cm⁻¹.¹⁰⁹ For the nanostructured Ag-film, potentials were applied between 0.1 V and -0.6 V in 0.1 V steps and this led to a shift of 3.9 cm⁻¹. The intensity of the nitrile absorbance band on Ag was much smaller (by a factor of 3) compared to the absorbance band on Au. (**Figure 27 A**) The potential-dependent shifts of the wavenumber and the intensity turned out to be less pronounced. (**Figure 27 C, D**) However, the wavenumbers are in the same frequency region for Ag and Au. With decreasing potential, a decrease of the wavenumber and an increase in intensity was detectable. During the measurement, a reference potential of 0.1 V was applied, and the reversibility of the shifts could be established. (**Figure A 5**) For -0.3 V, the wavenumber for Au and Ag could be assigned at the same position. The potential-dependent intensity and wavenumber changes could be described by a linear relationship. (**Figure 27 C, D**)

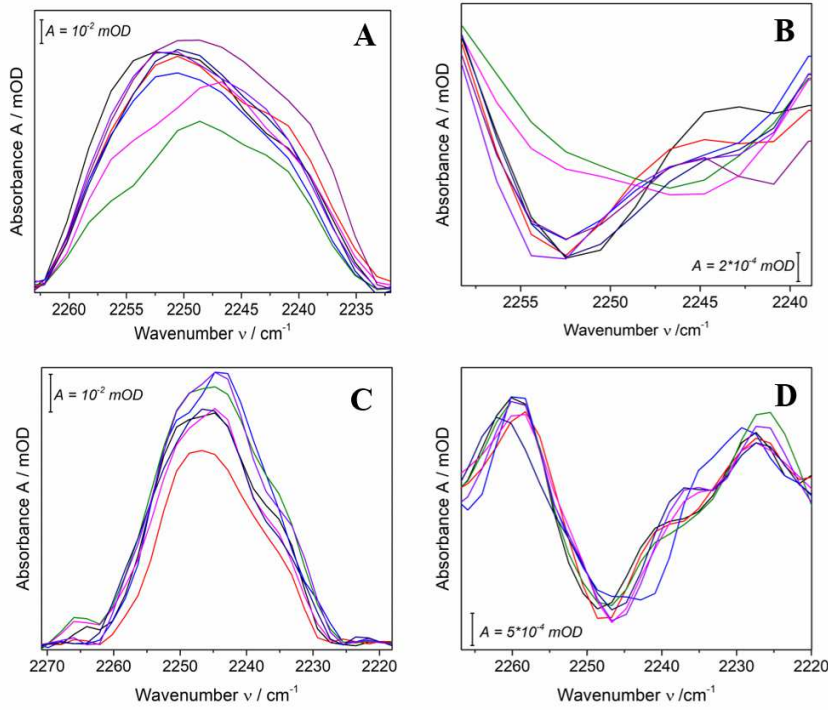


Figure 28: The absorbance band and second derivative of C5CN (**A, B**) and C6CN (**C, D**) is represented, respectively. The colours belong to potentials of 0.1 V (black), 0 V (red), -0.1 V (blue), -0.2 V (magenta), -0.3 V (green), -0.4 V (dark blue), -0.5 V (purple), -0.6 V (dark purple).

For the aliphatic nitrile SAMs, C5CN and C6CN, the absorbance band of the C≡N stretching was around 2252 cm^{-1} and 2247 cm^{-1} , respectively. In the case of C5CN a decreasing potential resulted in a frequency decrease and a slightly intensity increase. However, for C6CN a decrease in the potential leads to a decrease in wavenumber and an average increase in intensity. (**Figure A 6**) Using the second derivatives, the spectra analysis for both SAMs identified two absorbance bands, whereas the fit with two Gaussian functions did not lead to an improvement. Thus, the subsequent evaluation of the data was based on the fit of one Gaussian function. For C5CN, the potential-dependent frequency and intensity changes were described by a linear relationship and for C6CN by a linear and non-linear relationship, respectively. (**Figure A 6**) The absorbance bands on nanostructured Au and Ag are in the same region for C5CN and C6CN. (**Figure A 5**)

2.3 Comparison of the SAM Structure on Au and Ag

It was possible to create a nanostructured Au and Ag film on top of the IRE and construct aliphatic and aromatic nitrile SAMs on the surface. After performing potential-dependent SEIRA spectroscopy, a frequency and intensity shift of the C≡N stretching vibration was observed. In general, the changes were more distinct for the SAMs on the Au electrode. Creating nanostructured Au films for SEIRA in the ATR setup is a well-established method in comparison to Ag films. To perform SEIRA in the ATR mode, the metal film must be thermally and mechanically stable over a long period of time and thin enough such that the attenuated radiation can reach the self-assembled molecules. The Au film exhibits a small thickness and is

4. Results and Discussion

densely packed, whereas for the Ag film it is visible both with the eye and SEM pictures that it is less dense. (**Figure 19**) Running the electroless deposition for a longer time, the Ag film became thicker and no SEIRA signal was detectable. Additionally, the Ag film was less stable. It was removed upon touching whereas for Au the film had to be removed by polishing with alumina powder. To sum up, the Au film represents a superior support material for SEIRA spectroscopy. Though, it was possible to study interfacial electric fields effects at Ag films despite the poorer spectral quality that resulted in larger errors of the frequency and intensity determination. As a consequence of the less dense film, fewer molecules adsorb on the surface and therefore the SAM signal on Ag was much smaller. Best results were achieved for MBN that seems to form a more structured monolayer film compared to C5CN and C6CN. The C≡N vibration of MBN was symmetric, whereas for C5CN and C6CN at least two bands overlap. MD simulations of C5CN and C6CN on Au, performed by Dr. Tillmann Utesch within this project to support the experimental data, revealed an orientational distribution of the nitrile groups (**Figure A 4**). For C5CN, a distinctly more homogenous structure of the SAM was found compared to C6CN, as reflected by the distribution of the tilt angle of the C≡N bond (ϕ) with respect to the surface normal. In this respect, the C6CN SAM showed a substantial structural heterogeneity, consistent with the larger bandwidth of the SEIRA band for C6CN than for C5CN (20 vs 16 cm⁻¹).

Tilt Angle ϕ of the C≡N bond The lower intensity of C5CN and C6CN points to a stronger tilt of the C≡N bond to the surface and hence a larger tilt angle compared to MBN. For MBN on Ag a tilt of 0° was reported which quite differs from the tilt angle of thiophenol on Ag (24°-28°) whereas the tilt angles on Au were similar for both molecules (~40° for MBN and 49°-54° for thiophenol).⁴²⁻⁴⁶ In this work we used a tilt angle of 0° for MBN on Ag at the effective potential of zero charge. For C5CN and C6CN on Au the MD simulations predict tilt angles of 68° with $\Delta\phi \approx 10^\circ$ for C5CN and 63° with $\Delta\phi > 35^\circ$ for C6CN. (**Figure A 4**) For the alkyl nitriles on Ag the tilt angles were estimated considering the tilt of the methylene chains with respect to the surface normal of 30° on Au and 10° on Ag for alkyl thiols.³⁰ Assuming that the twist angle is similar for Au and Ag, one obtains a tilt angle of 45° for the nitrile group with respect to the surface normal for C5CN and C6CN at the effective potential of zero charge.

2.4 The Effective Potential of Zero Charge for the Au and Ag Interfaces

For the quantification of local electric fields according to **equation (2.67)** the frequency at the effective potential of zero charge v_0 and the electrode potential at which the electric field at the SAM/solution interface is zero, must be determined. The potential-dependent interfacial capacitances derived from the potential-dependent EIS measurements (**Figure 23**) confer the possibility to determine the effective potential of zero charge, corresponding to the potential of minimum capacitance.¹¹⁰ The shape of these curves varies somewhat from measurement to measurement, as also reported by Becka and Miller, due to impurities and ions in the SAM.¹¹⁰ In our case the (sub)-nanoscopic roughness of the metal film in the individual measurements associated with the amount of defects in the SAM are also relevant for different shapes of the curves. Nevertheless, a single minimum at ca. (0.2 ± 0.05) V was found for Au/C5CN, in contrast for Au/C6CN two minima at ca. 0.1 V and -0.2 V were identified. These double minima are mainly related to the structure of the C6CN film with its heterogenous distribution of the tilt angles with respect to the surface normal of the C≡N head group (*vide supra*).

Calculating the effective potential of zero charge according to **equation (2.56)**, the E_{PZC} for the bare metal is obtained to be 0.06 V for polycrystalline Au.¹¹¹ The value of $\Delta\phi_{SAM}$ for methyl-terminated SAMs is mainly influenced by the dipole moment contribution of the alkyl thiols. This can be approximately assumed by the dipole moment of the respective neutral radical thiol, the direction of the dipole moment points from the electrode to the solution.¹¹² It was observed that the modulus of the dipole moment increase with an increasing chain length. Corresponding to an increasing negative shift of the effective potential of zero charge ($\Delta\phi_{SAM} < 0$).¹¹³ On basis of this data and assuming that this trend applies also to nitrile-terminated SAMs, $E_{PZC,eff}$ of Au/C6CN would be expected to be more negative by 0.1 V compared to Au/C5CN due to the longer alkyl chain. Consequently, the value of $E_{PZC,eff}$ for Au/C5CN and Au/C6CN are estimated to be 0.2 V and 0.1 V, respectively, which agree with the minima of the potential-dependent capacitance plots. (**Figure 23**) The contribution of the nitrile function to the overall dipole moment is dependent on the tilt angle. Therefore, the second minima at more negative potentials for Au/C6CN can then be assigned to a SAM domain with larger tilt angles and thereby negligible for the contribution of the dipole moment to $\Delta\phi_{SAM}$. Altogether, one obtains a downshift of $E_{PZC,eff}$ compared to E_{PZC} . Correspondingly, ν_0 for C5CN and C6CN are estimated to be 2252.5 cm⁻¹ and 2250.8 cm⁻¹, respectively, determined from the potential-dependent SEIRA data. (**Figure 25**)

For the SAM-coated Ag electrode it was not possible to perform potential-dependent EIS measurements. Therefore, the value for $E_{PZC,eff}$ will be estimated. First, the distinctly more negative value of E_{PZC} for Ag of -0.92 V has to take into account.^{113,114} The coating by nitrile SAMs shifts the potential of zero charge to more positive values, like for Au. This effect may be relatively small in view of the chain length dependence of $\Delta\phi_{SAM}$ and yields a $E_{PZC,eff}$ of -0.85 V for Ag/C6CN and -0.75 for Ag/C5CN. Compared to the values for the $E_{PZC,eff}$ on Au, the values for Ag are negative, implying that the potential range studied for Ag lead to positive E_F (**equation (2.67)**) and the electric field points away from the electrode to the solution. Whereas for SAM coated Au electrodes, E_F is negative in the chosen potential range and the electric field points to the electrode from the solution. The values for ν_0 for Ag electrodes were taken from the potential-dependent wavenumber plots of C5CN and C6CN. Based on an approximately linear potential-dependent behaviour of the nitrile stretching frequency, ν_0 for Ag/C5CN and Ag/C6CN were obtained as 2250.39 cm⁻¹ and 2245.04 cm⁻¹, respectively. (**Figure A 6**) The frequencies at the effective potential of zero charge are in the same region for the Au and Ag electrodes. For MBN the $E_{PZC,eff}$ on Ag was obtained by Schkolnik et al. to be 1.277 V in a potential range of 0.1 V to -0.5 V by calculating the change in the work function of the metal. This method may be associated with considerable errors because the quality of the SAM and the nanostructured surface were not considered. The MBN SAM has approximately the same thickness as C5CN and therefore a $E_{PZC,eff}$ of -0.75 V will be assumed. In this case, E_F is positive ($E_{PZC,eff} < 0$) and points away from the electrode. This $E_{PZC,eff}$ value leads to a frequency at an effective potential of zero charge of 2226.53 cm⁻¹, derived from the potential-dependent SEIRA measurements and assuming a linear potential behaviour of the nitrile-frequency.

2.5 The Stark Tuning Rate for Nitrile-terminated Thiols

The different methods to obtain the Stark tuning rate and the corresponding pitfalls were already discussed in chap. 1.2. To obtain the tuning rate for alkyl nitrile SAMs solvatochromic ATR and DFT experiments of ACN lead to values of $2.6 \times 10^{-9} \text{ cm}^{-1}/(\text{Vm}^{-1})$ and $1.8 \times 10^{-9} \text{ cm}^{-1}/(\text{Vm}^{-1})$, after the correction with a factor of 2 for the values obtained by the slopes of the frequency-dependent solvent reaction field plots (**Figure 24 A**) (see chap. 1.2). The Stark tuning rate determined by VSS is $\approx (2.3 \pm 0.6) \times 10^{-9} \text{ cm}^{-1}/(\text{Vm}^{-1})$ (after correction of f).¹¹⁵ Additional to the solvatochromic experiments, DFT calculations of C5CN and C6CN as described in Material and Methods cap. 3.5 were performed by applying an electric field parallel to the C≡N axis. The results in **Figure 24 C** show a linear dependent of the nitrile stretching on the applied electric field with a slope of $3.9 \times 10^{-9} \text{ cm}^{-1}/(\text{Vm}^{-1})$ for both molecules. As already mentioned, values obtained with DFT are expected to be overestimated by 25%, which leads to a value for the Stark tuning rate of $3.0 \times 10^{-9} \text{ cm}^{-1}/(\text{Vm}^{-1})$. All the obtained values are within the limits of the value for ACN determined with VSS, such that for the following analysis the corrected DFT value of $3.0 \times 10^{-9} \text{ cm}^{-1}/(\text{Vm}^{-1})$ will be used. This represents the upper limit for the Stark tuning rate for aliphatic nitriles and therefore the calculated local electric fields present a lower limit. For MBN the Stark tuning-rate, obtained by Schkolnik et al., of $6.0 \times 10^{-9} \text{ cm}^{-1}/(\text{Vm}^{-1})$ was used for further analyses.¹⁰⁹ In general, this value fits to the fact that for aromatic nitrile SAMs larger tuning rates were obtained than for alkyl nitriles.⁶² C5CN and MBN SAMs possess a similar thickness but the total potential-dependent frequency shift of the nitrile stretching was ca. 5.5 cm^{-1} for Au/MBN and 2.35 cm^{-1} for Au/C5CN.¹⁰⁹ This ca. two-times larger overall shift may indeed be rationalised by a two times larger Stark tuning rate (**equation (2.67)**).

2.6 Potential-dependence of SEIRA Intensities

In **Figure 25 C, F** and in **Figure 27 D** the linear variation of the SEIRA intensities with the electrode potential for Au and Ag are depicted. A potential change leads to changes in the SEIRA intensity I_{SEIRA} due to the scaling of the surface enhanced IR absorption with $(\cos(\varphi))^2$ (Theoretical Background chap. 1.2.3)

$$I_{SEIRA} = B_s (\cos(\varphi))^2 \quad (4.1)$$

with B_s as a proportionality constant. Therefore, the linear function of the potential-dependent tilt angle φ change is

$$[\cos(\varphi(E))]^2 = [\cos(\varphi_0)]^2 + b(E - E_{pzc,eff}) \quad (4.2)$$

with φ_0 as the tilt angle at $E_{pzc,eff}$ and b (in V^{-1}) a proportionality constant describing the sensitivity of the tilt angle on the potential. Combining **equations (4.1)** and **(4.2)** leads to

$$I_{SEIRA} = B_s [\cos(\varphi_0)]^2 + B_s b (E - E_{pzc,eff}) \quad (4.3)$$

The tilt angles mentioned in the section above all refer to φ_0 . Using these values for linear fits of the intensity vs potential plots B_s and b can be determined. (**Table A 1**)

2.7 Potential-dependence of the Stretching Frequencies

The electrode potential must be related to the local electric field E_F at the nitrile head group to describe the potential-dependent changes of the nitrile stretching frequency for SAMs. Therefore, the tilt angle in **equation (2.67)** will be replaced by the angle φ between $\Delta\vec{\mu}$ and the surface normal. Then the local electric field in this equation can be expressed by **equation (2.63)** to connect the electrode potential to the nitrile stretching frequency

$$\nu = \nu_0 + \cos(\varphi) \times |\Delta\vec{\mu}| \frac{\varepsilon_0 \varepsilon_S \kappa - k}{\varepsilon_0 \left[\frac{\varepsilon_1 \varepsilon_2 \cdot (d_1 + d_2)}{d_1 \varepsilon_2 + d_2 \varepsilon_1} + \varepsilon_S \kappa (d_1 + d_2) \right]} (E - E_{pzc,eff}). \quad (4.4)$$

Considering the potential-dependent of the tilt angle φ as described in **equation (4.2)** gives

$$\nu = \nu_0 + |\Delta\vec{\mu}| \frac{\varepsilon_0 \varepsilon_S \kappa - k}{\varepsilon_0 \left[\frac{\varepsilon_1 \varepsilon_2 \cdot (d_1 + d_2)}{d_1 \varepsilon_2 + d_2 \varepsilon_1} + \varepsilon_S \kappa (d_1 + d_2) \right]} \sqrt{\left[\cos(\varphi_0) \right]^2 + b(E - E_{pzc,eff})} \\ (E - E_{PZC,eff}). \quad (4.5)$$

This equation was used for a fit to the potential-dependent frequency changes. Note that **equation (4.5)** is only defined for $(\cos(\varphi_0))^2 \geq b(E - E_{pzc,eff})$, what is fulfilled in the entire potential range in this work. k describes the assumed linear potential-dependent behaviour of the charge density at the OHP of the SAM/solution interface. The parameters used for the fit and the obtained values for k are summarized in **Table A 1**. **Equation (4.5)** provides a very good description for the potential-dependent frequency changes of C5CN and C6CN on Au. (**Figure 25 B, E**) Although the values for Ag scatter more strongly, the equation still gives a good description for MBN, C5CN and C6CN on Ag as well. (**Figure 27 C** and **Figure A 6**)

The charge density The values obtained for the charge density σ_0 can be used to determine the charge density per monomer in the OHP at the $E_{pzc,eff}$. Therefore, using the monomer-monomer distance of 5 Å (derived from MD simulations $1.96 \times 10^{-19} m^2$) the average area occupied by one monomer can be estimated and values of 0.028 and 0.099 elementary charge units for C6CN and C5CN on Au can be determined, respectively. These values represent the accumulation of a net positive partial charge at the SAM surface due to the negative partial charge at the nitrile nitrogen atoms. For C5CN the larger charge density (0.0807 Cm^{-2}) at $E_{pzc,eff}$ is found and associated with a more homogenous orientation of the CN head group distribution, which probably leads to a stronger net dipole of the SAM head groups.

4. Results and Discussion

Consequently, ions and oriented water dipoles undergo a much more pronounced attraction. For the C6CN SAM (0.0228 Cm^{-2}) the large distribution of inclinations angles may lead to a partial cancelling of the individual CN dipoles resulting in weaker attractions for ions and more randomly oriented water dipoles. The SAM may appear generally more hydrophobic. This is in line with the assumption that $E_{pzc,eff}$ for C6CN is lower by -0.1 V than that of C5CN. The more hydrophobic SAM surface shifts the $E_{pzc,eff}$ even more towards methyl-terminated SAMs as it would be expected for the different chain lengths of C5 and C6.¹¹² Interestingly, for C5CN and C6CN on Ag similar charge densities at $E_{pzc,eff}$ were determined as for Au. Values of 0.1 Cm^{-2} and 0.04 Cm^{-2} for C5CN and C6CN were obtained, respectively. This suggests that also on Ag the C6CN SAM creates a more heterogenous tilt angle distribution and hence has a more hydrophobic character. This may be a general property of C6CN on metal surfaces related to the “even/odd” effects of aliphatic SAMs, which lead to different orientations of the head group. For MBN on Au a charge density at $E_{pzc,eff}$ of 0.206 Cm^{-2} (next chapter) was determined whereas the corresponding value for Ag is only 0.1 Cm^{-2} , similar to the values obtained for C5CN. This would imply a more homogenous tilt angle distribution for MBN SAMs on Au. However, the tilt angles on Au and Ag differ in 40° .

The slope $|k|$ The difference in the slopes of C5CN and C6CN on Au for equation (4.5) agree with the interpretation of the charge densities at $E_{pzc,eff}$ and the larger hydrophobicity of the SAM head group region for C6CN. The slope $|k|$ derived from the electrostatic model represents the local charge sensed by the CN head groups based on its character as a capacitance ($\text{CV}^{-1}\text{m}^{-2}$). The capacitance of the C5CN and C6CN SAMs, neglecting the polar head group, can be estimated as $0.037 \text{ CV}^{-1}\text{m}^{-2}$ and $0.025 \text{ CV}^{-1}\text{m}^{-2}$, respectively.¹¹² However, the capacitance of the head group region for C5CN can be estimated based on the CN group area ($1 \text{ \AA} \times \cos(68^\circ) \approx 0.8 \text{ \AA}$) and the hydrated counter ion layer ($\sim 4 \text{ \AA}$) with $\epsilon_2 = 78$ yielding $C = \epsilon_0 \epsilon_2 d_2^{-1} = 1.44 \text{ CV}^{-1}\text{m}^{-2}$. (**Figure 11**) The slope $|k|$ for C5CN of $1.31 \text{ CV}^{-1}\text{m}^{-2}$ is in good agreement with this value demonstrating the hydrophilicity of the head group region whereas the value for C6CN of $0.35 \text{ CV}^{-1}\text{m}^{-2}$ displays a more hydrophobic character, as already described above. For C5CN and C6CN on Ag a different behaviour is reflected by values of $0.33 \text{ CV}^{-1}\text{m}^{-2}$ and $0.89 \text{ CV}^{-1}\text{m}^{-2}$, respectively. Nevertheless, the fits for these SAMs are not as good as for Au coated surfaces and therefore an interpretation of these data must treat with caution. The slope $|k|$ determined for MBN on both Au ($0.188 \text{ CV}^{-1}\text{m}^{-2}$) and Ag ($0.311 \text{ CV}^{-1}\text{m}^{-2}$) suggests a more hydrophobic head group region, which contrasts with the data obtained for the charge densities σ_0 (*vide supra*). Comparing the present values with values for $|k|$ determined by Schkolnik et al. $|k|$ is in the same range for Au ($0.186 \text{ CV}^{-1}\text{m}^{-2}$) whereas the value for Ag was found to be somewhat smaller ($0.117 \text{ CV}^{-1}\text{m}^{-2}$). Considering the cruder analytical model for the data analysis, the results for $|k|$ from Schkolnik et al. are in reasonable agreement with the present data. Nevertheless, the discrepancy between the interpretations of the charge densities and the capacitances remain such that no unambiguous conclusion concerning the hydrophobicity of the MBN-coated surface is possible.

2.8 The Local Electric Field at the SAM Interface

The goal of this work was to quantify the local electric field at different biomimetic interfaces. The potential-dependent frequency changes measured by SEIRA can be used to determine the relationship between the electrode potential and the local electric field at the SAM/solution

interface. For this purpose, the angle θ in **equation (2.67)** will be substituted by φ and considering the potential-dependent tilt angle changes (**equation (4.2)**) one obtains

$$E_F = - \frac{v - v_0}{|\Delta\vec{\mu}| \cdot \sqrt{(cos\theta_0)^2 + b(E - E_{pzc,eff})}}. \quad (4.6)$$

In **Figure 29** the experimental data (symbols) were compared to the linear relationship between the electric field strength and the electrode potential calculated by the electrostatic model (lines) described with **equation(2.63)**. This model provides a good description for Au/C5CN, Au/C6CN and Ag/MBN whereas for Ag/C5CN and Ag/C6CN the experimental data scatter significantly, most likely due to the distinctly lower quality of the underlying spectroscopic data. **Figure 29** confirms that in a potential range from +0.1 to -0.4 V the sign of the electric field vector is positive for Ag electrodes (pointing away from the electrode) but negative for Au (pointing to the electrode).

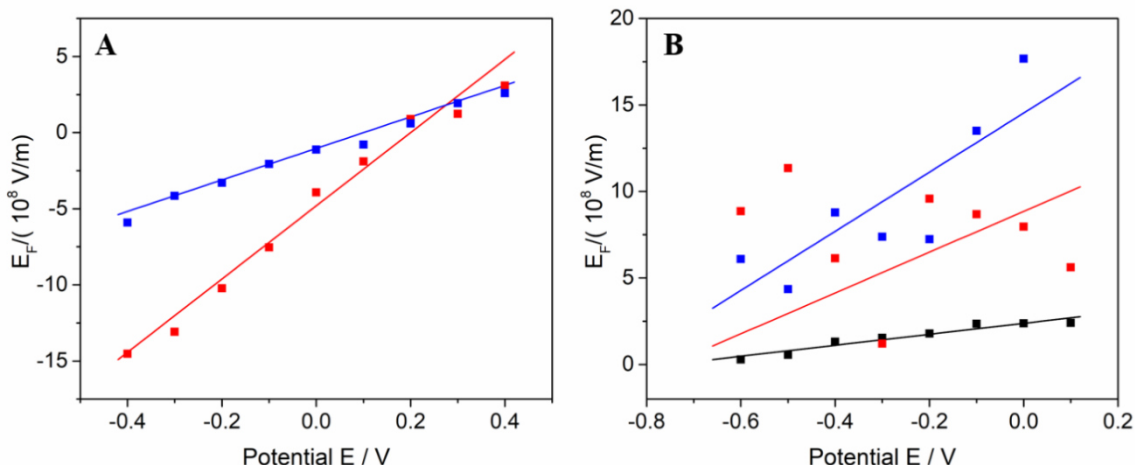


Figure 29: Variations of the local electric field at the SAM/solution interface with the electrode potential for Au (A) and Ag (B) of C5CN (red), C6CN (blue) and MBN (black). The symbols refer to the values directly obtained from the SEIRA frequencies using **equation(4.6)** and the solid lines were determined via **equation(2.63)**.

2.9 Summary

The local electric fields of aromatic and aliphatic SAMs on Au and Ag electrodes could be determined by potential-dependent SEIRA and EIS measurements. The experiments for Au electrodes showed better spectra with intensities higher by a factor of 3 and thus allowed for a more accurate analysis. For Au mainly negative local electric fields in a potential range from 0.4 V to -0.4 V were determined. If $E_F < 0$ the electric field vectors point to the electrode corresponding to a negatively charged surface that attracts positively charged ions. For Ag electrodes, the sign of the electric fields was found to be reversed in the same range of electrode

4. Results and Discussion

potentials. To calculate the electric fields the electrostatic model by Smith and White, later refined by Murgida and Hildebrandt, was extended. Thus, the polar head groups were introduced as a second layer of the SAM and treated separately from the alkyl chain layer. MD simulations of C5CN and C6CN on Au, performed by Dr. Tillmann Utesch, allowed analysing the distribution of the tilt angle and the number of hydrogen bonds. With the obtained physical parameters of the effective potential of zero charge, the charge density and the local capacitance of the CN group the metal/SAM interfaces could be characterized. (**Table A 1**)

3. Labelled Bilayer Membrane with CLSCN

3.1 Results of the IR Measurements

Using a thiocyanate labelled sterol derivate 7-beta-thiocyanocholest-5-en-3-betayacetate (CLSCN) in combination with phospholipids a labelled tBLM system was created.

First, the frequency of the thiocyanate vibration of CLSCN in trichloromethane was determined in IR transmission experiments. (**Figure 31 A**) Then vesicles consisting of POPC, POPG and CLSCN, with a ratio of 5:1:4, was generated and measured in buffer with Bio-ATR. To proof that CLSCN is inside the vesicles also Bio-ATR measurements of POPC/POPG and cholesterol were performed. The difference spectra of the vesicles with and without the Stark reporter group resulting in a positive thiocyanate band. (**Figure A 7**)

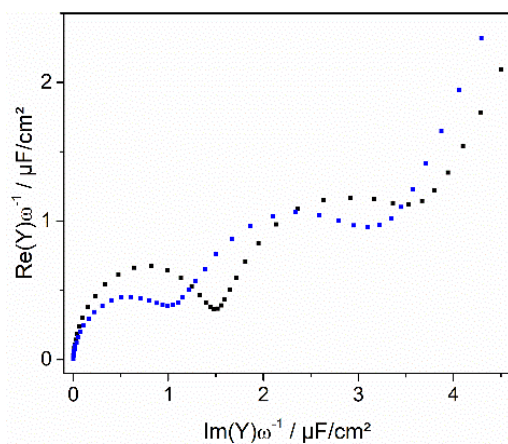


Figure 30: EIS spectra for the mixed WK3SH/6MH (black) and the tBLM with POPC/POPG/CLSCN (blue) with an electrode area of 1.7 cm^2 capacitances of $1.34 \mu\text{F} \times \text{cm}^{-2}$ and $0.88 \mu\text{F} \times \text{cm}^{-2}$ occur, respectively.

At last, the vesicles of POPC/POPG/CLSCN were spread on the WK3SH/6MH membrane and a tBLM was created. The adsorption behaviour of WK3SH with 6MH is in detailed described in Wiebalck, Kozuch et al.¹⁰ A cooperative binding process of the thiol is observed which is characteristic for phase-separated SAMs.¹¹⁶ For a system of 6MH and CPEO3 (Cholesteryl (2-

(2-(2-Mercaptoethoxy)ethoxyethyl)carbamate), which has a similar molecular structure like WK3SH, islands of 200 nm diameter are formed.²⁶ The incubation of the vesicles on the mixed SAM for 2 h and the tBLM in buffer (cyan spectra) is shown in **Figure 31 B**. No significant increasing intensity of the SCN band at 2151 cm^{-1} was detected over the time. To proof the quality of the system, EIS spectra of the mixed SAM and the tBLM were recorded at 0.25 V (near E_{PZC} of the tBLM). (**Figure 30**) Considering a nanostructured Au area of 1.7 cm^2 , the capacitance for the mixed SAM and tBLM are $1.34\text{ }\mu\text{F}\times\text{cm}^{-2}$ and $0.88\text{ }\mu\text{F}\times\text{cm}^{-2}$, respectively. This is in good agreement with reported data from Wiebalck, Kozuch et al. and Forbrig et al. where the capacitance of the tBLM, consisting of pure POPC or a POPC/POPG mix, is reported to be smaller by a factor of ca. 2.^{10,20}

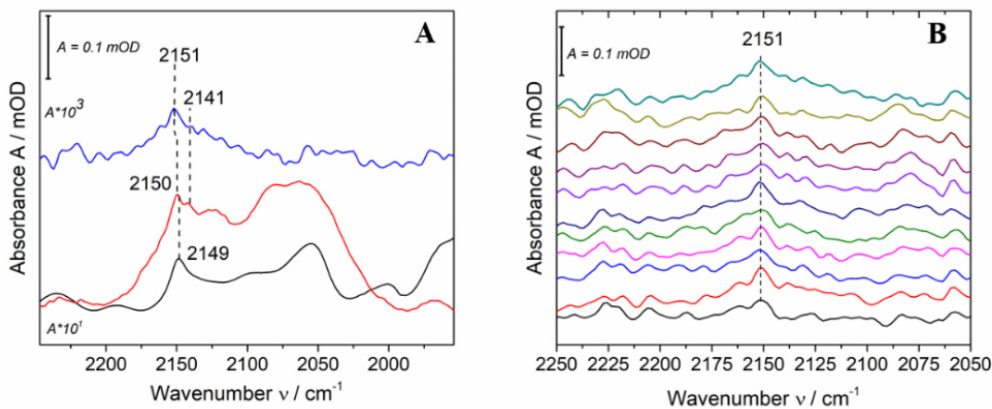


Figure 31: (A) IR difference spectra of CLSCN in trichloromethane against solvent measured with the transmission sandwich cell (black), POPC/POPG/CLSCN vesicles in buffer against buffer detected with the BioATR setup (red) and SEIRA spectra of the tBLM against the Au/WK3SH/6MH system (blue). (B) Incubation of the vesicles on top of the WK3SH/6MH SAM after 3 min. (black), 15 min. (red), 30 min. (blue), 45 min. (magenta), 60 min. (green), 75 min. (dark blue), 90 min. (purple), 105 min. (dark purple), 120 min. (brown), 126 min. (dark yellow) and tBLM after washing with buffer. (cyan).

Potential-dependent SEIRA experiments were performed starting at 0.4 V and decreasing the potential in 0.1 V steps to -0.4 V. After each potential step a reference potential of 0.4 V was applied to proof the reversibility of the system. The potential-dependent changes of the thiocyanate mode of the tBLM system is depicted as well as the second derivative of the absorbance band in **Figure 32 A, B**. The results of the spectra analysis are shown in **Figure 32 C, D**. With decreasing potentials, the SCN band shows a decreasing frequency and intensity. The wavenumber was determined as the centre of gravity of the second derivative. The data reveal a linear potential-dependence for the intensity and a non-linear behaviour for the frequency. The reference potential shows that the data are not completely reversible. (**Figure A 8**) Experiments with the same electrode preparation afforded the same results, revealing the reproducibility to build up a labelled tBLM with CLSCN.

4. Results and Discussion

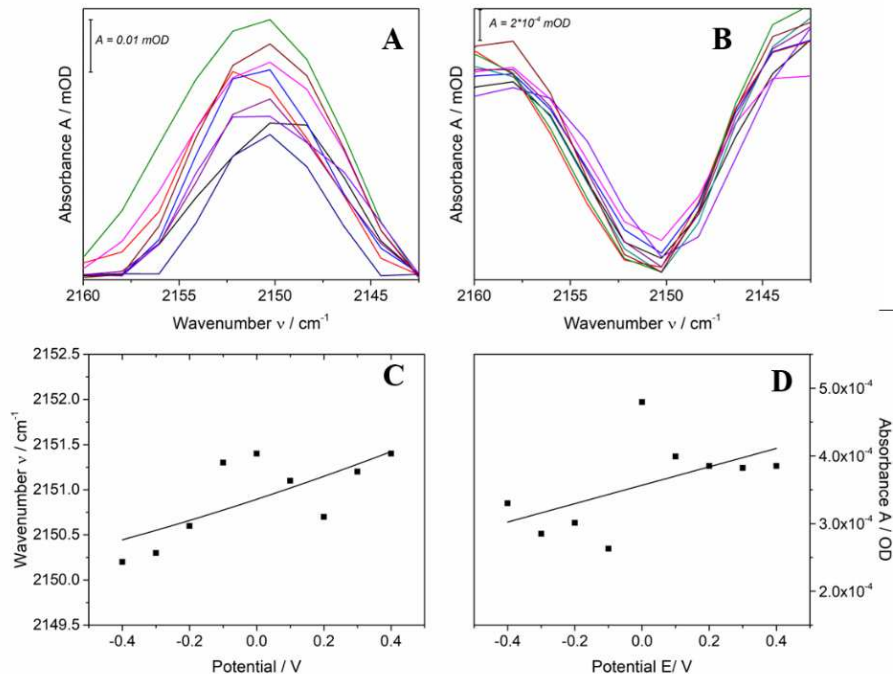


Figure 32: Potential-dependence of the absorption band of thiocyanate (A) and its second derivative (B). 0.4 V (black), 0.3 V (red), 0.2 V (blue), 0.1 V (magenta), 0 V (green), -0.1 V (dark blue), -0.2 V (purple), -0.3 V (dark purple), -0.4 V (brown). The potential-dependent changes of the frequencies (C) and intensities (D) derived from the SEIRA measurements with a non-linear and linear fit.

3.2 Shifts of the Thiocyanate Frequency in different IR Experiments

As discussed in chapter 1.2, the thiocyanate group represents a good Stark reporter group with a Stark tuning rate of $4.8 \times 10^9 \text{ cm}^{-1}/(\text{Vm}^{-1})$. The frequency of MeSCN in trichloromethane (detected in the solvatochromic ATR measurements chap. 1.1) is 2160.1 cm^{-1} and with that it fits into the solvatochromic series previously determined by Deb et al. (2164.3 cm^{-1} in hexane), corresponding to a relatively low electric field provided by the solvent.¹¹⁷ It is thus quite surprising that CLSCN in the same solvent displays a substantial red-shifted (2149 cm^{-1} , $\Delta\tilde{\nu} = 11 \text{ cm}^{-1}$) stretching mode, indicative of a strongly increased electric field. A possible explanation may be that CLSCN forms aggregates such that the SCN group of one CLSCN becomes in close contact with the ester function of second one. However, the solubility of cholesterol in trichloromethane of 1 mg in 4.5 mL is an argument against this explanation. The sterol part of the cholesterol is hydrophobic and a repulsion of the molecules from each other would be expected. An interaction of an ester group with a thiocyanate group has not been described in the literature. Nevertheless, the thiocyanate group of CLSCN in trichloromethane sensed another local electric field than the reporter group of MeSCN in the same solvent. The interactions of CLSCN in trichloromethane and the formation of aggregates is not clear. In POPC/POPG/CLSCN vesicles and in the tBLM system the frequency is slightly higher at 2150 and 2151 cm^{-1} , respectively. In these cases, one may conclude that the label is shielded from contact with the solvent (water). Thus, hydrogen bonding interactions are prevented that would

cause a distinct frequency upshift. The local electric fields are only slightly lower than for the CLSCN in solution such that a similar explanation may hold; the SCN group is in contact with the ester group, near the phospholipid head group region, and the sterol rings and acetyl chain are inside the hydrocarbon interior. Intensity variations of the SCN vibration are due to the different IR methods used for the detection (transmission sandwich cell, Bio-ATR and SEIRA).

3.3 Potential-dependent Changes of the Thiocyanate Vibration

For the SCN vibration in the tBLM system potential-dependent changes of the wavenumber and intensity were detected. (**Figure 32**) The effective potential of zero charge for a tBLM on a nanostructured Au electrode was estimated with potential-dependent EIS of 0.27 V.²⁰ This corresponds to a ν_0 frequency for the SCN group of 2151.24 cm⁻¹ obtained from the fit of the wavenumber vs potential plot from SEIRA experiments in **Figure 32 C**. The tilt angle of CLSCN at $E_{PZC,eff}$ was assumed as 17° based on literature values of the tilt angle with respect to the surface normal of cholesterol in different bilayers determined with MD simulations. (**Table 9**).

The potential-dependent tilt angle changes described for the SAMs also account for CLSCN (**equation (4.2)**). The potential-dependent intensity changes can be fitted with the linear **equation (4.3)** ($I_{SEIRA} = B_s[\cos(\phi)_0]^2 + B_s b(E - E_{pzc,eff})$) leading to a value for b of 0.31 V⁻¹.

Table 9: Tilt angles of cholesterol in different lipid membranes obtained with MD simulations taken from literature.

Composition of lipid bilayer	amount of cholesterol	tilt angle of cholesterol	method	reference
POPC/CL	34 %	17 °	MD	Ferreira et al., 2013 ¹¹⁸
DPPC/CL	11 %	20 °	MD	Smondyrev, Berkowitz, 1999 ¹¹⁹
DPPC/CL	50 %	11°, 12.3 °	MD	Smondyrev, Berkowitz, 1999 ¹¹⁹
DMPC/CL	30 mol %	16.4 °	MD	Sunhwan et al., 2009 ¹²⁰

Compared to the alkyl nitrile SAMs on Au and Ag, this value is greater by a factor of approximately 3. For the MBN SAM on Au and Ag a similar value for b was obtained. In relation to the SAM molecules which are covalently bound to the surface, CLSCN can undergo restricted lateral diffusion within the bilayer. However, the alignment of CLSCN may be influenced by the electric field vector created by the electrode potential. It may be that the potential-induced reorientation of the CLSCN molecules within the tBLM system may eventually lead to the thermodynamically most favourable configuration which cannot be reversed by re-setting the potential to the original value. This explanation can account for the irreversibility of the potential-dependent frequency and intensity changes. Also, the potential-dependent wavenumber changes can be described by **equation (4.5)** (including the potential-

4. Results and Discussion

dependent changes of the tilt angle). Therefore, the distances and dielectric constant must be determined. To reduce the number of a priori unknown parameters (Theoretical Background chap. 3.3) the description of the tBLM system will be simplified using just two layers.

Table 10: Estimated lengths for the several layers of the tBLM on Au.

	d_{C6}^a	d_{OH}^b	$d_{reservoir}^c$	$d_{Head\ group\ 1}^d$	$d_{CH\ bilayer}^e$
distance / m	9.7×10^{-10}	4.8×10^{-10}	1.2×10^{-9}	5×10^{-10}	$\sim 4 \times 10^{-9}$

^a derived from the SAM thickness of C6CN taken from MD simulations minus the nitrile group (the nitrile and hydroxyl group were assumed to have the same size)

^b set equal to the length of the head group and layer of hydrated Na^+ -ions

^c estimated from the 6MH and WK3SH length (C8 + sterol group)

^d taken from Nagle and Tristram-Nagle et al. 2000¹²¹

^e taken from Aittomie et al. 2007¹²²

One layer (d_1, ε_1) contains the mixed SAM, the aqueous reservoir and the lipid head group region on the site of the Au electrode with a dielectric constant of the solution. The second layer (d_2, ε_2) contains the hydrocarbon interior to the lipid head group region at the solution side with a dielectric constant of the membrane interior of $\varepsilon_2 = 2$.¹²³ (**Figure 33**) The total thickness of the first layer d_1 was estimated according to

$$d_1 = d_{C6} + d_{OH} + d_{reservoir} + d_{Head\ group\ 1} = 3.24 * 10^{-9} \text{ m} \quad (4.7)$$

and d_2 was estimated to be

$$d_2 = d_{CH_bilayer} = 4.0 * 10^{-9} \text{ m.} \quad (4.8)$$

Using these values, the electrostatic model described in chap. 2.8 can be applied and for the slope $|k|$ a value of $0.635 \text{ CV}^{-1}\text{m}^{-2}$ was derived. The capacitance at the thiocyanate group in the membrane can be estimated with $\varepsilon_2 = 2$ yielding $C = \varepsilon_0 \varepsilon_2 d_2^{-1} = 4.43 \text{ CV}^{-1}\text{m}^{-2}$ for a totally hydrophobic interior. The value determined by the electrostatic model is greater. This is pointing to a more hydrophilic character of the SCN environment, presumably due to defects caused by ions and water dipoles in the tBLM system.

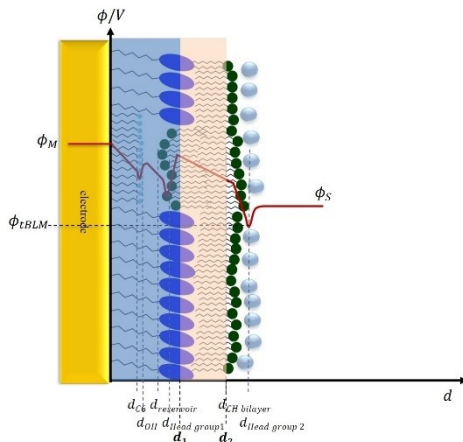


Figure 33: The layers of the tBLM used for the calculations of the local electric fields with the electrostatic model is presented schematically.

3.4 The Local Electric Field in the Bilayer of a tBLM

With the correlation between the electrode potential and the local electric field derived in chapter 2.8 and described by **equation (4.6)** the local electric field at the thiocyanate group within in the membrane can be calculated. This calculation is based on the experimental SEIRA data. With **equation (2.63)** and the abovementioned simplification of the layers the local electric field can be quantified for the developed electrostatic model. The results in **Figure 34** reveal local electric fields from 0 V/m to $-2 \cdot 10^8$ V/m in a potential range from 0.4 V to -0.4 V. The experimental values scatter; however, they can be well described by the fit. Like for the SAMs on Ag, the intensity of the SCN band was quite small and the wavenumber determination was therefore associated with a considerable error. The tBLM system includes defects in the mixed SAM due to the nanostructure of the surface and the phase separation. Performing spectro-electrochemical measurements an average of the changes over the whole surface will be addressed.

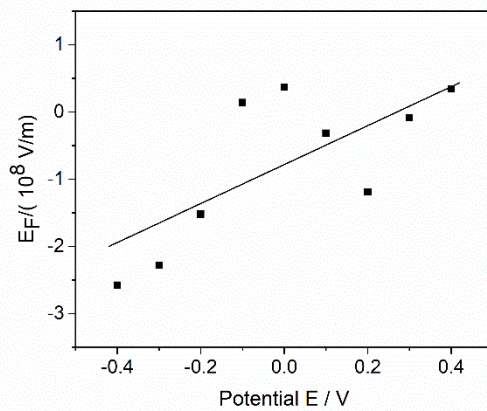


Figure 34: Variations of the local electric field at the SAM/solution interface with the electrode potential for CLSCN inside the bilayer of the tBLM. The symbols refer to the values directly obtained from the SEIRA frequencies using **equation (4.6)** and the solid lines were determined via **equation(2.63)**.

3.5 Summary

In this part of the work the local electric field inside a lipid bilayer was quantified. For this purpose, a thiocyanate-labelled sterol molecule was used. Mixed POPC and POPG vesicles were formed and spread on a phase-separated 6MH/WK3SH monolayer. In a potential range from 0.4 V to -0.4 V mainly negative local electric fields were determined (with the field vector pointing from the solution to the electrode). These electric fields were smaller compared to the SAMs on Au albeit in the same range. The potential-dependent spectral changes of the SCN band were not reversible, due to the restricted mobility of the CLSCN molecules inside the membrane which are eventually trapped in a thermodynamically stable configuration. Nevertheless, thiocyanate was found to be a useful Stark reporter group because of its high sensitivity to changes of the electric field and the symmetric band shape. The interactions of CLSCN in trichloromethane could not be explicit clarified. An aggregation of CLSCN

4. Results and Discussion

molecules cannot be excluded considering the data for vesicles in solution, for the tBLM system and for MeSCN in trichloromethane

4. Determination of the Transmembrane Potential

4.1 Composition of the Mixed Monolayer WK3SH/MBN

Studying the transmembrane potential (TMP) of a tBLM on a nanostructured Au electrode the aqueous solution on both sides of the membrane must be labelled with a Stark reporter group. Therefore, MBN was mixed with WK3SH to create a labelled phase-separated SAM on the nanostructured Au electrode.²⁶ Recently it was shown that a surface coverage of 80 – 90 % of WK3SH leads to an good quality of the tBLM.¹⁰ Whitesides et al. reported that the phase-separation of binary SAM mixtures can be investigated by analysing the ratio of both SAM molecules on the surface as a function of different SAM compositions of both in solution.¹²⁴ Jeuken et al. and Wiebalck, Kozuch et al. showed that this approach can be applied to the capacitance of the SAM from EIS experiments according to^{26,125}

$$x_{\text{WK3SH}} = \frac{C_{\text{WK3SH/MBN}} - C_{\text{WK3SH}}}{C_{\text{MBN}} - C_{\text{WK3SH}}} = \frac{C_{\text{WK3SH/MBN}} - 1.1 \mu\text{Fcm}^{-2}}{4 \mu\text{Fcm}^{-2} - 1.1 \mu\text{Fcm}^{-2}}. \quad (4.9)$$

The specific capacitance of the pure MBN (C_{MBN}) and pure WK3SH (C_{WK3SH}) SAM were determined with EIS experiments at 0.25 V, respectively. (Figure 35)^{10,26} The obtained values are in good agreement with literature.^{10,26}

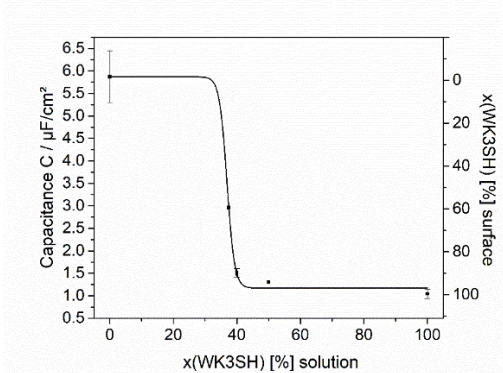


Figure 35: Capacitance values of the mixed WK3SH/MBN SAM as a function of the fraction of WK3SH (x_{WK3SH}) in the propanoic solution of WK3SH and MBN. The ratio of WK3SH on the surface was calculated using equation (4.9). The capacitances were determined from the normalized admittance plots as indicated before. The fit is based on a Boltzmann function:
 $y = A2 + (A1 - A2) / (1 + \exp(x - x0) / dx))$ with $A1 = 5.87 \pm 0.12$, $A2 = 1.17 \pm 0.09$, $x0 = 36.92 \pm 0.2$,

$\text{dx} = 1.19 \pm 0.22$ and $\chi^2 = 0.0017$.

Each point, except for 37.5 % and 59 % WK3SH in solution, results from an average of 3 experiments.

4.2 IR and EIS Measurements of the Labelled tBLM System with MBN and PE-N₃

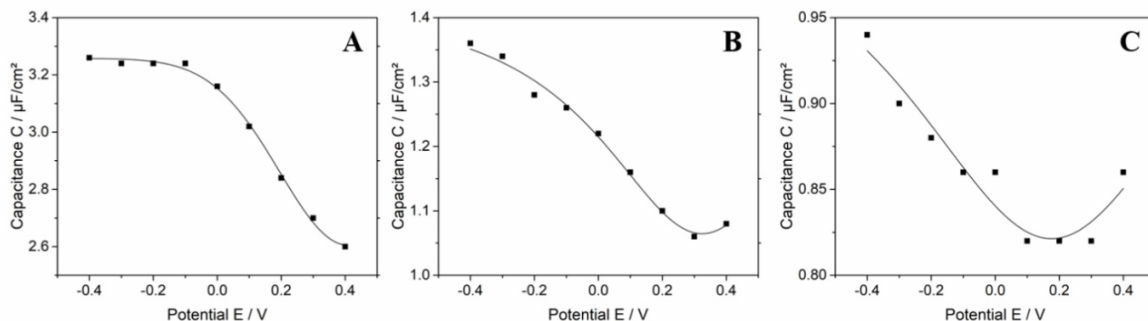


Figure 36: Capacitances determined from the normalized admittance plots of potential-dependent EIS measurements in a potential range from 0.4 V to -0.4 V in 0.1 V steps for MBN/WK3SH (**A**), MBN/tBLM (**B**) and tBLM/PE-N₃ (**C**) with the corresponding Au areas of 1.15 cm^2 , 1.225 cm^2 and 1.675 cm^2 , respectively.

Potential-dependent EIS and SEIRA experiments were performed for different systems to analyse the labelled biomimetic interface: (1) MBN/WK3SH, (2) MBN/WK3SH/POPC (in the following abbreviated to MBN/tBLM), (3) MBN/WK3SH/POPC/PE-N₃ (in the following abbreviated to tBLM/PE-N₃) and (4) WK3SH/POPC/PE-N₃. For the potential-dependent EIS measurements from 0.4 V to -0.4 V in 0.1 V steps it can be observed that the minimum of capacitance for all three tested systems (MBN/WK3SH, MBN/tBLM and tBLM/PE-N₃) were in the positive potential region.

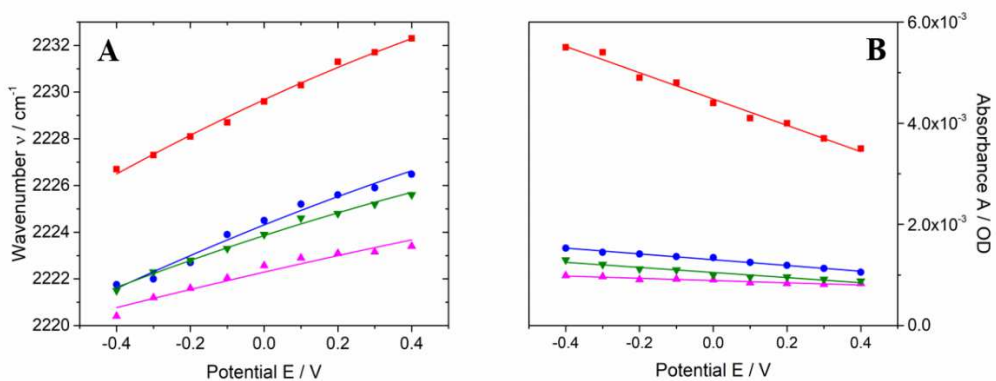


Figure 37: Changes of the wavenumber and intensities of the systems MBN (red), WK3SH/MBN (blue), MBN/tBLM (magenta), tBLM/PE-N₃ (green) between the potentials of 0.4 V to -0.4 V derived from the SEIRA experiments (**Figure 38**). The solid lines represent linear and non-linear fits for the frequencies and wavenumbers, respectively, as described in chap. 2.6 and 2.7.

4. Results and Discussion

Capacitance values were determined from the normalized admittance plots, like previous described, with an area of the Au film of 1.15 cm^2 , 1.225 cm^2 and 1.675 cm^2 for MBN/WK3SH, MBN/tBLM and tBLM/PE-N₃, respectively. For the mixed SAM a minimum capacitance of $1.3\text{ }\mu\text{F/cm}^2$ at 0.4 V was determined. (**Figure 36 A**) Spreading POPC vesicles on the mixed SAM shifted the minimum to 0.3 V at $0.82\text{ }\mu\text{F/cm}^2$ (**Figure 36 B**). Using vesicles with PE-N₃ and POPC, with a ratio of 2:3, $0.82\text{ }\mu\text{F/cm}^2$ at 0.2 V (**Figure 36 C**) is reached at the smallest capacitance. The trend of the capacitance was the same in all experiments, but the values of the capacitance changed because it strongly depends on the quality of the SAM and Au-film.

In potential-dependent SEIRA measurements, wavenumber and intensity changes of the C≡N absorbance band could be observed depicted in **Figure 38** for the systems MBN (**A**) MBN/WK3SH (**B**), MBN/tBLM (**C**) and tBLM/PE-N₃ (**D**). A decrease in potential leads to an increase in intensity for all systems. For the pure MBN SAM the highest intensity was detected with 5.5 mOD for -0.4 V whereas for the other systems intensities of 1.53 mOD (**B**), 0.98 mOD (**C**) and 1.3 mOD (**D**) at -0.4 V were determined. A red-shift was detectable for all systems with a decrease in potential. Thereby, the pure MBN revealed the strongest shift (5.6 cm^{-1}) from 2231.3 cm^{-1} (0.4 V) to 2226.7 cm^{-1} (-0.4 V).

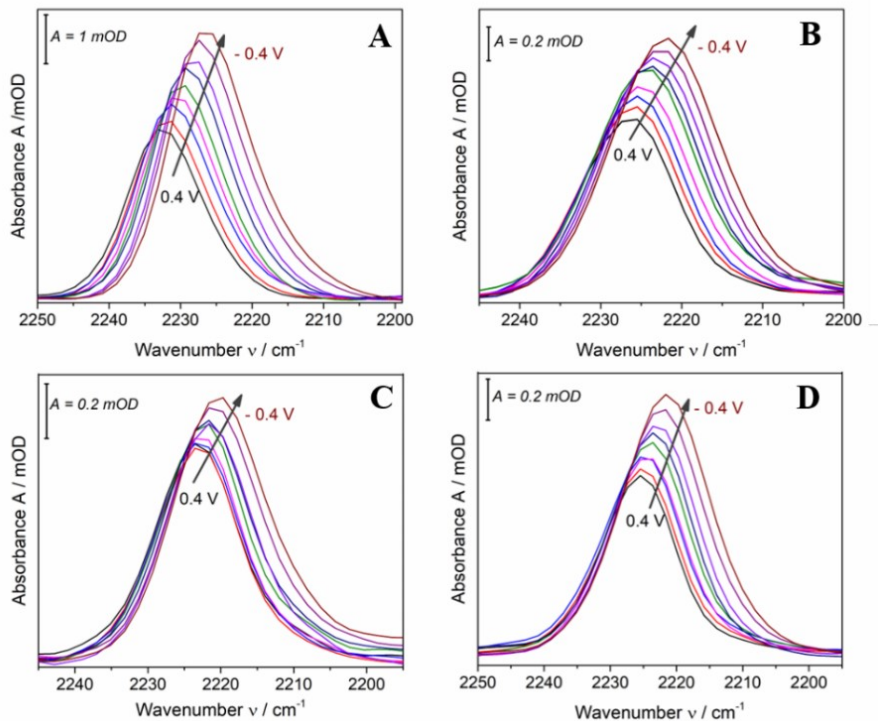


Figure 38: Potential-dependent MBN absorbance band of different systems: MBN (**A**), MBN/WK3SH (**B**), MBN/tBLM (**C**), tBLM/PE-N₃ (**D**) with 0.4 V (black), 0.3 V (red), 0.2 V (blue), 0.1 V (magenta), 0 V (green), -0.1 V (dark blue), -0.2 V (purple), -0.3 V (dark purple), -0.4 V (brown). The arrow marks the direction of the frequency and intensity change of each band.

Interestingly, the frequency of the C≡N vibration at 0.4 V of the mixed SAM system (2226.48 cm⁻¹) was close to the frequency of -0.4 V of pure MBN. Furthermore, the wavenumbers of the mixed SAM, MBN/tBLM and the tBLM with MBN and PE-N₃ are in the same range and the frequencies of the mixed SAM and tBLM/PE-N₃ were nearly the same for negative potentials. (**Figure 37**) The C≡N absorbance band shifted about 4.1 cm⁻¹ and 0.98 cm⁻¹ for the tBLM/PE-N₃ system and mixed SAM with pure POPC, respectively. The potential-dependent wavenumber and intensity changes are shown in **Figure 37** and can be described with a non-linear fit for the frequencies and linear fit for the intensities.

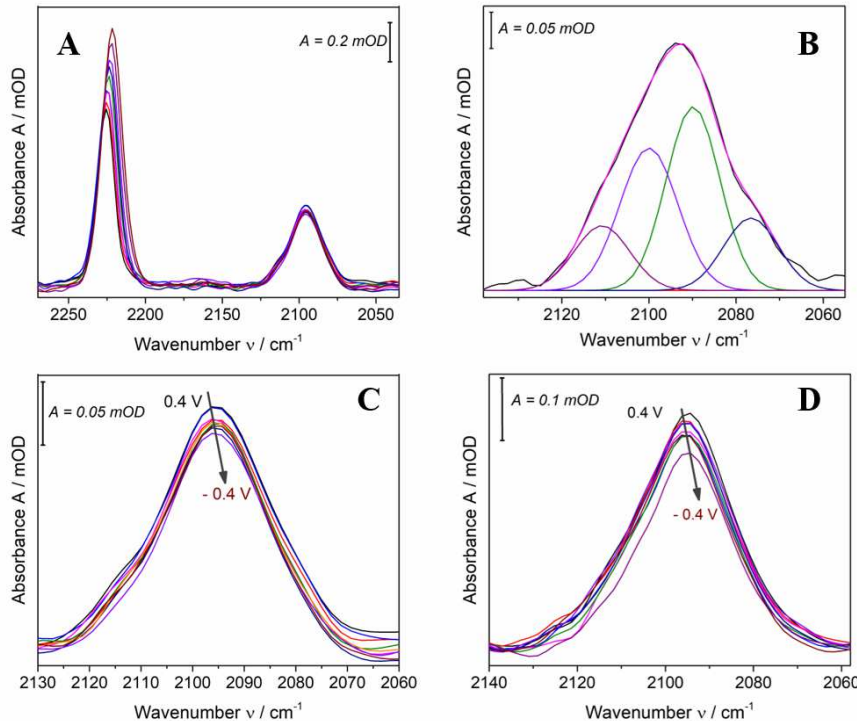


Figure 39: The SEIRA potential-dependent absorbance bands of MBN (C≡N) and PE-N₃ (N₃) are shown in **(A)** for the tBLM/PE-N₃ system. In **(B)** the fit with four Gaussian bands for the N₃-vibration at -0.4 V is presented. The potential-dependent SEIRA absorbance band of N₃ for the systems tBLM/PE-N₃ **(C)** and WK3SH/POPC/PE-N₃ **(D)** is depicted. The potential-dependent measurements are marked by traces of different colour, i.e. 0.4 V (black), 0.3 V (red), 0.2 V (blue), 0.1 V (magenta), 0 V (green), -0.1 V (dark blue), -0.2 V (purple), -0.3 V (dark purple), -0.4 V (brown).

In addition to the nitrile vibration of MBN, the azide vibration of the labelled PE-N₃ lipid could be detected simultaneously. The results of the potential-dependent SEIRA measurements are shown in **Figure 39**. In **(A)** the intensity of the N₃ vibration is much smaller by a factor of 2.7 for -0.4 V than for the C≡N vibration.

A red-shift with decreasing potential was found for the tBLM/PE-N₃ system whereas the frequency hardly changed for WK3SH/POPC/PE-N₃ in a potential range from 0.4 V to -0.4 V. The azide vibration exhibits an asymmetric band shape. Therefore, four Gaussian bands were used for a fit to the absorbance band. To analyse the potential-dependent changes, the shifts of the Gaussian band around 2094 cm⁻¹ (green Gaussian band in **Figure 39 B**) was used because

4. Results and Discussion

the other components show a weaker dependence on the potential (discussed in Appendix A 7). **Figure 40** represents the frequency and intensity potential-dependent changes of the N₃ vibration with a linear and non-linear fit, respectively.

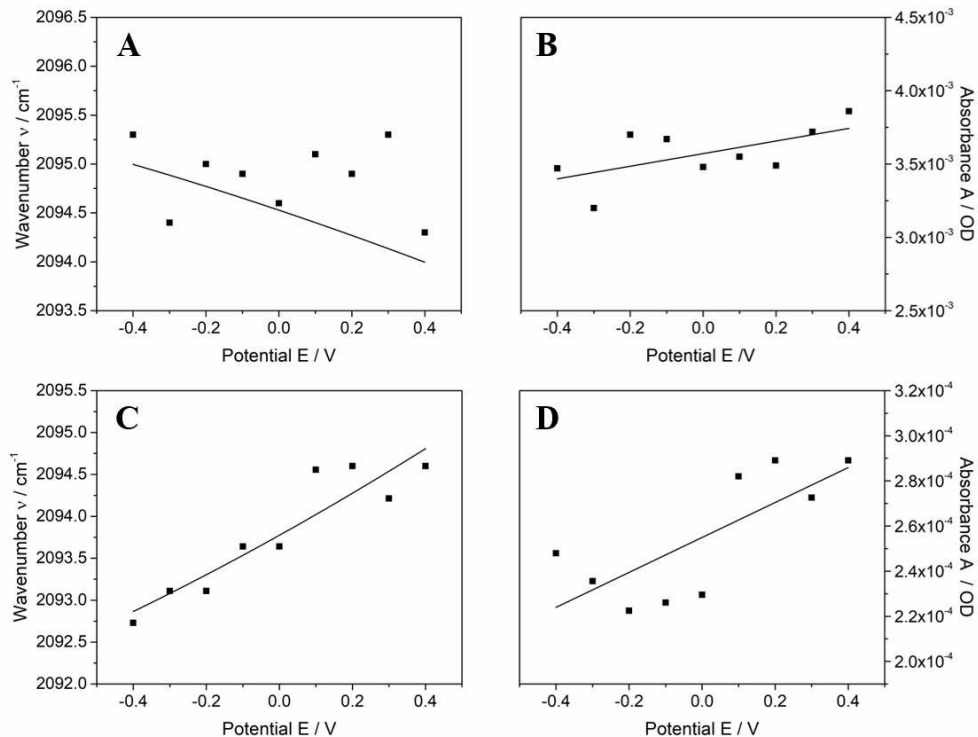


Figure 40: Potential-dependent changes of the frequency and intensity of the azide stretching determined from SEIRA measurements (**Figure 39 C, D**) for the system WK3SH/POPC/PE-N₃ (**A, B**) and tBLM/PE-N₃ (**C, D**) with a non-linear and linear fit for the wavenumber and intensity changes, respectively.

4.3 Analysis of the Mixed SAM Formation

The formation of a phase-separated 6MH/WK3SH SAM was described in detail by Wiebalck and Kozuch et al.¹⁰ For the tBLM formation it is necessary to have a polar head group for the short SAM, 6MH was exchanged by MBN for our system. Only a few solution ratios were prepared to form the optimal SAM ratio on the surface with approximately 80 % WK3SH. By fitting the MBN/WK3SH ratios in solution against the ratios on the surface (or the capacitance of the mixed SAM) a sigmoidal shape is reached. This indicates a cooperative binding process of the thiols, also observed for 6MH/WK3SH and is characteristic for phase separated SAMs.¹¹⁶ 6MH islands of 200 nm diameters on Au were created by the mixture with CPEO3.²⁶ For the new system a phase-separated SAM on the surface can be assumed based on a similar formation behaviour of MBN/WK3SH to 6MH/WK3SH.

4.4 The Effective Potential of Zero Charge for the tBLM

Analysing the potential-dependent EIS measurements, interfacial capacitances for the different systems can be derived (**Figure 36**). The potential of minimum capacitance corresponds to the effective potential of zero charge of the system,¹¹⁰ leading to $E_{PZC,eff}$ values for MBN/WK3SH of 0.4 V, for MBN/tBLM of 0.3 V, and for tBLM/PE-N₃ of 0.2 V. This decreasing effective potential of zero charge for the tBLM compared to the mixed SAM is due to increasing amount of charges for the bilayer system. When adding PE-N₃ to POPC the tBLM contains even more charges leading to a further decrease of $E_{PZC,eff}$ for the labelled tBLM system.

4.5 The Potential-dependent Frequency and Intensity Changes of C≡N

Using MBN as a Stark reporter group the electrostatic changes of the water reservoir can be quantified when building up a tBLM. Therefore, the potential-dependent frequency and intensity changes represented in **Figure 37** must be analysed to obtain the electrostatics. The thickness of the water reservoir was estimated to be 1.2 nm, which corresponds more to a layer of water dipoles rather than to an aqueous bulk phase. The thickness of the MBN head group with a hydrated counter ion layer was assumed of 0.48 nm (taken from the data obtained for C5CN and C6CN in chap. 2.7). Since the water layer is so small, changes can be directly detected by the nearby nitrile reporter groups.

Potential-dependent intensity changes The potential-dependent tilt angle changes of MBN can be described with **equation (4.2)**. **Equation (4.3)** is used to fit the data derived from the SEIRA experiments in **Figure 37 B**. For the tilt angles at the effective potential of zero charge for Au/MBN 40° were assumed⁴⁵ The tilt angles for the other three systems were derived from the fits (**equation (4.3)**), using an initial value of 40° that results in a tilt angle φ_0 for the mixed SAM and of 37° and 39° for both tBLM systems. The values obtained for b , the sensitivity of the tilt angle to potential changes, were determined to be -0.45 V⁻¹, -0.35 V⁻¹, -0.16 V⁻¹ and -0.32 V⁻¹ for MBN, MBN/WK3SH, MBN/tBLM and tBLM/PE-N₃, respectively. All the values are negative, thus, with increasing potential the intensity decreases. For the pure MBN monolayer the greatest tilt of the CN group was determined presumably caused by the lack of other molecules and the resultant higher mobility of the head group. The value is greater than those for C5CN and C6CN on Au. In **Figure 41 B** the tilt angles of the CN group in the different systems are shown, calculated after rearranging **equation (4.1)** to

$$\cos(\varphi) = \sqrt{\frac{I_{SEIRA}}{B_s}} \quad (4.10)$$

In **Figure 41 A** the potential-dependent changes of the cosine of the tilt angle are described by fits of **equation (4.2)**. For the mixed SAM the tilting of the CN group is somewhat more restricted compared to the pure MBN. The large WK3SH molecules co-adsorbed on the Au film may limit the MBN molecules from their free movement in the contact regions between the two SAM islands. Adding POPC vesicles to the mixed SAM and creating a tBLM attenuates the potential-dependent changes of the tilt angle. The water reservoir is formed but due to its small

4. Results and Discussion

size the SAM surface may also interact with the lipid surface and noncovalent interactions influence the tilt. Surprisingly, the CN group tilt more when adding PE-N₃ to the POPC lipids. These values are similar as for the mixed SAM. Thus, the addition of PE-N₃ may lead to a somewhat taller water reservoir due to the bulkier head group of PE-N₃.

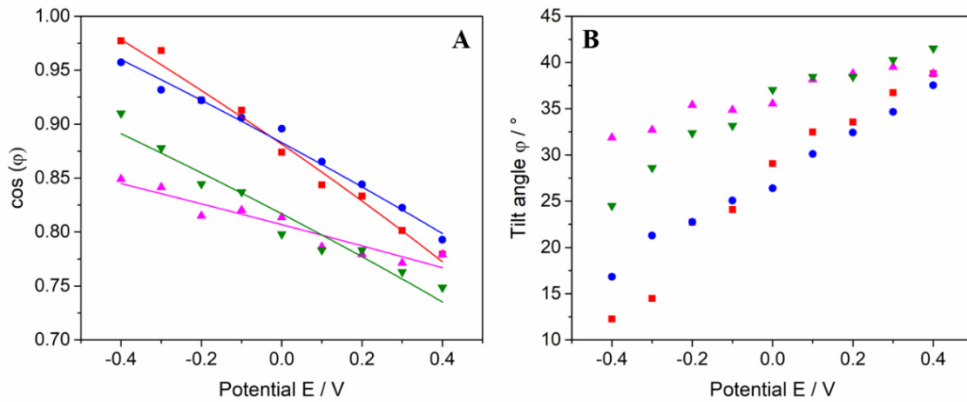


Figure 41: Potential-dependent C≡N tilt angle changes for MBN. In (A) the cosine of the tilt angle is calculated by **equation (4.10)** and fitted with **equation (4.2)**, in (B) the tilt angles φ calculated from $\cos(\varphi)$ are represented for MBN (red), WK3SH/MBN (blue), MBN/tBLM (magenta), tBLM/PE-N₃ (green).

Potential-dependent frequency changes The electrostatic model developed in ‘Theoretical Background chap. 3.3’ can be applied to the Au surface structured with MBN or the mixed SAM. **Equation (4.5)** can be fitted to the potential-dependent frequency shifts providing a good description of the data shown in **Figure 37**. Therefore, the effective potentials of zero charge obtained in chap. 4.4 were used as well as a value for pure MBN taken from Schkolnik et al. of 0.422 V.¹⁰⁹ The distance of MBN without the head group was taken from Schkolnik et al., minus the nitrile group (5.6×10^{-10} m and $\varepsilon_1 = 2.3$). For the head group region the length of the nitrile group plus a layer of hydrated Na⁺ ions was assumed.^{56,57} Here, the value was also taken from the C5CN monolayer head group region (4.8×10^{-10} m) and the dielectric constant of this region was set equal to that of the solution (*vide supra*). The Stark tuning rate of the CN group of MBN was assumed to be $6.0 \times 10^{-9} \text{ cm}^{-1}/(\text{Vm}^{-1})$ (chap. 2.5).¹⁰⁹

Thus, with all these parameters the fit to the potential-dependent frequency changes (**equation (4.5)**) of all systems including MBN led to values for $|k|$ and for the charge density at the effective potential of zero charge. The local capacitance of the head group region for MBN is the same as for C5CN (1.44 C/(Vm⁻¹)) indicative of a high polarity. Just comparing the wavenumbers of pure MBN and MBN/WK3SH, a downshift can be observed by about approximately 5 cm⁻¹. The effect obtained for hydrogen bonding interactions between the nitrile group and water dipoles was found to cause an upshift of up to ca. 7.6 cm⁻¹ for the fully solvent exposed label. This implies that the MBN phases in the mixed SAM are shielded by WK3SH to reduce hydrogen bond contacts and/or the island structure of the MBN-SAMs corresponds to a higher local electric field. Presumably, the smaller extent of hydrogen bonding interactions is the prevailing effect since the $|k|$ values for MBN of 0.188 C/(Vm⁻¹) and MBN/WK3SH of

0.12 C/(Vm⁻¹) are significantly larger than those obtained for the local capacitance at high polarity. Since, no MD simulations were performed for MBN containing SAMs, it is hard to quantify if this deviation is due to a heterogeneous tilt angle distribution and therefore a more heterogeneous SAM structure on the surface. For the tBLM with pure POPC $|k|$ was estimated to be 1.21 C/(Vm⁻¹) and with mixed lipids 0.056 C/(Vm⁻¹). Surprisingly, the head group region gets a more hydrophilic character by adding POPC lipids and a less hydrophilic character by adding mixed lipid compared to the mixed SAM. For the MBN/tBLM system the wavenumbers of the nitrile group are shifted about 7.5 cm⁻¹ in comparison to the pure MBN, the same amount quantified for the hydrogen bond effect. Since, the water layer between the CN group and the lipids is quite small such that hydrogen bond formation with water molecules is even more restricted. Hence, the values for $|k|$ must be treated with caution for the tBLM system. The values obtained for σ_0 are 0.206 Cm⁻², 0.228 Cm⁻², 0.137 Cm⁻², and 0.079 Cm⁻² for MBN, MBN/WK3SH, MBN/tBLM and tBLM/PE-N₃. The charge density is the highest for the mixed SAM. Thus, ions and water dipoles get strongly attracted. The value for pure MBN is in a similar region. However, after generation of the tBLM the charge density is decreased by a factor of 1.7 compared to the mixed SAM and even lower for mixed lipids (by a factor of 2.9). Thus, the MBN molecules get shielded from the solution by the bilayer and less ions and water dipoles get attracted. All values obtained with the electrostatic model are summarized in **Table A 1.**

4.6 The Potential-dependent Frequency and Intensity Changes of N₃

The tBLM system was not only labelled by MBN but also by using PE-N₃ to quantify the local electric fields in the bulk solutions near the lipid head group region. The frequency shift of the azide vibration was quite small but this was expected taking the solvatochromic measurements into account. The intensity changes were also quite small. To apply the electrostatic model to the two systems with PE-N₃, one with MBN and one without, the distances (d_1, d_2) of the corresponding layers must be determined. For the system without MBN the WK3SH SAM and lipid interior can be summarized as layer1 with $d_1 = 6.7 \times 10^{-9}$ m (detailed list of the different distances is in chap. 3.3 **Table 9**) and $\epsilon_1 = 2$ because of the hydrocarbons in the bilayer. For the second layer the lipid head group region with a layer of ions, $d_2 = 4.8 \times 10^{-10}$ m is estimated and ϵ_2 set equal to the value of the solution.¹²³ The Stark tuning-rate of N₃ was determined as 2×10^{-9} cm⁻¹/(Vm⁻²) in chap. 1.3. The potential-dependent intensity changes are shown in **Figure 40** and were used to determine the tilt angle at $E_{PZC,eff}$ with an initial value for POPC, taken from literature, of 20°.¹²⁶ A fit of **equation (4.3)** yielded a tilt angle at $E_{PZC,eff}$ of 18° and a value for b of 0.107 V⁻¹. The absorbance band shows a small amount of intensity changes also reflected by the small value for b . For the system with MBN, d_1 was changed to 2.7×10^{-9} m (addition of MBN and the water layer) and d_2 , as the thickness of the lipid head group region, was kept the same value. The dielectric constants were changed to $\epsilon_1=78$ and $\epsilon_2=2$. The fit to the data results in $b = 0.26$ V⁻¹.

For the potential-dependent frequency changes **equation (4.5)** was used to fit the data. The value for the local charge $|k|$ sensed by N₃ is about 5.1 C/(Vm⁻²) in presence of MBN and 4.9 C/(Vm⁻²) in absence of MBN. For a high polarity, values of 1.4 C/(Vm⁻²) were expected. This may be taken as an indication that the simplifications of the model associated with the restriction to two layers is too severe and thus may also afford physically meaningless values for individual parameters. This has also consequences for calculating the electric fields which must

4. Results and Discussion

be considered with caution. Another reason for the limited applicability of this model roots in the weak potential-dependent frequency and intensity changes of N₃ used as experimental data input.

4.7 Electrostatics at Different MBN Containing Biomimetic Interfaces

The local electric field at the CN group can be calculated using the experimental values from SEIRA spectroscopy as discussed in the previous sections (**Figure 42**). The electrostatic model provides a good description of the corresponding experimental data. It also applies for PE-N₃, although the accuracy of the experimental data must consider with caution. Note that the azide group is separated from the Au surface by ca. 7 nm ($\sim d_1 + d_2$). Thus, the weak signals of the azide groups can be rationalised in view of the distance-dependent attenuation of the surface enhancement (Theoretical Background chap.1.2.3).

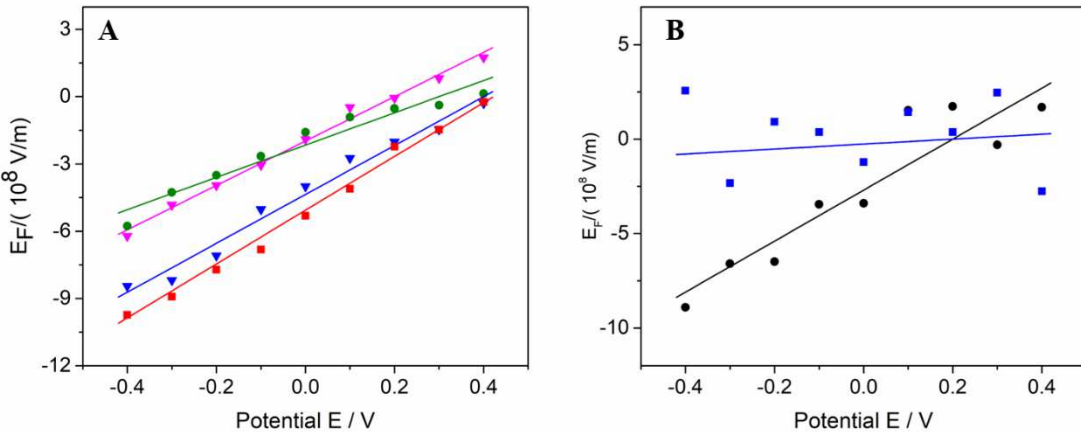


Figure 42: Potential-dependent variations of the local electric field at the SAM/solution interface for MBN (A) and in the solution, near the head group region, for PE-N₃ (B) with the electrode potential. The symbols refer to the values directly obtained from the SEIRA frequencies using **equation (4.6)** and the solid lines were determined via **equation (2.63)**. The different systems in (A) refer to MBN (red), MBN/WK3SH (blue), MBN/tBLM (green) and tBLM/PE-N₃ (magenta). In (B) the data for tBLM/PE-N₃ (black) and WK3SH/POPC/PE-N₃ (blue) is represented.

For the calculation of the transmembrane potential the potential in the water layer and in the bulk solution must be considered. For this purpose, the system is divided into two layers: (1) the short SAM plus the water layer (d_1) and (2) the lipid bilayer and the adsorbed ions on the interface (d_2). These layers are treated separately according to the model developed by Smith and White.⁵⁵ The charge density at the metal can be described with **equation (2.51)** by substituting $\varepsilon_0 \varepsilon_1 d_1^{-1}$ by K_1 :

$$\sigma_M = \frac{\varepsilon_0 \varepsilon_1}{d_1} (\phi_M - \phi_1) = K_1 (\phi_M - \phi_1). \quad (4.11)$$

The charge density at the first layer is:

$$\sigma_M + \sigma_1 = \frac{\varepsilon_0 \varepsilon_2}{d_2} (\phi_1 - \phi_2) = K_2 (\phi_1 - \phi_2). \quad (4.12)$$

And the charge density in solution is:

$$\sigma_S = -\varepsilon_0 \varepsilon_S \kappa (\phi_2 - \phi_S) = -K_3 (\phi_2 - \phi_S). \quad (4.13)$$

The potential difference $\phi_2 - \phi_1$ corresponds to the transmembrane potential ΔE_{TMP} . The potential difference $\phi_M - \phi_S$ refers to the difference of the applied electrode potential and the potential of zero charge of Au $E - E_{PZC}$.

The change of the charge density over the biomimetic interface expressed with **equation (4.11)** and **(4.13)** leads to:

$$\frac{\sigma_M}{K_1} - \frac{\sigma_S}{K_3} = \phi_M - \phi_S + \phi_2 - \phi_1 = E - E_{PZC} + \Delta E_{TMP}. \quad (4.14)$$

Based on the charge neutrality of the complete system

$$\sigma_M + \sigma_1 + \sigma_S = 0. \quad (4.15)$$

equation (4.12) can be rearranged to

$$\sigma_S = K_2 \Delta E_{TMP}. \quad (4.16)$$

Finally, by insertion of **equation (4.16)** in **(4.14)**, a relation between the transmembrane potential ΔE_{TMP} and the applied electrode potential E is obtained:

$$\Delta E_{TMP} = \frac{\sigma_M \frac{K_3}{K_1} - K_3 (E - E_{PZC})}{K_3 + K_2}. \quad (4.17)$$

As an assumption the charge density of first layer in **equation (4.11)** can be described by the local electric field of the MBN head group region $E_{F,MBN}$

$$\sigma_M = \frac{\varepsilon_0 \varepsilon_1}{d_1} (\phi_M - \phi_1) = \varepsilon_0 \varepsilon_1 E_{F,MBN}. \quad (4.18)$$

4. Results and Discussion

This assumption is associated with a significant error because of the two-layer model. The first layer includes the short SAM and the whole water layer. In **equation (4.18)** d_1 is approximated by d_{MBN} , although d_{MBN} corresponds to the MBN head group region of 4.8×10^{-10} m, which is about 5 times smaller than d_1 . Substituting the charge density of the metal in **equation (4.17)** leads to:

$$\begin{aligned}\Delta E_{TMP} &= \frac{\varepsilon_S \kappa d_2}{\varepsilon_2 + \varepsilon_S \kappa d_2} (E_{F,MBN} d_1 - (E - E_{PZC})) \\ &\approx 2.28 * 10^{-9} m * E_{F,MBN} - 0.99E + 0.059 V\end{aligned}\quad (4.19)$$

Using this potential-dependent description with the determined electric fields for the MBN head group with **equation (4.6)** the transmembrane potential can be calculated as shown in **Figure 43**. The dielectric constant ε_2 of the membrane interior was set to $\varepsilon_2 = 2$ and d_2 to the hydrocarbon interior and lipid head group interface to 4.5×10^{-9} m.

This analysis may be considered as a crude approximation. In addition to the abovementioned error associated with the assumption that $d_1 = d_{MBN}$, the dielectrics within the two layers are certainly not homogeneous as suggested by using a single dielectric constant in each case.

Using the potential-dependent values for the electric field of the MBN head group region $E_{F,MBN}$ to calculate the transmembrane potential with **equation (4.19)**, one obtains a the transmembrane potential of -0.15 V at the effective potential of zero charge (0.3 V) (**Figure 22**). Note that the transmembrane potential was described as the potential difference of the bulk solution at the tBLM minus the potential in the water reservoir. Here the negative value of the transmembrane potential shows that the potential in the water reservoir is more positive than the potential in the bulk solution in the case for the effective potential of zero charge. Therefore, the electric field over the lipid bilayer is directed from the electrode to the solution. Forbrig et al estimated the potential E_0 , which refers to the transmembrane potential of zero, be in a range between 0.14 V to 0.33 V.²⁰ Using **equation (4.19)** to calculate the potential E_0 with $E_{F,MBN} = 0$ V leads to 0.15 V and hence is in the expected potential range. However, values of the transmembrane potential for more negative potentials are very high. Thus, it appears to be that the present crude model may provide a satisfactory description for the transmembrane potential only in the region of effective potential of zero charge.

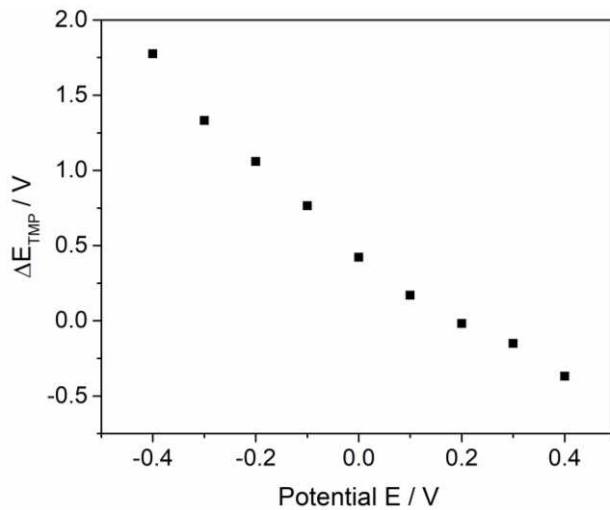


Figure 43: Potential-dependent transmembrane potential ΔE_{TMP} for the tBLM system calculated with equation (4.19).

4.8 Summary

In this part the assembly of the tBLM system on nanostructured Au was electrostatically analysed. The focus of the studies was laid on the water reservoir. Simple geometric considerations indicate that the inner water reservoir consists of several water layers which, however, do certainly not display the same properties as a bulk water phase. This is reflected by the frequencies of the C≡N vibration of the MBN SAM which suggest a more hydrophobic character of the SAM surface (less H-bonds) in the presence of a bilayer on top. Analysing the C≡N vibration of MBN in the different systems it could be determined that the addition of a second SAM and lipids restrict the MBN molecules in their potential-dependent changes which may be due to steric limitations and noncovalent interactions. Besides, the azide vibration shows only a weak potential-dependence of frequencies and intensities such that it was not possible to evaluate the potential and local electric field at the membrane/solution interface. However, with the assumption of two separated layers within the tBLM system a satisfactory estimation of the transmembrane potential near the effective potential of zero charge was possible.

5. Conclusion and Outlook

Stark-Reporter Groups In this work, the cyanide, thiocyanate, and azide group were analysed with respect to their quality as a local electric field reporter. There are different ways to determine Stark tuning rates. In this project, solvatochromic ATR and DFT experiments were applied and led to values of $4.8 \times 10^{-9} \text{ cm}^{-1}/(\text{Vm}^{-1})$ for cyanide, $3.2 \times 10^{-9} \text{ cm}^{-1}/(\text{Vm}^{-1})$ for thiocyanate and $2 \times 10^{-9} \text{ cm}^{-1}/(\text{Vm}^{-1})$ for the azide group. For the CN and SCN group, interactions with sulphur in DMSO influenced the frequency of the vibration.

The metal/SAM interface The local electric fields of nitrile-functionalized nanostructured Au and Ag surfaces were determined successfully. Aliphatic (C5CN, C6CN) or aromatic (MBN) SAMs on metal electrodes were analysed with spectro-electrochemical measurements, which were performed in a potential range from 0.4 V to -0.4 V and from 0.1 V to -0.6 V for Au and Ag, respectively. Thereby potential-dependent frequency and intensity changes of the C≡N stretching vibration led to the quantification of local electric fields using the vibrational Stark effect. (**Table 11**) The electrostatic model introduced by Smith and White, later refined by Murgida and Hildebrandt, was revised by a more detailed consideration of the SAM. The hydrophobic alkyl chain and the polar head group were treated separately, leading to a very good description of the electrostatics at the metal/SAM interface and a relation of the applied potential with the local electric field in the head group region. With the obtained physical parameters of the effective potential of zero charge, the charge density and the local capacitance of the CN group the metal/SAM interfaces could be characterized.

Table 11: Calculated potential-dependent local electric fields at the CN head group of various nitrile-functionalized nanostructured Au and Ag surfaces.

Au	C5CN E_F / Vm^{-1}	C6CN E_F / Vm^{-1}	Ag	C5CN E_F / Vm^{-1}	C6CN E_F / Vm^{-1}	MBN E_F / Vm^{-1}
0.4 V	3×10^8	2.6×10^8	0.1 V	5.6×10^8	17.7×10^8	2.4×10^8
-0.4 V	-14×10^8	-6×10^8	-0.6 V	8.8×10^8	6.1×10^8	2.9×10^8

The experimental observations of the tilt angle and the heterogeneity of the system could additionally be confirmed by MD simulations of C5CN and C6CN on Au. However, a potential-dependent alteration of the Ag-film could not be excluded for that electrode (**Figure A1**)

Construction of labelled tBLMs on Au Solid supported membranes represent more realistic biomimetic interfaces. With a SCN labelled sterol derivative (CLSCN) incorporated in a tBLM system on Au, the local electric field inside the membrane was determined. The successful formation of a labelled tBLM was verified with the capacitance of the tBLM at 0.25 V of $0.88 \mu\text{F} \times \text{cm}^{-2}$, which is in line with literature data and, thus, proves the successful bilayer formation. First IR measurements of pure CLSCN and CLSCN within vesicles in solution were performed and compared to the SCN vibration in the tBLM system. A pronounced shift of the SCN vibration in trichloromethane was found in contrast to MeSCN in the same solvent. Interactions between the thiocyanate and ester group of two different molecules and the formation of aggregates, may linked by solvent molecules, could be assumed. But no clear hints were found how CLSCN interacts in trichloromethane. In vesicles and in the tBLM, the SCN vibration was found in the same frequency range as for CLSCN in trichloromethane. This may be due to similar interactions of the SCN group with the ester groups of POPC or POPG.

Potential-dependent frequency and intensity changes of the SCN vibration were described by a linear relationship, based on the electrostatic model. Therefore, two layers were assumed containing the mixed SAM, the aqueous reservoir and the lipid head group region on the site of the Au electrode in one layer. The second layer contained the hydrocarbon interior and the lipid head group region at the solution side. Hence, local electric fields from $3.4 \times 10^7 \text{ V/m}$ to $-2.6 \times 10^8 \text{ V m}^{-1}$ in a potential range from 0.4 V to -0.4 V were determined for the SCN vibration within the membrane.

A phospholipid labelled with an azide at the head group region (PE-N₃) was also incorporated in the tBLM system leading to a capacitance of the tBLM of $0.82 \mu\text{F/cm}^2$ at 0.2 V. Using this labelled lipid, the local electric field in solution, near the bilayer lipid membrane surface, could be determined. However, the azide group in solution has a distance from the surface about ca. 7 nm. Thus, the weak IR signals of the azide group can be explained with the distance-dependent attenuation of the surface enhancement. Furthermore, the azide group exhibits a small Stark tuning rate and is therefore not the ideal reporter group to detect potential-dependent changes in the local electric field.

The water reservoir Three different biomimetic interfaces of (1) MBN (2) MBN/WK3SH and (3) MBN/WK3SH/POPC were examined for the analysis of the water reservoir. Performing potential-dependent SEIRA spectroscopy the frequency of the C≡N stretching changed for each of the studied biomimetic interfaces. Thus, the water reservoir was identified as a small layer of water between the SAM head group region and the lipid head group region. Also, the potential-dependent frequency and intensity changes were distinct in each of the systems. The addition of a second SAM or the creation of the tBLM restrict the MBN molecules in their potential-dependent behaviour, which may be due to steric limitations and noncovalent interactions.

The transmembrane potential The transmembrane potential of the tBLM system was obtained by the calculation of the potential difference over the lipid bilayer between the water reservoir and the bulk solution. The system was treated as two separated layers, one containing the short SAM and water layer and the other consisting of the lipid bilayer. Analysing the charge densities at the layers a relation between the applied potential and the transmembrane potential was obtained. Some errors were tolerated during the estimation of the transmembrane potential. First, the layers are not homogenous. Secondly, the distance of the first layer was set equal to the C≡N head group region and thereby underestimated by a factor of 5. Finally, the estimation only holds in a potential range near the effective potential of zero charge.

Outlook Applying solid supported membranes as biomimetic interfaces when studying the structure and activity of membrane bound proteins it is necessary to know the electrostatics. Electric fields can control the protein behaviour and it is of highest interest to quantify these electric fields. The tBLM system labelled with Stark reporter groups are a promising approach. In this work, we relied on commercially available labelled lipids, although they turned out not to be perfect for the specific systems. The labelled lipids need to exhibit a reporter group with a large Stark tuning rate like CN or SCN. Furthermore, for SEIRA experiments the reporter group must be near the surface ($d < 5 \text{ nm}$), i.e., in the head groups, preferentially in different types of head groups that allow for forming a charged membrane. In the past POPC has been utilized to construct a tBLM systems on Au. Specifically, the lipid head group and the alkyl chain of POPC should be labelled separately with CN or SCN. Hence, the electrostatics inside the membrane and at the lipid head group region can be studied by using both lipids in different experiments.

6. Appendix

A 1 Analyses of the Nanostructured Ag-film

Getting a better insight if the Ag-film changes when applying potentials different number of CVs during the electrochemical cleaning, before the SAM incubation, were performed. The light parts refer to the Ag and the dark to Si. The various dense structures can be the result of disassembling the cell.

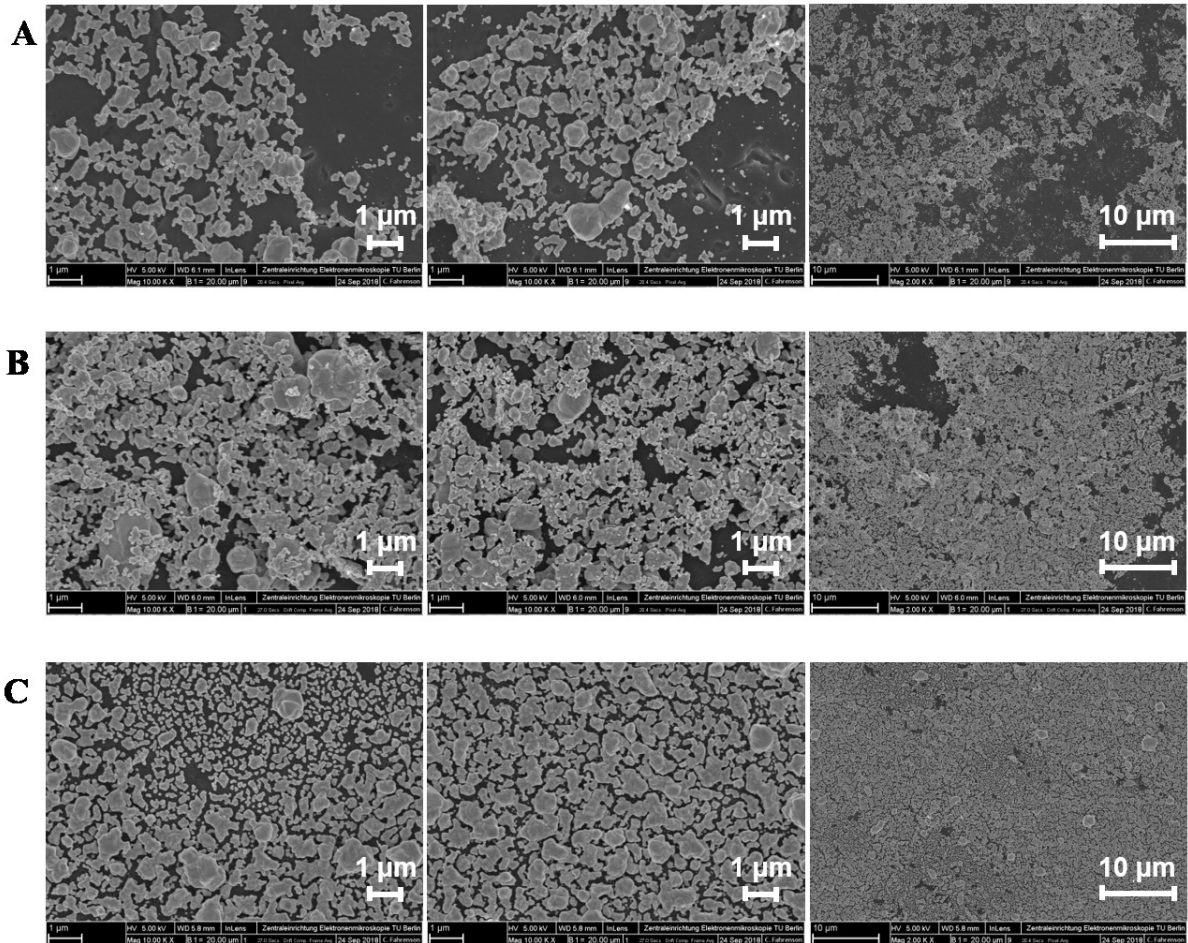


Figure A 1: SEM pictures of the nanostructured Ag film on Si after an electrochemically treatment of 6 CVs (**A**) 12 CVs (**B**) and 18 CVs (**C**) shown for different scales. The pictures were obtained together with C. Fahrenson from the ZELMI at the TU Berlin.

6. Appendix

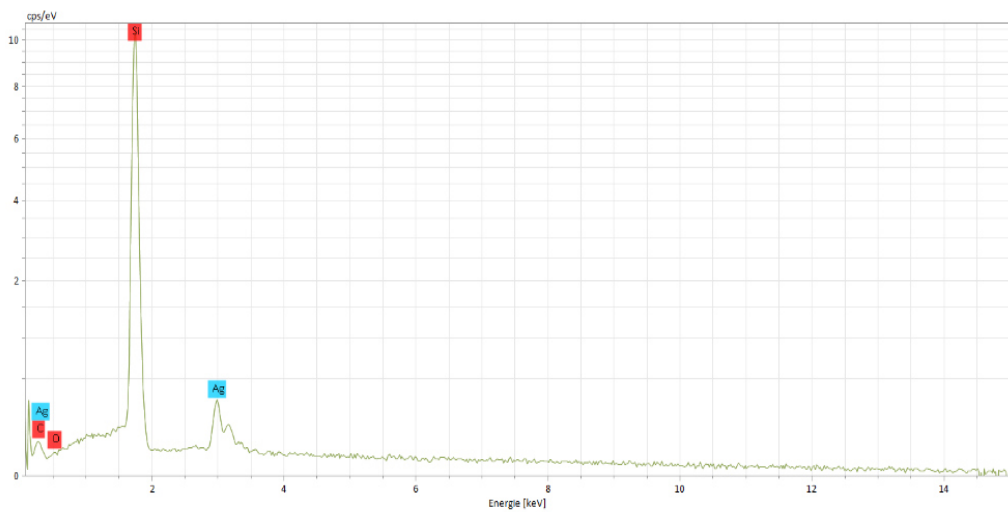


Figure A 2: EDX spectra for the Ag-film after the electrochemical treatment of 6 CVs is represented. The characteristic peaks for Si, Ag, C and O are marked. The spectra were obtained together with C. Fahrenson from the ZELMI at the TU Berlin

A 2 Solvatochromic ATR Measurement of ACN and H-bonding Effect of C4CN

The normalized C≡N vibration of acetonitrile in different solvents is shown and the corresponding frequencies are plotted in **Figure 24 A**. Additionally, the mentioned measurement of C4CN in water and propylene carbonate in the sandwich cell to obtain the H-bonding effect is depicted.

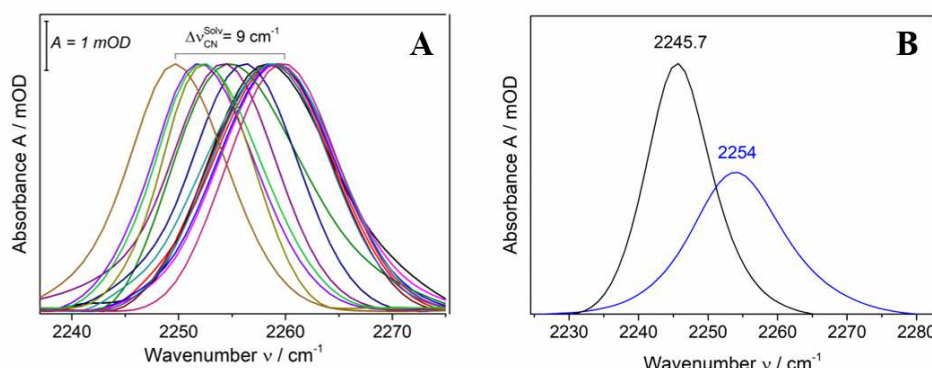


Figure A 3: Frequency of the nitrile vibration of ACN in different solvents of the solvatochromic ATR measurement (**A**) and the hydrogen bonding effect of C4CN in water (black) and in propylene carbonate (blue) (**B**).

A 3 Results of the MD Simulations of C5CN and C6CN

MD simulations performed by Dr. Tillmann Utesch to obtain information about the structure of C5CN and C6CN on Au.

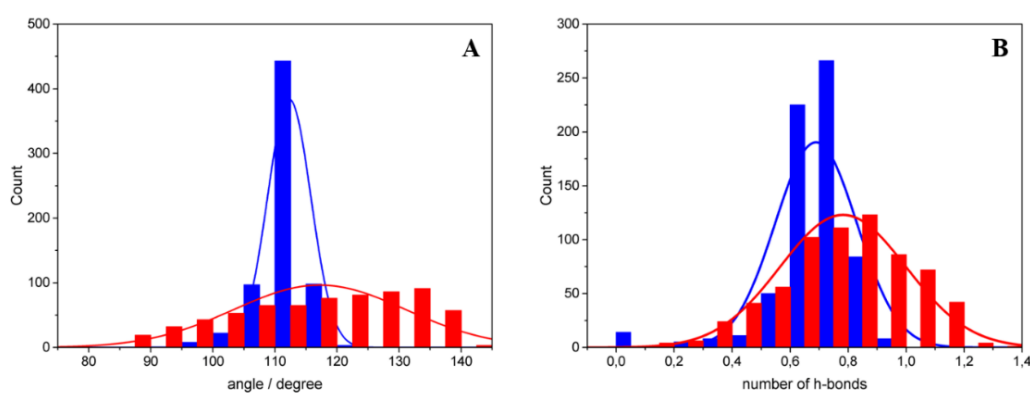


Figure A 4: Results of the MD simulations for C5CN (blue) and C6CN (red) done by Dr. Tillmann Utesch showing (**A**) the distribution of the tilt angle of the C≡N bond with respect to the surface normal and (**B**) the number of hydrogen bonding contacts.

Reprinted with permission from Staffa, J. K. *et al.* Determination of the Local Electric Field at Au/SAM Interfaces Using the Vibrational Stark Effect. *J. Phys. Chem. C* **121**, 22274–22285 (2017). Copyright 2017 American Chemical Society.

A 4 Self-assambled Monolayer Absorbed on the Nanostructured Ag-film

The potential-dependent frequency shifts of MBN, C5CN and C6CN self-assembled on Au and Ag are compared as well as the reversibility of the potential-dependent changes for Ag/MBN. Furthermore the potential-dependent potential and frequency changes of C5CN and C6CN on Ag are described with a linear (intensity, **equation (4.3)**) and non-linear (frequency, **equation(4.5)**) fit, respectively.

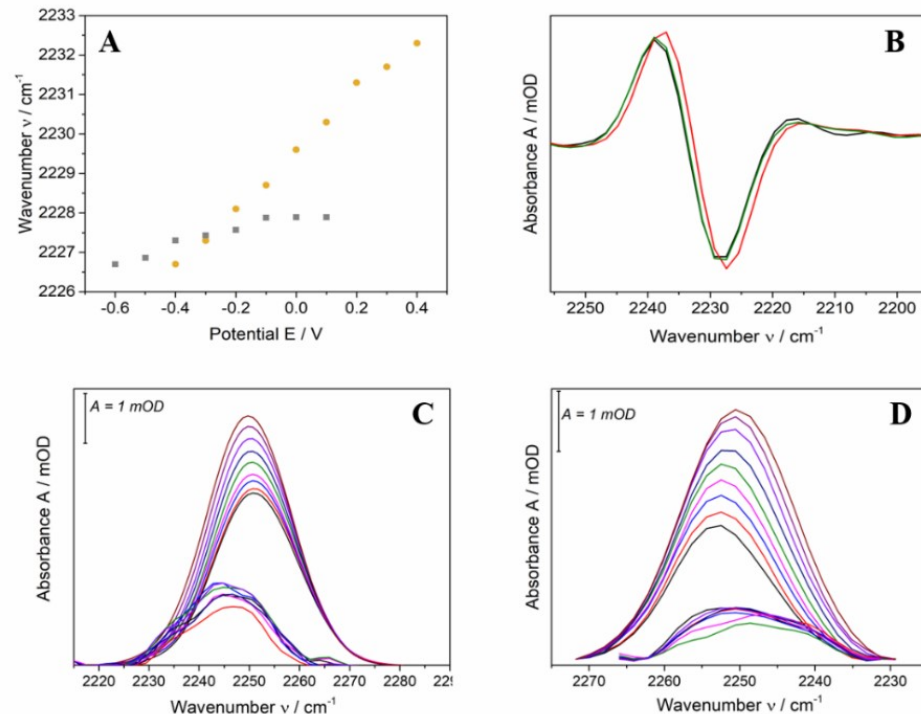


Figure A 5: In (A) the C≡N frequency shift of MBN on Au (yellow) and Ag (silver) for different potentials is represented. In (B) the reversibility of the C≡N frequency shift of MBN at 0.1 V (black, green) and -0.6 V (red) is shown. The nitrile vibration of C5CN (C) and C6CN (D) on Au (high intensity) and Ag (low intensity) at different potentials is shown. of 0.4 V (black), 0.3 V (red), 0.2 V (blue), 0.1 V (magenta), 0 V (green), -0.1 V (dark blue), -0.2 V (purple), -0.3 V (dark purple) and -0.4 V (brown)

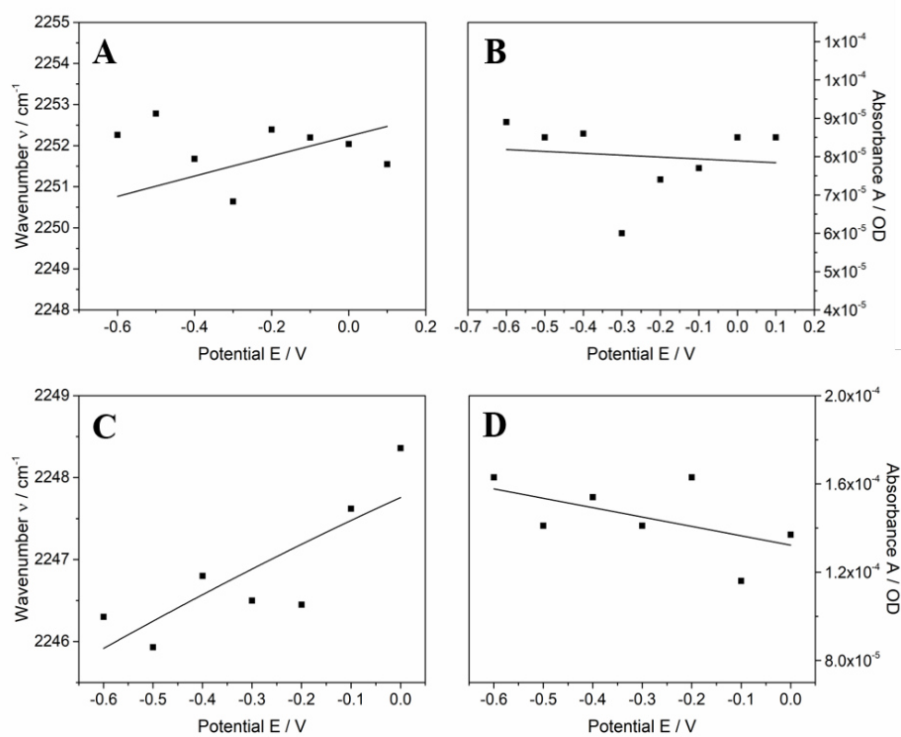


Figure A 6: Potential-dependent frequency and intensity shifts of C5CN (**A, B**) and C6CN (**C, D**) derived from SEIRA experiments. The wavenumber and intensity with a non-linear fit (frequency, **equation(4.5)**) and linear fit (intensity, **equation (4.3)**) is represented.

A 5 Further IR Spectra of the Labelled tBLM System with CLSCN

To demonstrate the intensity and irreversibility of the potential-dependent nitrile shift of CLSCN in the tBLM system further IR spectra are shown.

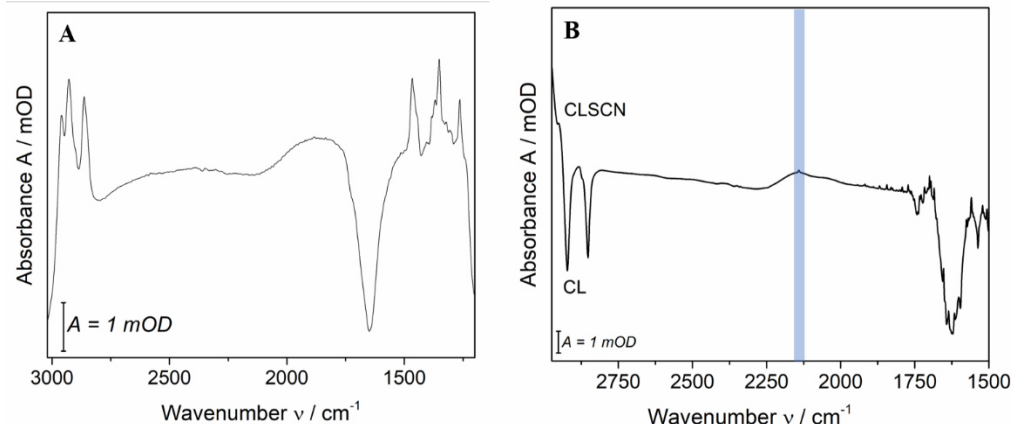


Figure A 7: SEIRA spectra of WK3SH in BTP buffer is shown in (A). In (B) difference spectra of vesicles in buffer with POPC/POPG/Cholesterol ('CL') minus POPC/POPG/CLSCN ('CLSCN') is represented with the SCN vibration marked in blue. The positive bands refer to the vesicles with CLSCN.

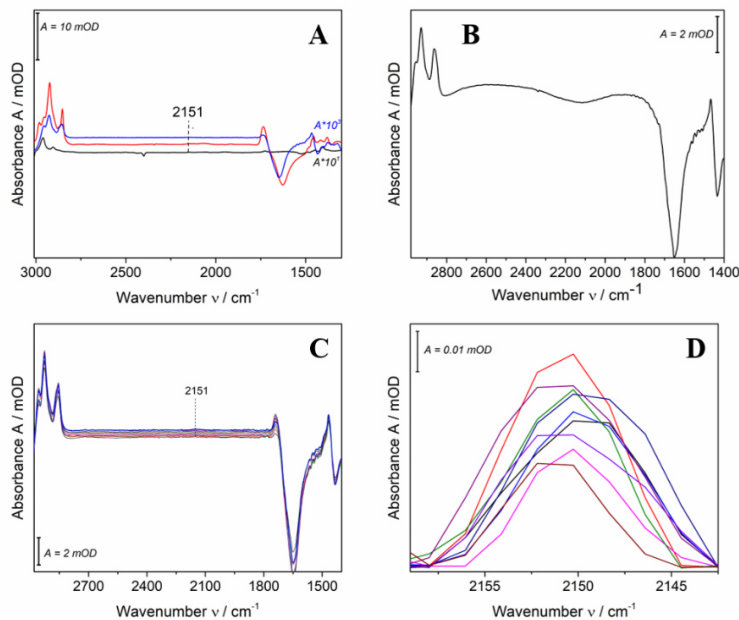


Figure A 8: (A) IR difference spectra of CLSCN in trichloromethane against trichloromethane measured with the transmission sandwich cell (black), POPC/POPG/CLSCN vesicles in buffer against buffer detected with the BioATR setup (red) and SEIRA spectra of the tBLM against the Au/WK3SH/6MH system (blue). In (B) the SEIRA spectra of the 6MH/WK3SH SAM in buffer is shown. (C) demonstrates the SEIRA spectra of the CLSCN incubation with the marked -SCN vibration and (D) shows the irreversibility of the -SCN vibration at the reference potential of 0.4 V.

A 6 Potential-dependent EIS Spectra for Different Biomimetic Interfaces

The potential-dependent EIS spectra used to calculate the potential-dependent capacitances (**Figure 36**) to obtain the effective potential of zero charge are shown.

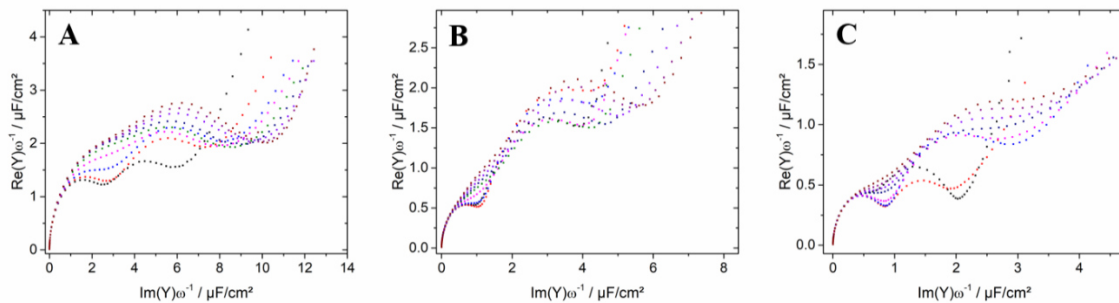


Figure A 9: The potential-dependent EIS spectra of measurements in a range from 0.4 V to -0.4 V in 0.1 V steps for MBN/WK3SH (**A**), MBN/tBLM (**B**) and tBLM/PE-N₃ (**C**) is represented.

6. Appendix

A 7 IR Spectra of the tBLM System with MBN and PE-N₃

The spectra of the nitrile vibration of MBN and azide vibration of PE-N₃ of the mixed SAM and tBLM/PE-N₃ system in buffer is shown, respectively. The reversibility of the potential-dependent shifts by the representation of the vibrations at the reference potential of 0.4 V is represented. Additionally, the potential-dependent shifts of the PE-N₃ vibrational band fitted with four gaussian bands (**Figure 39 B**) is demonstrated.

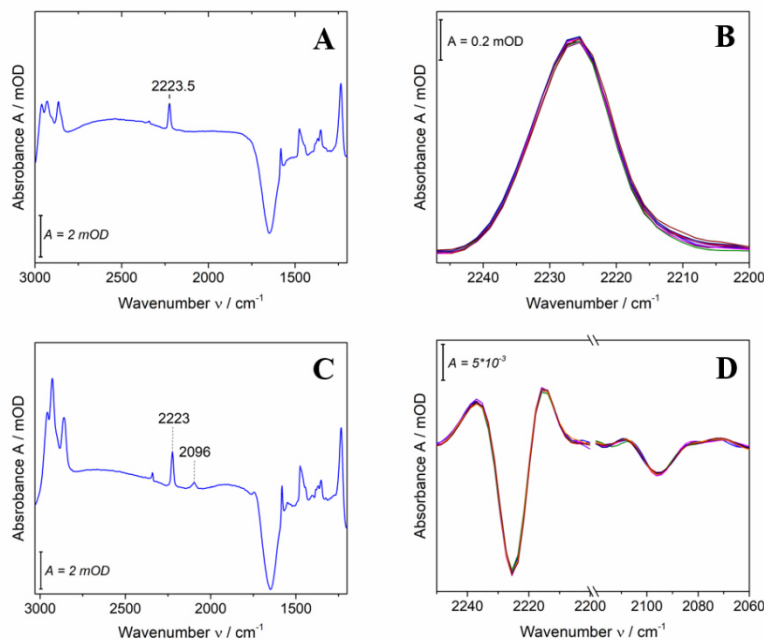


Figure A 10: IR spectra of (A) the MBN SAM in buffer, (B) the MBN vibration at the reference potential of 0.4 V, (C) the tBLM/PE-N₃ in buffer and (D) the second derivation of the reference potential of 0.4 V for the nitrile and azide vibration is shown.

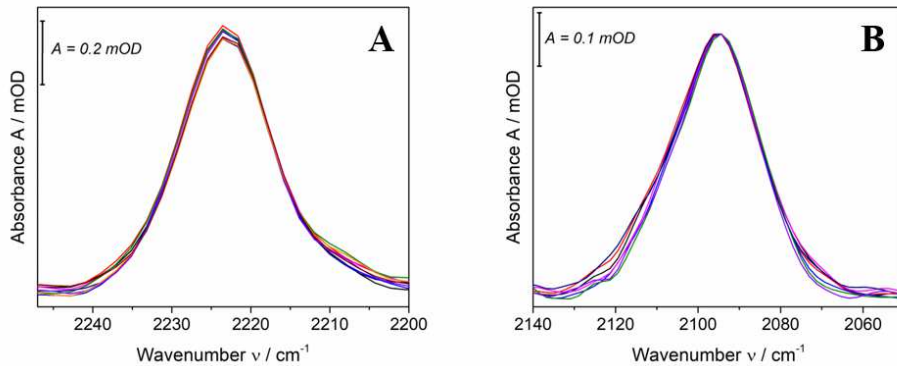


Figure A 11: The CN vibration of MBN/WK3SH (A) and azide vibration of WK3SH/POPC/PE-N₃ (B) at the reference potential of 0.4 V is represented.

The azide absorbance band was fitted with four Gaussian bands, for the analysis in chap. 4.4 the band around 2094 cm^{-1} (green squares in **Figure A 12**) were chosen. The other vibrations around 2100 cm^{-1} , 2111 cm^{-1} and 2083 cm^{-1} may belong to a small amount of different tilt angle distributions of the azide group in the solution and therefore were assumed as azide vibrations in other domains on the mixed SAM. Since the azide group can move freely in the bulk solution it can tilt in different ways based on interactions with the solution and the lipid head group region. It could also appear that vesicles did not spread on the SAM but noncovalently bound to it.

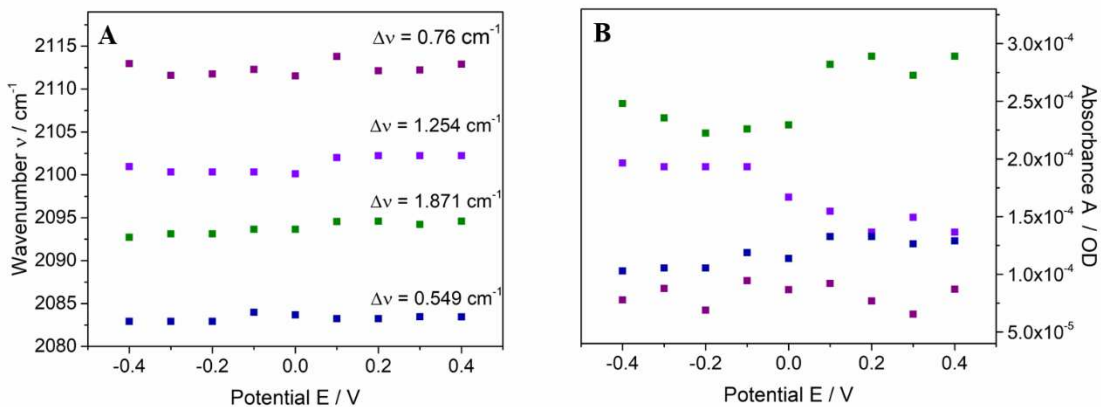


Figure A 12: Potential-dependent frequency (A) and intensity (B) changes of the azide vibration of the tBLM/PE-N₃ system fitted with four gaussian bands (**Figure 39 B**).

6. Appendix

A 8 Summary of all Electrostatics Data Obtained in this Work

The electrostatic data for different biomimetic systems determined in this work are summarized in one table.

Table A 1: Collection of the electrostatic data obtained in this work.

	Au/C5CN	Au/C6CN	Ag/C5CN	Ag/C6CN
ν_0/cm^{-1}	2252.5	2250.8	2250.39	2245.04
κ/m^{-1}	8.345×10^8	8.345×10^8	8.345×10^8	8.345×10^8
d_1/m^a	8×10^{-10}	9.7×10^{-10}	8×10^{-10}	9.7×10^{-10}
d_2/m^b	4.8×10^{-10}	4.8×10^{-10}	4.8×10^{-10}	4.8×10^{-10}
ϵ_1^c	2.3	2.3	2.3	2.3
ϵ_2^d	78	78	78	78
ϵ_s	78	78	78	78
$\Delta\mu/cm^{-1}/(Vm^{-1})^g$	3×10^{-9}	3×10^{-9}	3×10^{-9}	3×10^{-9}
φ_0	68	63	45	45
$k/CV^{-1}m^{-2}$	-1.31	-0.35	-0.33	-0.89
b/V^{-1}	-0.13	-0.11	-0.03	-0.13
σ_0/Cm^{-2}	0.0807	0.0228	0.1	0.04
E_{PZC}/V	0.2	0.1	-0.75	-0.85

^a SAM thickness minus the nitrile group, taken from MD simulations

^b set equal to the length of the nitrile group and a layer of hydrated Na⁺ ions.

^c taken from Murgida and Hildebrandt⁵⁶

^d set equal to the dielectric constant of the aqueous solution

	Ag/MBN	Au/MBN	MBN/ WK3SH	MBN/tBLM
ν_0/cm^{-1}	2226.53	2232.41	2226.62	2223.34
κ/m^{-1}	8.345×10^8	8.345×10^8	8.345×10^8	8.345×10^8
d_1/m^a	7.7×10^{-10}	5.6×10^{-10}	5.6×10^{-10}	5.6×10^{-10}
d_2/m^b	4.8×10^{-10}	4.8×10^{-10}	4.8×10^{-10}	4.8×10^{-10}
ϵ_1^c	2.3	2.3	2.3	2.3
ϵ_2^d	78	78	78	78
ϵ_s	78	78	78	78

$\Delta\mu/cm^{-1}/(Vm^{-1})^g$	6×10^{-9}	6×10^{-9}	6×10^{-9}	6×10^{-9}
φ_0	0	40	37	39
$k/CV^{-1}m^{-2}$	-0.33	-0.188	-0.12	-1.21
b/V^{-1}	-0.12	-0.45	-0.352	-0.16
σ_0/Cm^{-2}	0.1	0.206	0.228	0.137
E_{PZC}/V	-0.75	0.422	0.4	0.3

^a SAM thickness minus the nitrile group, taken from Schkolnik et al. for Au/MBN and Ag/MBN⁵⁷

^b set equal to the length of the nitrile group and a layer of hydrated Na⁺ ions.

^c taken from Murgida and Hildebrandt⁵⁶

^d set equal to the dielectric constant of the aqueous solution

	tBLM/PE-N ₃ MBN	tBLM/PE-N ₃ PE-N ₃	WK3SH/ POPC/ PE-N ₃ PE-N ₃	CLSCN
ν_0/cm^{-1}	2224.83	2094.27	2094.83	2151.24
κ/m^{-1}	8.345×10^8	8.345×10^8	8.345×10^8	8.345×10^8
d_1/m	5.6×10^{-10} ^a	2.7×10^{-10} ^a	6.7×10^{-10} ^a	3.2×10^{-10} ^a
d_2/m	4.8×10^{-10} ^b	4.8×10^{-10} ^b	4.8×10^{-10} ^b	4×10^{-9} ^b
ϵ_1	2.3 ^c	2 ^c	2 ^c	78 ^d
ϵ_2	78 ^d	78 ^d	78 ^d	2 ^c
ϵ_s	78	78	78	78
$\Delta\mu/cm^{-1}/(Vm^{-1})^g$	6×10^{-9}	2×10^{-9}	2×10^{-9}	4.8×10^{-9}
φ_0	39	18	18	17
$k/CV^{-1}m^{-2}$	-0.056	-5.1	-4.9	-0.635
b/V^{-1}	-0.32	0.26	0.107	0.31
σ_0/Cm^{-2}	0.079	0.0797	0.797	0.12
E_{PZC}/V	0.2	0.2	0.2	0.27

^{a,b} estimated under the consideration of the length of the molecules of a tBLM (**Table 10**)

^c taken from Murgida and Hildebrandt⁵⁶ for MBN and from Horrocks et al. for the tBLM¹²³

^d set equal to the dielectric constant of the aqueous solution

6. Appendix

A 9 Cartesian Coordinates of the DFT Calculations

Cartesian Coordinates for the solvatochromic DFT calculations of CHCN, MeSCN, COOHC₅N₃ and ACN as well as electric field-dependent calculations of C5CN and C6CN are given.

CHCN vac

Atom	Coordinates (Angstroms)		
	X	Y	Z
C	-1.079228	-2.251419	0.839528
C	-0.078881	-2.436723	-0.306885
C	1.099086	-1.46313	-0.198362
C	0.601582	-0.002651	-0.115784
C	-0.398049	0.185099	1.047296
C	-1.565112	-0.80052	0.929658
H	0.296764	-3.461095	-0.321476
H	1.683597	-1.684314	0.698015
H	0.129789	0.026154	1.990787
H	-2.153248	-0.559041	0.038619
C	1.724682	0.930949	-0.001229
N	2.611285	1.657773	0.102759
H	1.771665	-1.574527	-1.049104
H	-0.58945	-2.280664	-1.262457
H	-2.233165	-0.675906	1.783375
H	-0.760547	1.213214	1.057779
H	-1.928311	-2.924604	0.709731
H	-0.601528	-2.531011	1.783643
H	0.0879	0.238318	-1.052003

CHCN Cyclohexane

Atom	Coordinates (Angstroms)		
	X	Y	Z
C	-1.078972	-2.251085	0.839243
C	-0.078749	-2.436299	-0.307149
C	1.100255	-1.464173	-0.197551
C	0.600615	-0.003895	-0.115319
C	-0.398039	0.185453	1.049007
C	-1.564787	-0.80029	0.929571
H	0.297401	-3.460371	-0.321606
H	1.682897	-1.686007	0.699711
H	0.129335	0.025081	1.992413
H	-2.151729	-0.557839	0.038265
C	1.722972	0.930027	-0.002214
N	2.609201	1.65831	0.09937
H	1.772059	-1.575709	-1.048748

H	-0.588289	-2.278728	-1.262818
H	-2.232236	-0.675397	1.783574
H	-0.761499	1.213141	1.058398
H	-1.928379	-2.923487	0.708105
H	-0.601553	-2.531152	1.783278
H	0.088328	0.238321	-1.051638

CHCN trichloromethane

Atom	Coordinates (Angstroms)		
	X	Y	Z
C	-1.07865	-2.250866	0.839282
C	-0.078692	-2.436077	-0.307262
C	1.100894	-1.464726	-0.197344
C	0.599975	-0.004545	-0.115265
C	-0.398167	0.185768	1.04978
C	-1.564634	-0.800184	0.929497
H	0.297891	-3.459945	-0.321508
H	1.682702	-1.686912	0.70029
H	0.128896	0.024701	1.993171
H	-2.150873	-0.557336	0.038023
C	1.721921	0.92922	-0.002472
N	2.608261	1.657896	0.098758
H	1.771748	-1.576211	-1.049219
H	-0.587806	-2.277637	-1.262849
H	-2.231562	-0.675108	1.783822
H	-0.762397	1.213132	1.058083
H	-1.928213	-2.922912	0.707517
H	-0.60117	-2.530905	1.783247
H	0.088709	0.238548	-1.05166

CHCN tetrahydrofuran

Atom	Coordinates (Angstroms)		
	X	Y	Z
C	-1.07849	-2.250779	0.839355
C	-0.078676	-2.43601	-0.307284
C	1.10111	-1.464909	-0.197357
C	0.59973	-0.004759	-0.115296
C	-0.398255	0.18591	1.049991
C	-1.564596	-0.800151	0.929462
H	0.298099	-3.459797	-0.321412
H	1.682729	-1.687219	0.700346
H	0.128672	0.024642	1.993397
H	-2.150586	-0.557209	0.037925
C	1.721547	0.928857	-0.002451
N	2.608008	1.657553	0.098922

6. Appendix

H	1.771468	-1.57633	-1.049606
H	-0.587687	-2.277284	-1.262805
H	-2.231297	-0.675003	1.783939
H	-0.76281	1.21314	1.057781
H	-1.928096	-2.922732	0.707415
H	-0.60093	-2.530722	1.783292
H	0.088892	0.238705	-1.051725

CHCN dichloromethane

Atom	Coordinates (Angstroms)		
	X	Y	Z
C	-1.078435	-2.250751	0.839386
C	-0.078671	-2.435992	-0.307287
C	1.101175	-1.464964	-0.197374
C	0.599652	-0.004823	-0.115312
C	-0.398289	0.185958	1.050048
C	-1.564587	-0.800142	0.929449
H	0.298169	-3.459753	-0.321374
H	1.682753	-1.687312	0.700341
H	0.128592	0.024635	1.993462
H	-2.150501	-0.557177	0.037893
C	1.721432	0.928734	-0.002428
N	2.607942	1.657421	0.099026
H	1.771357	-1.576359	-1.049757
H	-0.587657	-2.277181	-1.262784
H	-2.231212	-0.67497	1.783979
H	-0.762951	1.213145	1.057662
H	-1.928052	-2.92268	0.707398
H	-0.600843	-2.530652	1.783313
H	0.088956	0.238764	-1.051752

CHCN acetone

Atom	Coordinates (Angstroms)		
	X	Y	Z
C	-1.078256	-2.250666	0.8395
C	-0.078658	-2.435944	-0.307288
C	1.101362	-1.465117	-0.197462
C	0.59942	-0.005003	-0.115378
C	-0.398406	0.186111	1.050183
C	-1.564569	-0.800118	0.929409
H	0.298384	-3.459627	-0.321233
H	1.682877	-1.687575	0.700252
H	0.128324	0.024652	1.993631
H	-2.150268	-0.557102	0.037799
C	1.721104	0.928344	-0.002306

N	2.607787	1.656956	0.09949
H	1.770961	-1.576414	-1.050295
H	-0.587592	-2.276904	-1.262698
H	-2.230956	-0.674874	1.784109
H	-0.763398	1.213164	1.057234
H	-1.9279	-2.922541	0.707396
H	-0.600549	-2.53041	1.783401
H	0.089165	0.238968	-1.051855

CHCN DMSO

Atom	Coordinates (Angstroms)		
	X	Y	Z
C	-1.078184	-2.250633	0.839552
C	-0.078654	-2.435929	-0.307284
C	1.101428	-1.46517	-0.19751
C	0.599333	-0.005065	-0.115409
C	-0.398457	0.186171	1.050221
C	-1.564567	-0.80011	0.929393
H	0.298468	-3.459582	-0.321171
H	1.682945	-1.687668	0.700189
H	0.128213	0.024673	1.993685
H	-2.150191	-0.557084	0.037764
C	1.720988	0.928189	-0.002239
N	2.607746	1.656753	0.099725
H	1.770786	-1.576422	-1.050532
H	-0.587577	-2.276812	-1.262657
H	-2.230858	-0.674839	1.784162
H	-0.763576	1.213174	1.057045
H	-1.927835	-2.922495	0.707414
H	-0.600427	-2.530306	1.783443
H	0.089251	0.239056	-1.051902

CHCN PC

Atom	Coordinates (Angstroms)		
	X	Y	Z
C	-1.078153	-2.250619	0.839576
C	-0.078652	-2.435923	-0.307281
C	1.101456	-1.465192	-0.197534
C	0.599296	-0.005092	-0.115424
C	-0.398481	0.186198	1.050234
C	-1.564567	-0.800106	0.929386
H	0.298504	-3.459564	-0.321142
H	1.682978	-1.687706	0.700157
H	0.128162	0.024685	1.993707
H	-2.15016	-0.557077	0.03775

6. Appendix

C	1.720939	0.928121	-0.002206
N	2.607732	1.656661	0.099837
H	1.770706	-1.576424	-1.050641
H	-0.587571	-2.276774	-1.262637
H	-2.230816	-0.674824	1.784185
H	-0.763655	1.213178	1.056958
H	-1.927805	-2.922477	0.707425
H	-0.600372	-2.530259	1.783463
H	0.08929	0.239096	-1.051924

MeSCN vac

Atom	Coordinates (Angstroms)		
	X	Y	Z
C	-1.36205	0.88653	0.116189
N	-0.21177	1.003967	0.134304
S	-3.046327	0.671907	0.134807
C	-3.529455	1.859729	-1.181822
H	-4.612843	1.787983	-1.239965
H	-3.238495	2.866685	-0.902376
H	-3.086768	1.569224	-2.128577

MeSCN cyclohexane

Atom	Coordinates (Angstroms)		
	X	Y	Z
C	-1.360211	0.887267	0.116331
N	-0.209146	1.000646	0.140943
S	-3.04357	0.673123	0.131265
C	-3.530384	1.861768	-1.184776
H	-4.613564	1.786272	-1.235031
H	-3.239372	2.867948	-0.90402
H	-3.091463	1.569002	-2.132152

MeSCN trichloromethane

Atom	Coordinates (Angstroms)		
	X	Y	Z
C	-1.359146	0.88772	0.116135
N	-0.207462	0.997807	0.144299
S	-3.041913	0.674649	0.129868
C	-3.531	1.863121	-1.186364
H	-4.613911	1.784537	-1.232872
H	-3.240956	2.869125	-0.904848
H	-3.093321	1.569068	-2.133658

MeSCN tetrahydrofuran

Atom	Coordinates (Angstroms)		
	X	Y	Z
C	-1.358773	0.887879	0.116003
N	-0.206833	0.99659	0.145315
S	-3.04133	0.675398	0.129576
C	-3.531237	1.863639	-1.186897
H	-4.614015	1.783747	-1.232318
H	-3.24179	2.869644	-0.905088
H	-3.093729	1.56913	-2.13403

MeSCN dichloromethane

Atom	Coordinates (Angstroms)		
	X	Y	Z
C	-1.358658	0.887926	0.115954
N	-0.206634	0.996182	0.1456
S	-3.041152	0.675662	0.129519
C	-3.531314	1.863805	-1.187057
H	-4.614045	1.783475	-1.232181
H	-3.242091	2.86982	-0.905154
H	-3.093814	1.569155	-2.13412

MeSCN acetone

Atom	Coordinates (Angstroms)		
	X	Y	Z
C	-1.358326	0.888057	0.115784
N	-0.206042	0.994892	0.146328
S	-3.040643	0.676541	0.129467
C	-3.531543	1.864304	-1.187504
H	-4.614122	1.782594	-1.231898
H	-3.243106	2.870385	-0.905321
H	-3.093927	1.569253	-2.134297

MeSCN DMSO

Atom	Coordinates (Angstroms)		
	X	Y	Z
C	-1.358205	0.888102	0.115712
N	-0.20582	0.994379	0.146551
S	-3.040461	0.676908	0.129497
C	-3.53163	1.864492	-1.187659
H	-4.614146	1.782235	-1.231844
H	-3.243535	2.870612	-0.905371
H	-3.093911	1.569299	-2.134325

6. Appendix

MeSCN PC

Atom	Coordinates (Angstroms)		
	X	Y	Z
C	-1.358154	0.88812	0.115679
N	-0.205724	0.994153	0.146638
S	-3.040384	0.677072	0.129518
C	-3.531668	1.864573	-1.187724
H	-4.614156	1.782075	-1.231829
H	-3.243729	2.870713	-0.90539
H	-3.093894	1.56932	-2.134331

COOHC₅N₃ vac

Atom	Coordinates (Angstroms)		
	X	Y	Z
C	0.298122	0.03068	0.076884
C	1.043583	-1.299091	0.144838
H	0.639533	0.588168	-0.797315
H	0.568973	0.63745	0.942933
H	0.74014	-1.880203	1.019409
H	0.811081	-1.929253	-0.717419
C	2.543385	-1.143202	0.20171
O	3.150611	-0.103319	0.19713
O	3.166327	-2.347235	0.26121
H	4.117471	-2.170968	0.295086
C	-1.218465	-0.159819	0.020776
C	-1.959887	1.166893	-0.046896
H	-1.563628	-0.710485	0.898845
H	-1.492722	-0.759985	-0.84983
H	-1.729688	1.778544	0.83017
H	-1.657878	1.728576	-0.935522
N	-3.417425	0.897956	-0.098556
N	-4.14366	1.886675	-0.156392
N	-4.904725	2.722798	-0.211296

COOHC₅N₃ cyclohexane

Atom	Coordinates (Angstroms)		
	X	Y	Z
C	0.29949	0.035097	0.077937
C	1.044487	-1.294722	0.148014
H	0.636372	0.590514	-0.799233
H	0.567819	0.643858	0.943251
H	0.741874	-1.871871	1.025445
H	0.808437	-1.926634	-0.71182
C	2.544108	-1.14586	0.201092
O	3.157173	-0.106707	0.199332

O	3.162416	-2.349875	0.253466
H	4.116191	-2.184988	0.285641
C	-1.216929	-0.159218	0.023971
C	-1.958489	1.166723	-0.047915
H	-1.557843	-0.70741	0.905104
H	-1.488523	-0.76295	-0.844894
H	-1.732385	1.781344	0.827251
H	-1.66036	1.725394	-0.938872
N	-3.419073	0.897817	-0.098966
N	-4.145902	1.883777	-0.158426
N	-4.907717	2.719892	-0.214613

COOHC₅N₃ trichloromethane

Atom	Coordinates (Angstroms)		
	X	Y	Z
C	0.300405	0.037621	0.077638
C	1.045006	-1.292226	0.149389
H	0.634365	0.591247	-0.801728
H	0.567013	0.647702	0.942513
H	0.74287	-1.866756	1.02862
H	0.806886	-1.925101	-0.709071
C	2.5444	-1.147714	0.200025
O	3.161278	-0.108982	0.195743
O	3.159761	-2.3513	0.253258
H	4.115069	-2.193237	0.283628
C	-1.215941	-0.158755	0.025193
C	-1.95737	1.166869	-0.048483
H	-1.553992	-0.705615	0.908185
H	-1.485878	-0.764265	-0.842889
H	-1.733315	1.782892	0.825643
H	-1.662201	1.723935	-0.940863
N	-3.419871	0.897967	-0.098404
N	-4.147374	1.882039	-0.158139
N	-4.909965	2.717857	-0.214491

COOHC₅N₃ tetrahydrofuran

Atom	Coordinates (Angstroms)		
	X	Y	Z
C	0.300759	0.038431	0.077024
C	1.045138	-1.291431	0.149904
H	0.633348	0.590783	-0.803656
H	0.567087	0.649457	0.941306
H	0.743155	-1.864628	1.030028
H	0.806282	-1.924944	-0.707839
C	2.544419	-1.148451	0.199721

6. Appendix

O	3.162619	-0.109812	0.194511
O	3.158789	-2.351796	0.253414
H	4.114614	-2.196098	0.283226
C	-1.215597	-0.158548	0.025824
C	-1.956883	1.166996	-0.048803
H	-1.552272	-0.704444	0.909919
H	-1.485286	-0.765083	-0.841598
H	-1.73317	1.783871	0.824596
H	-1.663123	1.723062	-0.942064
N	-3.420105	0.89814	-0.09759
N	-4.147871	1.881504	-0.157751
N	-4.910758	2.717168	-0.214406

COOHC₅N₃ dichloromethane

Atom	Coordinates (Angstroms)		
	X	Y	Z
C	0.300868	0.038673	0.0768
C	1.045185	-1.291189	0.150025
H	0.63303	0.59063	-0.804287
H	0.567094	0.649979	0.940911
H	0.743174	-1.864017	1.030371
H	0.806196	-1.924851	-0.707555
C	2.544417	-1.148653	0.199768
O	3.162992	-0.110015	0.194563
O	3.158518	-2.351904	0.253415
H	4.114493	-2.196913	0.283204
C	-1.215489	-0.158495	0.025974
C	-1.956733	1.167025	-0.048922
H	-1.551732	-0.704103	0.910405
H	-1.485088	-0.765333	-0.841258
H	-1.733128	1.784143	0.824264
H	-1.663417	1.722799	-0.942447
N	-3.420177	0.898175	-0.097358
N	-4.148035	1.88131	-0.15767
N	-4.911022	2.716917	-0.214437

COOHC₅N₃ acetone

Atom	Coordinates (Angstroms)		
	X	Y	Z
C	0.301207	0.039308	0.075759
C	1.045257	-1.29057	0.15039
H	0.63182	0.5896	-0.806954
H	0.567511	0.651838	0.938968
H	0.743223	-1.861967	1.031637
H	0.805775	-1.924958	-0.706465

C	2.544342	-1.14934	0.199798
O	3.163986	-0.110677	0.194657
O	3.157687	-2.352291	0.253206
H	4.114093	-2.199335	0.282923
C	-1.215187	-0.158296	0.026701
C	-1.956226	1.167178	-0.049286
H	-1.549847	-0.702622	0.912507
H	-1.484886	-0.766386	-0.839601
H	-1.732597	1.785343	0.822954
H	-1.664488	1.721706	-0.94391
N	-3.420355	0.898418	-0.096074
N	-4.148456	1.880892	-0.157082
N	-4.91171	2.716335	-0.214358

COOHC₅N₃ DMSO

Atom	Coordinates (Angstroms)		
	X	Y	Z
C	0.301333	0.039512	0.075283
C	1.045268	-1.290374	0.15049
H	0.631315	0.589098	-0.808109
H	0.567745	0.652555	0.938091
H	0.743184	-1.861218	1.032072
H	0.805649	-1.925046	-0.706096
C	2.544289	-1.149599	0.19988
O	3.164283	-0.110897	0.195015
O	3.157397	-2.352419	0.25301
H	4.113951	-2.200178	0.282817
C	-1.21508	-0.15822	0.027009
C	-1.956024	1.167245	-0.049417
H	-1.549092	-0.701996	0.913393
H	-1.48489	-0.76683	-0.838886
H	-1.732313	1.785844	0.82242
H	-1.664922	1.72125	-0.944502
N	-3.420411	0.898535	-0.095473
N	-4.148594	1.880766	-0.156842
N	-4.911938	2.716148	-0.21439

COOHC₅N₃PC

Atom	Coordinates (Angstroms)		
	X	Y	Z
C	0.301388	0.039594	0.075052
C	1.045269	-1.290297	0.150529
H	0.631088	0.588851	-0.808653
H	0.567865	0.652876	0.937669
H	0.743153	-1.86089	1.03226

6. Appendix

H	0.805601	-1.925096	-0.705938
C	2.544261	-1.14971	0.199929
O	3.1644	-0.110988	0.195188
O	3.157273	-2.352472	0.252943
H	4.113889	-2.200531	0.282797
C	-1.215035	-0.158186	0.027145
C	-1.955935	1.167276	-0.049485
H	-1.548753	-0.701705	0.913796
H	-1.484909	-0.767038	-0.838557
H	-1.732172	1.786077	0.822164
H	-1.665118	1.721037	-0.944784
N	-3.420433	0.898589	-0.095197
N	-4.148651	1.880717	-0.156717
N	-4.912034	2.716073	-0.214377

ACN vac

Atom	Coordinates (Angstroms)		
	X	Y	Z
C	-0.000023	-0.000051	0.267466
N	0.000002	0.000079	1.419485
C	0.000007	-0.000011	-1.189204
H	0.000064	1.02318	-1.570108
H	0.88607	-0.511659	-1.570166
H	-0.88612	-0.511537	-1.570199

ACN 2-methylbutan

Atom	Coordinates (Angstroms)		
	X	Y	Z
C	0	0.000003	0.263993
N	0.000001	-0.000016	1.414166
C	0	0.000011	-1.192653
H	-0.000014	1.022698	-1.566087
H	0.885695	-0.511336	-1.566073
H	-0.885683	-0.511359	-1.566073

ACN n-hexane

Atom	Coordinates (Angstroms)		
	X	Y	Z
C	0.000001	0.000002	0.263895
N	-0.000009	-0.00005	1.41409
C	0.000006	0.000021	-1.192684
H	0.000094	1.02273	-1.566012
H	0.88566	-0.511441	-1.566005
H	-0.885753	-0.511262	-1.566011

ACN n-heptane

Atom	Coordinates (Angstroms)		
	X	Y	Z
C	-0.000002	0.000001	0.26381
N	-0.000006	-0.000035	1.414031
C	0.000003	0.000017	-1.192735
H	0.000092	1.022754	-1.565952
H	0.88569	-0.51145	-1.565938
H	-0.885776	-0.511288	-1.565944

ACN 2-cyclohexane

Atom	Coordinates (Angstroms)		
	X	Y	Z
C	0.000004	0.000022	0.263587
N	-0.000002	-0.000033	1.413868
C	0.000003	0.00002	-1.19284
H	-0.000002	1.02281	-1.565817
H	0.885789	-0.511414	-1.565763
H	-0.885792	-0.511405	-1.565761

ACN toluol

Atom	Coordinates (Angstroms)		
	X	Y	Z
C	0.000003	0.00002	0.263461
N	-0.000001	-0.000028	1.413776
C	0.000002	0.000018	-1.192896
H	-0.000002	1.022844	-1.565724
H	0.88582	-0.51143	-1.565673
H	-0.885822	-0.511424	-1.565672

ACN trichloromethane

Atom	Coordinates (Angstroms)		
	X	Y	Z
C	0.00001	0.000015	0.262441
N	0.00001	-0.000091	1.413045
C	-0.000001	0.000033	-1.193305
H	-0.00004	1.023132	-1.565003
H	0.886077	-0.511517	-1.56496
H	-0.886056	-0.511571	-1.564946

6. Appendix

ACN tetrahydrofuran

Atom	Coordinates (Angstroms)		
	X	Y	Z
C	0.000009	0.000021	0.262007
N	0.000016	-0.000155	1.412739
C	-0.000001	0.000047	-1.193442
H	-0.000013	1.023253	-1.564714
H	0.886159	-0.511583	-1.564665
H	-0.886169	-0.511583	-1.564652

ACN dichloromethane

Atom	Coordinates (Angstroms)		
	X	Y	Z
C	0.000009	0.000019	0.261869
N	0.000017	-0.000167	1.412643
C	-0.000002	0.00005	-1.193489
H	-0.000005	1.02329	-1.56462
H	0.886187	-0.511602	-1.564572
H	-0.886206	-0.511589	-1.564558

ACN 1-propanol

Atom	Coordinates (Angstroms)		
	X	Y	Z
C	0.000007	0.000018	0.261516
N	0.000024	-0.000228	1.412398
C	-0.000006	0.000063	-1.1936
H	0.000026	1.023381	-1.564391
H	0.88625	-0.511643	-1.564334
H	-0.886301	-0.511591	-1.564315

ACN acetone

Atom	Coordinates (Angstroms)		
	X	Y	Z
C	0.000009	0.000025	0.261464
N	0.000023	-0.000262	1.412364
C	-0.000006	0.000072	-1.193616
H	0.00003	1.023397	-1.564369
H	0.88626	-0.511645	-1.564295
H	-0.886315	-0.511588	-1.564274

ACN ethanol

Atom	Coordinates (Angstroms)		
	X	Y	Z
C	0.000011	0.00001	0.26142
N	0.000023	-0.000254	1.41233
C	-0.000006	0.000068	-1.19363
H	0.000029	1.023418	-1.564314
H	0.886271	-0.511653	-1.564277
H	-0.886328	-0.511589	-1.564257

ACN methanol

Atom	Coordinates (Angstroms)		
	X	Y	Z
C	0.000011	0.000005	0.26135
N	0.000023	-0.00028	1.412282
C	-0.000006	0.000074	-1.193651
H	0.000029	1.023442	-1.564263
H	0.886287	-0.511653	-1.564233
H	-0.886344	-0.511589	-1.564212

ACN dimethyl sulfoxide

Atom	Coordinates (Angstroms)		
	X	Y	Z
C	0.000012	0.000003	0.261308
N	0.000023	-0.000296	1.412253
C	-0.000006	0.000078	-1.193663
H	0.000027	1.023457	-1.564233
H	0.886297	-0.511651	-1.564206
H	-0.886353	-0.51159	-1.564185

ACN propylene carbonate

Atom	Coordinates (Angstroms)		
	X	Y	Z
C	0.000016	0.000094	0.261231
N	0.000001	-0.000109	1.412207
C	-0.000001	0.000035	-1.193693
H	0.000006	1.023397	-1.564279
H	0.886331	-0.511719	-1.564105
H	-0.886353	-0.511697	-1.564088

6. Appendix

C5CN vac

Atom	Coordinates (Angstroms)		
	X	Y	Z
C	0.032145	-0.015879	-0.098251
N	1.182715	-0.070892	-0.141176
C	-1.424669	0.064668	-0.019083
H	-1.78103	0.678996	-0.852709
H	-1.83424	-0.938831	-0.175681
C	-1.91886	0.641782	1.321811
H	-1.484211	1.636122	1.46514
H	-1.541881	0.019747	2.139675
C	-3.446844	0.722864	1.385373
H	-3.87257	-0.276655	1.229562
H	-3.814642	1.342175	0.557234
C	-3.954597	1.290966	2.717006
H	-3.526554	2.287853	2.875697
H	-3.601305	0.671631	3.547698
C	-5.478637	1.378978	2.772149
H	-5.92687	0.390397	2.644649
H	-5.871332	2.012022	1.973625
S	-6.150102	1.966633	4.382229
H	-5.634232	3.21566	4.32081

C5CN electric field z+50

Atom	Coordinates (Angstroms)		
	X	Y	Z
C	0.039758	-0.035693	-0.089111
N	1.191311	-0.110792	-0.115984
C	-1.417046	0.07146	-0.030293
H	-1.745684	0.710733	-0.856084
H	-1.840885	-0.92116	-0.213599
C	-1.921786	0.630807	1.316719
H	-1.473866	1.615826	1.483358
H	-1.566907	-0.016098	2.125345
C	-3.449777	0.736284	1.369053
H	-3.889773	-0.254655	1.20337
H	-3.803086	1.371248	0.547443
C	-3.946478	1.299772	2.707928
H	-3.532086	2.303874	2.857024
H	-3.567321	0.684779	3.531096
C	-5.471438	1.363733	2.804226
H	-5.906747	0.367239	2.699199
H	-5.898767	1.98382	2.013785
S	-6.094255	1.961214	4.429306
H	-5.752885	3.255844	4.262977

C5CN electric field z+25

Atom	Coordinates (Angstroms)		
	X	Y	Z
C	0.036031	-0.025608	-0.093377
N	1.187265	-0.092684	-0.129748
C	-1.420735	0.069761	-0.02472
H	-1.760969	0.698743	-0.853804
H	-1.837074	-0.92837	-0.19537
C	-1.920548	0.636888	1.319959
H	-1.480281	1.627007	1.474887
H	-1.55499	0.001144	2.132428
C	-3.448894	0.729262	1.377572
H	-3.880503	-0.266518	1.217322
H	-3.809105	1.357183	0.553238
C	-3.951879	1.294636	2.713063
H	-3.532056	2.295765	2.865859
H	-3.585219	0.676888	3.539412
C	-5.476946	1.369406	2.788025
H	-5.917655	0.375825	2.675914
H	-5.885997	1.99378	1.991065
S	-6.125972	1.967936	4.40309
H	-5.682189	3.237192	4.290943

C5CN electric field z+10

Atom	Coordinates (Angstroms)		
	X	Y	Z
C	0.03383	-0.019561	-0.096693
N	1.18488	-0.080452	-0.139836
C	-1.422864	0.06725	-0.021001
H	-1.771343	0.68853	-0.852549
H	-1.833745	-0.93475	-0.182393
C	-1.919495	0.640384	1.321836
H	-1.483671	1.633542	1.468788
H	-1.54761	0.012018	2.137028
C	-3.448024	0.72532	1.38267
H	-3.874867	-0.273252	1.226012
H	-3.812129	1.348824	0.556494
C	-3.954748	1.292304	2.715994
H	-3.53125	2.291418	2.871187
H	-3.596109	0.672683	3.544235
C	-5.479745	1.374332	2.777749
H	-5.924076	0.38296	2.659254
H	-5.877067	2.003024	1.97814
S	-6.144642	1.971297	4.387535
H	-5.645042	3.222363	4.31131

6. Appendix

C5CN electric field z+0

Atom	Coordinates (Angstroms)		
	X	Y	Z
C	0.03235	-0.015265	-0.099277
N	1.183255	-0.071644	-0.147313
C	-1.424249	0.065463	-0.018526
H	-1.77852	0.681649	-0.851486
H	-1.831269	-0.939126	-0.173847
C	-1.918719	0.642288	1.323244
H	-1.485673	1.637299	1.4652
H	-1.542807	0.018521	2.140026
C	-3.447355	0.722613	1.386176
H	-3.871247	-0.277691	1.23184
H	-3.813836	1.343295	0.558786
C	-3.956535	1.290764	2.718048
H	-3.530492	2.288472	2.874878
H	-3.603345	0.669863	3.547534
C	-5.481422	1.377834	2.770974
H	-5.928249	0.387991	2.64832
H	-5.870786	2.009351	1.969616
S	-6.156735	1.97444	4.377063
H	-5.622082	3.212119	4.324501

C5CN electric field z-10

Atom	Coordinates (Angstroms)		
	X	Y	Z
C	0.030864	-0.010643	-0.102135
N	1.181605	-0.061994	-0.155415
C	-1.425603	0.063452	-0.015971
H	-1.786055	0.674321	-0.850274
H	-1.828408	-0.943837	-0.16505
C	-1.917911	0.643937	1.324758
H	-1.487593	1.64074	1.461773
H	-1.538043	0.024708	2.143073
C	-3.446652	0.719791	1.389756
H	-3.86769	-0.282193	1.237773
H	-3.815392	1.337651	0.561111
C	-3.958302	1.289245	2.720132
H	-3.529573	2.28547	2.878634
H	-3.610743	0.667025	3.550877
C	-5.483021	1.381636	2.764104
H	-5.932483	0.39343	2.637164
H	-5.864201	2.01611	1.961096
S	-6.168698	1.978163	4.36642
H	-5.599817	3.201224	4.337933

C5CN electric field z-25

Atom	Coordinates (Angstroms)		
	X	Y	Z
C	0.028528	-0.004059	-0.107031
N	1.178934	-0.047576	-0.168868
C	-1.427612	0.059868	-0.012071
H	-1.797739	0.662437	-0.848311
H	-1.823947	-0.951478	-0.151379
C	-1.916393	0.646145	1.327088
H	-1.489745	1.645402	1.456635
H	-1.530889	0.033588	2.147653
C	-3.445267	0.715988	1.395176
H	-3.862436	-0.288321	1.246714
H	-3.817068	1.32975	0.564626
C	-3.960539	1.287581	2.723292
H	-3.527907	2.281618	2.884267
H	-3.621361	0.66347	3.555898
C	-5.484938	1.387713	2.753899
H	-5.938061	0.401978	2.619801
H	-5.85393	2.027056	1.949
S	-6.186317	1.98322	4.350802
H	-5.57103	3.183855	4.358568

C5CN electric field z-50

Atom	Coordinates (Angstroms)		
	X	Y	Z
C	0.024292	0.006642	-0.117112
N	1.173816	-0.021523	-0.195917
C	-1.430888	0.051233	-0.004743
H	-1.819564	0.637096	-0.844723
H	-1.814702	-0.967589	-0.124672
C	-1.91302	0.649632	1.331021
H	-1.491869	1.652754	1.446461
H	-1.518381	0.049189	2.155981
C	-3.442091	0.710637	1.404408
H	-3.853518	-0.297245	1.262113
H	-3.818445	1.317544	0.570472
C	-3.963398	1.28634	2.728613
H	-3.523879	2.276425	2.894187
H	-3.639032	0.658725	3.564206
C	-5.487005	1.399996	2.736164
H	-5.9461	0.419067	2.586187
H	-5.834798	2.050267	1.930523
S	-6.216026	1.98891	4.325091
H	-5.533107	3.150134	4.397496

6. Appendix

C6CN vac

Atom	Coordinates (Angstroms)		
	X	Y	Z
C	0.028444	-0.01686	-0.031491
N	1.180235	-0.052011	-0.06142
C	-1.4303	0.040163	0.030607
H	-1.790672	0.59246	-0.843713
H	-1.819195	-0.979177	-0.064516
C	-1.948227	0.692324	1.327484
H	-1.533365	1.702018	1.41009
H	-1.566386	0.131096	2.186315
C	-3.477677	0.747596	1.373935
H	-3.883662	-0.267524	1.278796
H	-3.849703	1.304965	0.504694
C	-4.014994	1.390561	2.657107
H	-3.608944	2.405556	2.752306
H	-3.641988	0.833204	3.525626
C	-5.547575	1.442943	2.705674
H	-5.960325	0.432192	2.621989
H	-5.922473	1.998454	1.83747
C	-6.07158	2.09132	3.985485
H	-5.703899	3.11382	4.094399
H	-5.734777	1.536666	4.864904
S	-7.906392	2.099676	4.141108
H	-8.148537	2.921172	3.093975

C6CN electric field z+50

Atom	Coordinates (Angstroms)		
	X	Y	Z
C	0.04021	-0.044309	-0.005141
N	1.19313	-0.101439	-0.015189
C	-1.418741	0.040836	0.030577
H	-1.748144	0.616235	-0.840696
H	-1.82326	-0.969404	-0.08967
C	-1.951895	0.681344	1.329771
H	-1.522294	1.682958	1.435196
H	-1.598493	0.096432	2.18516
C	-3.481834	0.763644	1.351525
H	-3.903332	-0.243088	1.243419
H	-3.830457	1.336676	0.483639
C	-4.021331	1.405162	2.63547
H	-3.618069	2.421934	2.728447
H	-3.645533	0.845852	3.502162
C	-5.554508	1.453074	2.696187
H	-5.961497	0.439402	2.626359
H	-5.941472	2.001317	1.829609

C	-6.06495	2.108693	3.980154
H	-5.728583	3.145914	4.053197
H	-5.675229	1.582021	4.855648
S	-7.888017	2.047815	4.206005
H	-8.207696	2.849544	3.168997

C6CN electric field z+25

Atom	Coordinates (Angstroms)		
	X	Y	Z
C	0.034326	-0.031289	-0.01873
N	1.186937	-0.079323	-0.040325
C	-1.424534	0.040936	0.030454
H	-1.767891	0.605408	-0.842641
H	-1.820629	-0.97426	-0.075925
C	-1.949907	0.688256	1.328452
H	-1.528992	1.694624	1.420417
H	-1.582037	0.115468	2.185713
C	-3.479984	0.755608	1.362932
H	-3.8922	-0.256037	1.262884
H	-3.840586	1.320768	0.494504
C	-4.018639	1.398135	2.646561
H	-3.615021	2.414427	2.73932
H	-3.64416	0.839524	3.513834
C	-5.55176	1.447726	2.701715
H	-5.960411	0.435043	2.624948
H	-5.932549	2.00098	1.835324
C	-6.068274	2.099119	3.984602
H	-5.713014	3.128128	4.075955
H	-5.707719	1.555028	4.861531
S	-7.898332	2.079341	4.173354
H	-8.176617	2.883001	3.125944

C6CN electric field z+10

Atom	Coordinates (Angstroms)		
	X	Y	Z
C	0.030796	-0.022663	-0.02765
N	1.183187	-0.064123	-0.057146
C	-1.427902	0.040653	0.03058
H	-1.780514	0.598398	-0.843216
H	-1.81819	-0.97769	-0.067434
C	-1.948612	0.691577	1.328144
H	-1.53267	1.700526	1.412645
H	-1.572447	0.125516	2.186137
C	-3.478698	0.750567	1.370012
H	-3.885689	-0.263777	1.274409

6. Appendix

H	-3.845999	1.311362	0.501375
C	-4.016974	1.393613	2.653495
H	-3.612664	2.409401	2.746537
H	-3.643897	0.834965	3.521099
C	-5.550127	1.444928	2.70476
H	-5.960127	0.43301	2.623665
H	-5.926612	2.001372	1.838368
C	-6.070485	2.094013	3.986833
H	-5.704783	3.118097	4.088829
H	-5.727165	1.540258	4.864413
S	-7.904062	2.098159	4.153992
H	-8.15836	2.902454	3.100978

C6CN electric field z+0

Atom	Coordinates (Angstroms)		
	X	Y	Z
C	0.028435	-0.016458	-0.033972
N	1.180648	-0.052929	-0.069224
C	-1.430097	0.040272	0.030779
H	-1.789355	0.593341	-0.84334
H	-1.816083	-0.980287	-0.06154
C	-1.947699	0.693454	1.328145
H	-1.535017	1.704045	1.407852
H	-1.566115	0.131719	2.186499
C	-3.477768	0.747051	1.374858
H	-3.881382	-0.269013	1.282102
H	-3.849371	1.305039	0.506109
C	-4.015853	1.390435	2.658246
H	-3.610876	2.405796	2.751633
H	-3.643977	0.83159	3.526075
C	-5.549052	1.443216	2.706672
H	-5.960108	0.431888	2.622592
H	-5.922402	2.001888	1.840246
C	-6.072058	2.090833	3.988141
H	-5.699678	3.111612	4.097157
H	-5.740203	1.530879	4.866062
S	-7.907741	2.110776	4.14107
H	-8.146242	2.915466	3.084663

C6CN electric field z-10

Atom	Coordinates (Angstroms)		
	X	Y	Z
C	0.026055	-0.009818	-0.040633
N	1.178053	-0.040713	-0.082085
C	-1.432251	0.039703	0.031094

H	-1.798605	0.587862	-0.843239
H	-1.813511	-0.983193	-0.055367
C	-1.94674	0.695063	1.328318
H	-1.537296	1.707245	1.403333
H	-1.559802	0.137564	2.18695
C	-3.476778	0.743376	1.37982
H	-3.877081	-0.274356	1.289845
H	-3.852568	1.298616	0.510971
C	-4.014727	1.387112	2.663102
H	-3.608914	2.40197	2.756954
H	-3.64428	0.827933	3.53117
C	-5.547991	1.441629	2.708473
H	-5.960238	0.430964	2.621287
H	-5.917974	2.002643	1.842006
C	-6.073721	2.08779	3.989306
H	-5.694836	3.105226	4.105351
H	-5.75337	1.521759	4.867476
S	-7.911334	2.123504	4.128063
H	-8.134083	2.928734	3.068631

C6CN electric field z-25

Atom	Coordinates (Angstroms)		
	X	Y	Z
C	0.022455	0.001182	-0.051311
N	1.174023	-0.019954	-0.103046
C	-1.435364	0.03837	0.031859
H	-1.813407	0.578445	-0.842655
H	-1.808486	-0.988347	-0.045292
C	-1.945229	0.696987	1.328885
H	-1.540691	1.711517	1.396904
H	-1.55031	0.145846	2.187861
C	-3.475195	0.73747	1.387492
H	-3.870595	-0.282697	1.301583
H	-3.857098	1.288651	0.518501
C	-4.01306	1.381745	2.670591
H	-3.605577	2.395659	2.765448
H	-3.645283	0.821739	3.539037
C	-5.546444	1.43953	2.710906
H	-5.960841	0.430059	2.618657
H	-5.910837	2.004431	1.84443
C	-6.076398	2.083402	3.990784
H	-5.687964	3.095697	4.117566
H	-5.773489	1.508331	4.869092
S	-7.916588	2.142946	4.108304
H	-8.115615	2.949602	3.04523

6. Appendix

C6CN electric field z-50

Atom	Coordinates (Angstroms)		
	X	Y	Z
C	0.016269	0.022998	-0.071256
N	1.16661	0.022986	-0.143304
C	-1.440124	0.03437	0.034245
H	-1.841145	0.558044	-0.840281
H	-1.795935	-0.999796	-0.025212
C	-1.942474	0.698856	1.330713
H	-1.546466	1.7173	1.386713
H	-1.534249	0.158767	2.190293
C	-3.472274	0.726274	1.400957
H	-3.85953	-0.297846	1.321774
H	-3.863999	1.270647	0.531639
C	-4.01041	1.371664	2.683575
H	-3.598885	2.383422	2.780932
H	-3.648743	0.809384	3.552763
C	-5.544031	1.436973	2.713933
H	-5.963143	0.430183	2.611593
H	-5.897376	2.009856	1.847854
C	-6.081451	2.076189	3.992466
H	-5.677339	3.079341	4.138339
H	-5.808522	1.485616	4.870048
S	-7.925081	2.176557	4.074342
H	-8.083694	2.988828	3.008698

7. References

1. Hildebrandt, P. & Friedrich, S. *Friedrich Siebert and Peter Hildebrandt, vibrational spectroscopy in life science.* (Wiley- VCH, 2008).
2. Michelson, A. A. XXXVIII. On the application of interference-methods to spectroscopic measurements.—I. *Phil. Mag.* **31**, 338–346 (1891).
3. Griffiths, P. R. & DeHaseth, J. A. *Fourier Transform Infrared Spectrometry.* 2nd Edition, (John Wiley & Sons, Inc., 2007).
4. Herzberg, G. *Molecular Spectra and Molecular Structure: II, Infrared and Raman Spectra of Polyatomic Molecules.* (Van Nostrand Reinhold, New York, 1945).
5. Kozuch, J. A. Structure-Function Relationships of Membrane Proteins - Spectroelectrochemical Investigation of Artificial Membranes. (2013).
6. Khoa Ly, H. *et al.* Electric-field effects on the interfacial electron transfer and protein dynamics of cytochrome c. *J. Electroanal. Chem.* **660**, 367–376 (2011).
7. Schkolnik, G. Vibrational Stark Spectroscopy as a Tool for Probing Electrostatics at Protein Surfaces and Self Assembled Monolayers. (2012).
8. Herbst, J., Heyne, K. & Diller, R. Femtosecond Infrared Spectroscopy of Bacteriorhodopsin Chromophore Isomerization. *Science (80-.)* **297**, 822–825 (2002).
9. Laimgruber, S., Schachenmayr, H., Schmidt, B., Zinth, W. & Gilch, P. A femtosecond stimulated raman spectrograph for the near ultraviolet. *Appl. Phys. B* **85**, 557–564 (2006).
10. Wiebalck, S. *et al.* Monitoring the Transmembrane Proton Gradient Generated by Cytochrome bo 3 in Tethered Bilayer Lipid Membranes Using SEIRA Spectroscopy. *J. Phys. Chem. B* **120**, 2249–2256 (2016).
11. Khoa Ly, H. *et al.* Surface-enhanced vibrational spectroscopy for probing transient interactions of proteins with biomimetic interfaces: electric field effects on structure, dynamics and function of cytochrome c. *FEBS J.* **278**, 1382–1390 (2011).
12. Peter Atkins & Julio de Paula. *Atkins' Physical Chemistry.* (Oxford University Press, 2006).
13. Bouguer, P. M. *Essai d'optique sur la gradation de la lumière.* (Claude Jombert, l'Image Notre-Dame, 1729).
14. Lambert, D. K. Vibrational Stark effect of adsorbates at electrochemical interfaces. *Electrochim. Acta* **41**, 623–630 (1996).
15. Beer, A. Bestimmung der Absorption des rothen Lichts in farbigen Flussgkeiten (Determination of the absorption of red light in colored liquids). *Ann. der Phys. und Chemie* **86**, 78–88 (1852).
16. Osawa, M. in *Handbook of Vibrational Spectroscopy* (ed. Chalmers, J. M.) **7**, 2861–2880 (John Wiley & Sons, Ltd, 2006).
17. Hartstein, A., Kirtley, J. R. & Tsang, J. C. Enhancement of the infrared absorption from molecular monolayers with thin metal overlayers. *Phys. Rev. Lett.* **45**, 201–204 (1980).
18. Osawa, M. & Ikeda, M. Surface-enhanced infrared absorption of p-nitrobenzoic acid deposited on silver island films: contributions of electromagnetic and chemical

7. References

- mechanisms. *J. Phys. Chem.* **95**, 9914–9919 (1991).
- 19. Kozuch, J. *et al.* Voltage-dependent structural changes of the membrane-bound anion channel hVDAC1 probed by SEIRA and electrochemical impedance spectroscopy. *Phys. Chem. Chem. Phys.* **16**, 9546–9555 (2014).
 - 20. Forbrig, E. *et al.* Monitoring the Orientational Changes of Alamethicin during Incorporation into Bilayer Lipid Membranes. *Langmuir* **34**, 2373–2385 (2018).
 - 21. Staffa, J. K. *et al.* Determination of the Local Electric Field at Au/SAM Interfaces Using the Vibrational Stark Effect. *J. Phys. Chem. C* **121**, 22274–22285 (2017).
 - 22. Vadim F., L. *Impedance Spectroscopy Applications to Electrochemical and Dielectric Phenomena.* (2012).
 - 23. Cole, K. S. & Cole, R. H. Dispersion and absorption in dielectrics I. Alternating current characteristics. *J. Chem. Phys.* **9**, 341–351 (1941).
 - 24. Erbe, A., Bushby, R. J., Evans, S. D. & Jeuken, L. J. C. Tethered Bilayer Lipid Membranes Studied by Simultaneous Attenuated Total Reflectance Infrared Spectroscopy and Electrochemical Impedance Spectroscopy. *J. Phys. Chem. B* **111**, 3515–3524 (2007).
 - 25. Cole, K. S. Electric Phase Angle of Cell Membranes. *J. Gen. Physiol.* **15**, 641–649 (1932).
 - 26. Jeuken, L. J. C. *et al.* Phase separation in mixed self-assembled monolayers and its effect on biomimetic membranes. *Sensors Actuators B Chem.* **124**, 501–509 (2007).
 - 27. Su, Z., Leitch, J. J. & Lipkowski, J. Electrode-supported biomimetic membranes: An electrochemical and surface science approach for characterizing biological cell membranes. *Curr. Opin. Electrochem.* In Press (2018). doi:10.1016/j.coelec.2018.05.020
 - 28. Nuzzo, R. G. & Allara, D. L. Adsorption of bifunctional organic disulfides on gold surfaces. *J. Am. Chem. Soc.* **105**, 4481–4483 (1983).
 - 29. Whitesides, G. M., Kriebel, J. K. & Love, J. C. Molecular engineering of surfaces using self-assembled monolayers. *Sci. Prog.* **88**, 17–48 (2005).
 - 30. Love, J. C., Estroff, L. A., Kriebel, J. K., Nuzzo, R. G. & Whitesides, G. M. Self-assembled monolayers of thiolates on metals as a form of nanotechnology. *Chem. Rev.* **105**, 1103–1169 (2005).
 - 31. Jeuken, L. J. C. AFM Study on the Electric-Field Effects on Supported Bilayer Lipid Membranes. *Biophys. J.* **94**, 4711–4717 (2008).
 - 32. Aaron T. Fafarman, Lauren J. Webb, Jessica I. Chuang & Steven G. Boxer. Site-Specific Conversion of Cysteine Thiols into Thiocyanate Creates an IR Probe for Electric Fields in Proteins. *J. Am. Chem. Soc.* **128**, 13356–13357 (2006).
 - 33. Levinson, N. M., Fried, S. D. & Boxer, S. G. Solvent-Induced Infrared Frequency Shifts in Aromatic Nitriles Are Quantitatively Described by the Vibrational Stark Effect. *J. Phys. Chem. B* **116**, 10470–10476 (2012).
 - 34. Nuzzo, R. G., Zegarski, B. R. & Dubois, L. H. Fundamental studies of the chemisorption of organosulfur compounds on gold(111). Implications for molecular self-assembly on gold surfaces. *J. Am. Chem. Soc.* **109**, 733–740 (1987).
 - 35. Schreiber, F. Structure and growth of self-assembling monolayers. *Prog. Surf. Sci.* **65**, 151–257 (2000).
 - 36. Dubois, L. H. & Nuzzo, R. G. Synthesis, Structure, and Properties of Model Organic Surfaces. *Annu. Rev. Phys. Chem.* **43**, 437–463 (1992).

37. Schlenoff, J. B., Li, M. & Ly, H. Stability and Self-Exchange in Alkanethiol Monolayers. *J. Am. Chem. Soc.* **117**, 12528–12536 (1995).
38. Walczak, M. M., Chung, C., Stole, S. M., Widrig, C. A. & Porter, M. D. Structure and interfacial properties of spontaneously adsorbed n-alkanethiolate monolayers on evaporated silver surfaces. *J. Am. Chem. Soc.* **113**, 2370–2378 (1991).
39. Laibinis, P. E. *et al.* Comparison of the structures and wetting properties of self-assembled monolayers of n-alkanethiols on the coinage metal surfaces, copper, silver, and gold. *J. Am. Chem. Soc.* **113**, 7152–7167 (1991).
40. Laibinis, P. E. *et al.* Comparison of the structures and wetting properties of self-assembled monolayers of n-alkanethiols on the coinage metal surfaces, copper, silver, and gold. *J. Am. Chem. Soc.* **113**, 7152–7167 (1991).
41. Li, Z., Chang, S.-C. & Williams, R. S. Self-Assembly of Alkanethiol Molecules onto Platinum and Platinum Oxide Surfaces. *Langmuir* **19**, 6744–6749 (2003).
42. Han, S. W., Lee, S. J. & Kim, K. Self-Assembled Monolayers of Aromatic Thiol and Selenol on Silver: Comparative Study of Adsorptivity and Stability. *Langmuir* **17**, 6981–6987 (2001).
43. Frey, S. *et al.* Structure of Thioaromatic Self-Assembled Monolayers on Gold and Silver. *Langmuir* **17**, 2408–2415 (2001).
44. Käfer, D., Bashir, A. & Witte, G. Interplay of Anchoring and Ordering in Aromatic Self-Assembled Monolayers. *J. Phys. Chem. C* **111**, 10546–10551 (2007).
45. Ballav, N. *et al.* Direct Probing Molecular Twist and Tilt in Aromatic Self-Assembled Monolayers. *J. Am. Chem. Soc.* **129**, 15416–15417 (2007).
46. Shaw, S. K., Lagutchev, A., Dlott, D. D. & Gewirth, A. A. Sum-Frequency Spectroscopy of Molecular Adsorbates on Low-Index Ag Surfaces: Effects of Azimuthal Rotation. *Anal. Chem.* **81**, 1154–1161 (2009).
47. Nuzzo, R. G., Dubois, L. H. & Allara, D. L. Fundamental studies of microscopic wetting on organic surfaces. 1. Formation and structural characterization of a self-consistent series of polyfunctional organic monolayers. *J. Am. Chem. Soc.* **112**, 558–569 (1990).
48. Chon, S. & Paik, W. Adsorption of self-assembling sulfur compounds through electrochemical reactions: Effects of potential, acid and oxidizing agents. *Phys. Chem. Chem. Phys.* **3**, 3405–3410 (2001).
49. Bain, C. D. & Whitesides, G. M. Formation of monolayers by the coadsorption of thiols on gold: variation in the length of the alkyl chain. *J. Am. Chem. Soc.* **111**, 7164–7175 (1989).
50. Clarke, R. J. Effect of lipid structure on the dipole potential of phosphatidylcholine bilayers. *Biochim. Biophys. Acta - Biomembr.* **1327**, 269–278 (1997).
51. Clarke, R. J. The dipole potential of phospholipid membranes and methods for its detection. *Adv. Colloid Interface Sci.* **89–90**, 263–281 (2001).
52. Hu, W. & Webb, L. J. Direct Measurement of the Membrane Dipole Field in Bicelles Using Vibrational Stark Effect Spectroscopy. *J. Phys. Chem. Lett.* **2**, 1925–1930 (2011).
53. Montal, M. & Mueller, P. Formation of Bimolecular Membranes from Lipid Monolayers and a Study of Their Electrical Properties. *Proc. Natl. Acad. Sci.* **69**, 3561–3566 (1972).
54. Staffa, J. K. Spectroscopic studies on the vibrational Stark effect of self-assembled monolayers. (2015).
55. Smith, C. P. & White, H. S. Theory of the interfacial potential distribution and reversible

7. References

- voltammetric response of electrodes coated with electroactive molecular films. *Anal. Chem.* **64**, 2398–2405 (1992).
- 56. Murgida, D. H. & Hildebrandt, P. Heterogeneous Electron Transfer of Cytochrome c on Coated Silver Electrodes. Electric Field Effects on Structure and Redox Potential. *J. Phys. Chem. B* **105**, 1578–1586 (2001).
 - 57. Schkolnik, G. *et al.* Vibrational Stark Effect of the Electric-Field Reporter 4-Mercaptobenzonitrile as a Tool for Investigating Electrostatics at Electrode/SAM/Solution Interfaces. *Int. J. Mol. Sci.* **13**, 7466–7482 (2012).
 - 58. Miller, C. Ionic channels of excitable membranes. Second edition. *Cell* **69**, 579 (1992).
 - 59. Fried, S. D., Bagchi, S. & Boxer, S. . Extreme electrif fields power catalysis in the active site of ketosteroid isomerase. *Science (80-.)* **346**, 1510–1514 (2014).
 - 60. Fried, S. D. & Boxer, S. G. Electric Fields and Enzyme Catalysis. *Annu. Rev. Biochem.* **86**, 387–415 (2017).
 - 61. Fried, S. D. & Boxer, S. G. Measuring Electric Fields and Noncovalent Interactions Using the Vibrational Stark Effect. *Acc. Chem. Res.* **48**, 998–1006 (2015).
 - 62. Suydam, I. T. & Boxer, S. G. Vibrational Stark effects calibrate the sensitivity of vibrational probes for electric fields in proteins. *Biochemistry* **42**, 12050–12055 (2003).
 - 63. Park, E. S., Andrews, S. S., Hu, R. B. & Boxer, S. G. Vibrational Stark Spectroscopy in Proteins: A Probe and Calibration for Electrostatic Fields. *J. Phys. Chem. B* **103**, 9813–9817 (1999).
 - 64. Fried, S. D., Bagchi, S. & Boxer, S. G. Measuring Electrostatic Fields in Both Hydrogen-Bonding and Non-Hydrogen-Bonding Environments Using Carbonyl Vibrational Probes. *J. Am. Chem. Soc.* **135**, 11181–11192 (2013).
 - 65. Schneider, S. H. & Boxer, S. G. Vibrational Stark Effects of Carbonyl Probes Applied to Reinterpret IR and Raman Data for Enzyme Inhibitors in Terms of Electric Fields at the Active Site. *J. Phys. Chem. B* **120**, 9672–9684 (2016).
 - 66. Zhang, W., Markiewicz, B. N., Doerksen, R. S., Smith, III, A. B. & Gai, F. CN stretching vibration of 5-cyanotryptophan as an infrared probe of protein local environment: what determines its frequency? *Phys. Chem. Chem. Phys.* **18**, 7027–7034 (2016).
 - 67. Fafarman, A. T., Sigala, P. a, Herschlag, D. & Boxer, S. G. Decomposition of Vibrational Shifts of Nitriles into Electrostatic and Hydrogen-Bonding Effects. *J. Am. Chem. Soc.* **132**, 12811–12813 (2010).
 - 68. Aschaffenburg, D. J. & Moog, R. S. Probing Hydrogen Bonding Environments: Solvatochromic Effects on the CN Vibration of Benzonitrile. *J. Phys. Chem. B* **113**, 12736–12743 (2009).
 - 69. Onsager, L. LARS ONSAGER Vol. 58. *J. Am. Chem. Soc.* **58**, 1486–1493
 - 70. Becke, A. D. Density-functional thermochemistry. III. The role of exact exchange. *J. Chem. Phys.* **98**, 5648–5652 (1993).
 - 71. Lorenz, L. Schwingungsspektroskopische Untersuchung von selbstorganisierten Monoschichten aus bifunktionellen Thiolen. (2004).
 - 72. Luippold, A. H., Arnhold, T., Jörg, W. & Süßmuth, R. D. An integrated platform for fully automated high-throughput LC–MS/MS analysis of in vitro metabolic stability assay samples. *Int. J. Mass Spectrom.* **296**, 1–9 (2010).
 - 73. Miyake, H., Ye, S. & Osawa, M. Electroless deposition of gold thin films on silicon for

- surface-enhanced infrared spectroelectrochemistry. *Electrochim. commun.* **4**, 973–977 (2002).
74. Trasatti, S. & Petrii, O. A. Real surface area measurements in electrochemistry. *J. Electroanal. Chem.* **327**, 353–376 (1992).
75. Schmitt, E. K., Nurnabi, M., Bushby, R. J. & Steinem, C. Electrically insulating pore-suspending membranes on highly ordered porous alumina obtained from vesicle spreading. *Soft Matter* **4**, 250–253 (2008).
76. Whim, B.P., P. G. & Johnson. *Directory of Solvents*. (Springer Netherlands, 1996). doi:10.1007/978-94-009-1549-7
77. Reichardt, C. *Solvents and Solvent Effects in Organic Chemistry*. (Wiley-VCH, 2003).
78. Frisch, M. J. *et al.* Gaussian09. *Gaussian 09* (2009).
79. Clark, T., Chandrasekhar, J., Spitznagel, G. W. & Schleyer, P. V. R. Efficient diffuse function-augmented basis sets for anion calculations. III. The 3-21+G basis set for first-row elements, Li-F. *J. Comput. Chem.* **4**, 294–301 (1983).
80. Frisch, M. J., Pople, J. A. & Binkley, J. S. Self-consistent molecular orbital methods 25. Supplementary functions for Gaussian basis sets. *J. Chem. Phys.* **80**, 3265–3269 (1984).
81. McLean, A. D. & Chandler, G. S. Contracted Gaussian basis sets for molecular calculations. I. Second row atoms, Z = 11–18. *J. Chem. Phys.* **72**, 5639–5648 (1980).
82. Krishnan, R., Binkley, J. S., Seeger, R. & Pople, J. A. Self-consistent molecular orbital methods. XX. A basis set for correlated wave functions. *J. Chem. Phys.* **72**, 650–654 (1980).
83. Miertuš, S., Scrocco, E. & Tomasi, J. Electrostatic interaction of a solute with a continuum. A direct utilization of AB initio molecular potentials for the prevision of solvent effects. *Chem. Phys.* **55**, 117–129 (1981).
84. Miertuš, S. & Tomasi, J. Approximate evaluations of the electrostatic free energy and internal energy changes in solution processes. *Chem. Phys.* **65**, 239–245 (1982).
85. Cossi, M., Barone, V. & Robb, M. A. A direct procedure for the evaluation of solvent effects in MC-SCF calculations. *J. Chem. Phys.* **111**, 5295–5302 (1999).
86. Tomasi, J., Mennucci, B. & Cancès, E. The IEF version of the PCM solvation method: an overview of a new method addressed to study molecular solutes at the QM ab initio level. *J. Mol. Struct. THEOCHEM* **464**, 211–226 (1999).
87. Cammi, R., Mennucci, B. & Tomasi, J. Fast Evaluation of Geometries and Properties of Excited Molecules in Solution: A Tamm-Dancoff Model with Application to 4-Dimethylaminobenzonitrile. *J. Phys. Chem. A* **104**, 5631–5637 (2000).
88. Cossi, M. & Barone, V. Time-dependent density functional theory for molecules in liquid solutions. *J. Chem. Phys.* **115**, 4708–4717 (2001).
89. Cossi, M., Rega, N., Scalmani, G. & Barone, V. Polarizable dielectric model of solvation with inclusion of charge penetration effects. *J. Chem. Phys.* **114**, 5691–5701 (2001).
90. Cossi, M., Rega, N., Scalmani, G. & Barone, V. Energies, structures, and electronic properties of molecules in solution with the C-PCM solvation model. *J. Comput. Chem.* **24**, 669–681 (2003).
91. Cammi, R. Quantum cluster theory for the polarizable continuum model. I. The CCSD level with analytical first and second derivatives. *J. Chem. Phys.* **131**, 164104 (2009).
92. Cammi, R. Coupled-cluster theories for the polarizable continuum model. II. Analytical

7. References

- gradients for excited states of molecular solutes by the equation of motion coupled-cluster method. *Int. J. Quantum Chem.* **110**, 3040–3052 (2010).
93. Scalmani, G. & Frisch, M. J. Continuous surface charge polarizable continuum models of solvation. I. General formalism. *J. Chem. Phys.* **132**, 114110 (2010).
 94. Lipparini, F. *et al.* A variational formulation of the polarizable continuum model. *J. Chem. Phys.* **133**, 014106 (2010).
 95. Pascual-ahuir, J. L., Silla, E. & Tuñon, I. GEPOL: An improved description of molecular surfaces. III. A new algorithm for the computation of a solvent-excluding surface. *J. Comput. Chem.* **15**, 1127–1138 (1994).
 96. Cossi, M., Barone, V., Cammi, R. & Tomasi, J. Ab initio study of solvated molecules: a new implementation of the polarizable continuum model. *Chem. Phys. Lett.* **255**, 327–335 (1996).
 97. Barone, V., Cossi, M. & Tomasi, J. A new definition of cavities for the computation of solvation free energies by the polarizable continuum model. *J. Chem. Phys.* **107**, 3210–3221 (1997).
 98. Mennucci, B., Cancès, E. & Tomasi, J. Evaluation of Solvent Effects in Isotropic and Anisotropic Dielectrics and in Ionic Solutions with a Unified Integral Equation Method: Theoretical Bases, Computational Implementation, and Numerical Applications. *J. Phys. Chem. B* **101**, 10506–10517 (1997).
 99. Mennucci, B. & Tomasi, J. Continuum solvation models: A new approach to the problem of solute's charge distribution and cavity boundaries. *J. Chem. Phys.* **106**, 5151–5158 (1997).
 100. Barone, V. & Cossi, M. Quantum Calculation of Molecular Energies and Energy Gradients in Solution by a Conductor Solvent Model. *J. Phys. Chem. A* **102**, 1995–2001 (1998).
 101. Cossi, M., Barone, V., Mennucci, B. & Tomasi, J. Ab initio study of ionic solutions by a polarizable continuum dielectric model. *Chem. Phys. Lett.* **286**, 253–260 (1998).
 102. Cammi, R., Mennucci, B. & Tomasi, J. Second-Order Møller–Plesset Analytical Derivatives for the Polarizable Continuum Model Using the Relaxed Density Approach. *J. Phys. Chem. A* **103**, 9100–9108 (1999).
 103. Bagchi, S., Fried, S. D. & Boxer, S. G. A Solvatochromic Model Calibrates Nitriles' Vibrational Frequencies to Electrostatic Fields. *J. Am. Chem. Soc.* **134**, 10373–10376 (2012).
 104. Lindner, S. *et al.* Azide-Modified Membrane Lipids: Synthesis, Properties, and Reactivity. *Langmuir* **33**, 4960–4973 (2017).
 105. Tookmanian, E. M., Phillips-Piro, C. M., Fenlon, E. E. & Brewer, S. H. Azidoethoxyphenylalanine as a Vibrational Reporter and Click Chemistry Partner in Proteins. *Chem. - A Eur. J.* **21**, 19096–19103 (2015).
 106. Tlili, A., Abdelghani, A., Hleli, S. & Maaref, M. Electrical Characterization of a Thiol SAM on Gold as a First Step for the Fabrication of Immunosensors based on a Quartz Crystal Microbalance. *Sensors* **4**, 105–114 (2004).
 107. Agonafer, D. D., Chainani, E., Oruc, M. E., Lee, K. S. & Shannon, M. A. Study of Insulating Properties of Alkanethiol Self-Assembled Monolayers Formed Under Prolonged Incubation Using Electrochemical Impedance Spectroscopy. *J. Nanotechnol. Eng. Med.* **3**, 031006 (2013).
 108. Schkolnik, G. *et al.* Mapping local electric fields in proteins at biomimetic interfaces.

- Chem. Commun.* **48**, 70–72 (2012).
109. Schkolnik, G. *et al.* Vibrational stark effect of the electric-field reporter 4-mercaptopbenzonitrile as a tool for investigating electrostatics at electrode/SAM/solution interfaces. *Int. J. Mol. Sci.* **13**, 7466–7482 (2012).
 110. Becka, A. M. & Miller, C. J. Electrochemistry at o-Hydroxy Thiol Coated Electrodes . 4 . Comparison of the Double Layer at w-Hydroxy Thiol and Alkanethiol Monolayer Coated Au Electrodes + Cm. *J. Phys. Chem.* **97**, 6233–6239 (1993).
 111. Trasatti, S. Work function, electronegativity, and electrochemical behaviour of metals. *J. Electroanal. Chem. Interfacial Electrochem.* **33**, 351–378 (1971).
 112. Ramírez, P. *et al.* Potential of zero charge of Au (111) modified with ω - mercaptoalkanoic acid monolayers . *Anal. Chem.* **79**, 6473–6479 (2007).
 113. Wang, L. *et al.* Electronic Structure of Self-Assembled Monolayers on Au(111) Surfaces: The Impact of Backbone Polarizability. *Adv. Funct. Mater.* **19**, 3766–3775 (2009).
 114. Valette, G. Hydrophilicity of metal surfaces. *J. Electroanal. Chem. Interfacial Electrochem.* **139**, 285–301 (1982).
 115. Boxer, S. G. Stark Realities. *J. Phys. Chem. B* **113**, 2972–2983 (2009).
 116. Bain, C. D. & Whitesides, G. M. Modeling organic surfaces with self-assembled monolayers. *Adv. Mater.* **1**, 110–116 (1989).
 117. Deb, P. *et al.* Correlating Nitrile IR Frequencies to Local Electrostatics Quantifies Noncovalent Interactions of Peptides and Proteins. *J. Phys. Chem. B* **120**, 4034–4046 (2016).
 118. Ferreira, T. M. *et al.* Cholesterol and POPC segmental order parameters in lipid membranes: solid state ^1H – ^{13}C NMR and MD simulation studies. *Phys. Chem. Chem. Phys.* **15**, 1976–1989 (2013).
 119. Smondyrev, A. M. & Berkowitz, M. L. Structure of Dipalmitoylphosphatidylcholine/Cholesterol Bilayer at Low and High Cholesterol Concentrations: Molecular Dynamics Simulation. *Biophys. J.* **77**, 2075–2089 (1999).
 120. Jo, S., Lim, J. B., Klauda, J. B. & Im, W. CHARMM-GUI Membrane Builder for Mixed Bilayers and Its Application to Yeast Membranes. *Biophys. J.* **97**, 50–58 (2009).
 121. Nagle, J. F. & Tristram-Nagle, S. Structure of lipid bilayers. *Biochim. Biophys. Acta - Rev. Biomembr.* **1469**, 159–195 (2000).
 122. Aitttoniemi, J., Niemelä, P. S., Hyvönen, M. T., Karttunen, M. & Vattulainen, I. Insight into the Putative Specific Interactions between Cholesterol, Sphingomyelin, and Palmitoyl-Oleoyl Phosphatidylcholine. *Biophys. J.* **92**, 1125–1137 (2007).
 123. Dilger, J., McLaughlin, S., McIntosh, T. & Simon, S. The dielectric constant of phospholipid bilayers and the permeability of membranes to ions. *Science (80-).* **206**, 1196–1198 (1979).
 124. Bain, C. D., Evall, J. & Whitesides, G. M. Formation of monolayers by the coadsorption of thiols on gold: variation in the head group, tail group, and solvent. *J. Am. Chem. Soc.* **111**, 7155–7164 (1989).
 125. Wiebalck, S. *et al.* Monitoring the Transmembrane Proton Gradient Generated by Cytochrome bo3in Tethered Bilayer Lipid Membranes Using SEIRA Spectroscopy. *J. Phys. Chem. B* (2016). doi:10.1021/acs.jpcb.6b01435
 126. Murzyn, K., Róg, T. & Pasenkiewicz-Gierula, M. Phosphatidylethanolamine-

7. References

Phosphatidylglycerol Bilayer as a Model of the Inner Bacterial Membrane. *Biophys. J.* **88**, 1091–1103 (2005).

8. Danksagung

Ich möchte mich bei allen bedanken, die mich während dieser Arbeit unterstützt haben ganz besonders:

- Prof. Dr. Peter Hildebrandt für die Betreuung und persönlichen Engagement. Vielen Dank für die Möglichkeit diese Doktorarbeit anzufertigen.
- Prof. Dr. Franz Bartl für die Übernahme des Zweitgutachtens.
- Der IRTG 1524 für die finanzielle Unterstützung meiner Doktorarbeit.
- Dr. Jacek Kozuch für die Einarbeitung in die theoretischen und praktischen Arbeiten, sowie die zahlreichen Diskussionen und persönliche Betreuung.
- Dr. Tillmann Utesch für die gute Zusammenarbeit und die theoretischen MD-Simulationen.
- Christoph Fahrenson am ZELMI der TU Berlin für die Möglichkeit und Durchführung der SEM-Messungen.
- Dr. Ingo Zebger für die technische Betreuung der Spektrometer, sowie der Hilfe bei der Lösung technischer Fehler.
- Prof. Dr. Martin Lerch für die Übernahme des Vorsitzes meiner Disputation.
- Allen Mitarbeitern des MVL, ganz besonders Claudia Schulz für die Hilfe im Labor, Marina Böttcher für die organisatorische Hilfe bei Fragen aller Art, Jürgen Krauss und Lars Paasche für ihre technische Unterstützung.
- Prof. Süßmuth für die Möglichkeit die Aufreinigung der Monolayer in seinen Laboren durchzuführen.
- Dr. Khoa Ly, Dr. Alexandre Ciaccafava, Dr. Murat Sezer, Sagie Katz, Anke Keidel, David Bührke, Dr. Tomos Harris, Dr. Patrycja Kielb, Dr. Marius Horch, Fabian Kruse, Dr. Stefan Wahlefeld, Christian Lorent, Anastasia Kraskov, Christine Querebillo für die angenehme Arbeitsatmosphäre im Labor und während des Zusammenschreibens.
- Dr. Eleanor Ewins und José Danglad Flores für die gemeinsame lebhafte Zeit während zahlreicher Meetings.
- Enrico für die zahlreichen Diskussionen und Unterstützung, sowie einer entspannten Konferenzreise.
- Cathi, Svea und Sven für jede einzelne entspannte und erheiternde Kaffeepause.
- Meiner ganzen Familie, ganz besonders meinen Eltern, die es mir ermöglicht haben, Chemie zu studieren und diese Arbeit zu schreiben, sowie meinem Bruder Nils für die Auflockerung des Alltages.
- Robert für Geduld und Unterstützung während der Doktorarbeit.